

THE UNIVERSITY OF CALGARY

Optimal drilling direction in folded fractured Triassic carbonates
in northeastern British Columbia determined by applying fracture
“occurrence” to frequency intercept and flow diagrams.

by

Terry G. Joubert

A THESIS

SUBMITTED TO THE FACULTY OF GRADUATE STUDIES
IN PARTIAL FULFILLMENT OF THE REQUIREMENTS FOR THE
DEGREE OF MASTER OF SCIENCE

DEPARTMENT OF GEOLOGY AND GEOPHYSICS

CALGARY, ALBERTA

SEPTEMBER, 1998

© Terry G. Joubert 1998



National Library
of Canada

Acquisitions and
Bibliographic Services

395 Wellington Street
Ottawa ON K1A 0N4
Canada

Bibliothèque nationale
du Canada

Acquisitions et
services bibliographiques

395, rue Wellington
Ottawa ON K1A 0N4
Canada

Your file Votre référence

Our file Notre référence

The author has granted a non-exclusive licence allowing the National Library of Canada to reproduce, loan, distribute or sell copies of this thesis in microform, paper or electronic formats.

The author retains ownership of the copyright in this thesis. Neither the thesis nor substantial extracts from it may be printed or otherwise reproduced without the author's permission.

L'auteur a accordé une licence non exclusive permettant à la Bibliothèque nationale du Canada de reproduire, prêter, distribuer ou vendre des copies de cette thèse sous la forme de microfiche/film, de reproduction sur papier ou sur format électronique.

L'auteur conserve la propriété du droit d'auteur qui protège cette thèse. Ni la thèse ni des extraits substantiels de celle-ci ne doivent être imprimés ou autrement reproduits sans son autorisation.

0-612-34965-9

ABSTRACT

A new method is used to calculate fracture intercept and flow diagrams using fracture "occurrence" (Lacazette, 1991) measurements. The analysis is done for nine wells in northeastern British Columbia using borehole image logs. The wells are drilled into complexly structured folds of the upper Triassic Pardonet and Baldonnel formations. The folds are "unfolded" to compare the fractures relative to horizontal bedding.

The flow diagrams are used to determine the optimal drilling direction (Nolen-Hoeksema and Howard, 1987) from the nine well data interpretations. Two fracture sets influence the optimal drilling direction. The most frequent fracture set strikes NNE/SSW. However, the optimal drilling direction depends more on large aperture Type 2 (striking NW/SE) fractures. From the data, an optimal drilling direction is found with an inclination of 0-30 degrees relative to bedding, and an azimuth of 70 degrees, measured counterclockwise from the trend in the region of the well.

ACKNOWLEDGMENTS

This work would not have been possible without the support of Amoco Canada and their permission to use their data and resources. I would like to acknowledge the financial support for this thesis provided by other sponsors of the Foothills Research Project and the Natural Science and Engineering Research Council of Canada (NSERC). Debbie Spratt provided support, encouragement and many hours of editing for which I am immensely grateful. There have been many people who have provided technical support including Jay Guidos of Gaia Software Inc. and Ron Nelson who patiently listened to, helped and supported my ideas. Craig Rice was the greatest technical supporter of this work. Craig helped me immensely with log analysis, geological support and just being a great geologist to discuss ideas with. This thesis would not have been possible without Craig's help. Lastly, I would like to thank my family for their unconditional support and love. My son Alex was one when I began graduate studies and is now heading off to his first year in school. My daughter, Catharine, was born in my first year of course work. Having a young family, working and being a full time student puts a lot of strain on a family. Without the support and love of my partner, Heather White, I would not have been able to have completed this thesis. Thanks again Heather for the unselfish support and encouragement to help me through these last few, most challenging years of our lives.

Table of Contents

Title Page	i
Approval Page	ii
Abstract	iii
Acknowledgments	iv
Table of Contents	v
List of Figures	vii
 CHAPTER 1. INTRODUCTION AND BACKGROUND	 1
Introduction	1
Study Area	3
Stratigraphy	5
Structural Geology	9
Fracture Measurements from the FMI/FMS Tool	14
Fracture Classification	22
Fracturing Inferred from Fold Models	26
Previous Work	34
 CHAPTER 2. ANALYSIS METHOD	 42
Introduction	42
Data Interpretation	42
Fracture Frequency and Spacing	43
Occurrence Measurements	46
Fracture Rotation	55
Summary	56
 CHAPTER 3. STRUCTURAL ANALYSIS OF WELL DATA	 57
Introduction	57
Well 1	60
Well 2	68
Well 3	75
Well 4	82
Well 5	90
Well 6	97
Well 7	104
Well 8	111
Well 9	118
 CHAPTER 4. DISCUSSION	 125
Fracture Orientations	125
Fracture Aperture	129
Structural Position versus Fracture Density and Volume	134

Fracture Density	134
Fracture Volume	137
Vertical Changes in Fracture Volumes and Densities	140
Optimal Drilling Direction	144
Optimal Drilling Direction Recommendation	147
A Comparison of the Nine Wells to the Optimal Drilling Direction	147
Summary	150
CHAPTER 5. RECOMMENDATIONS AND CONCLUSIONS	152
Conclusions	152
Fracture Occurrence	152
Fracture Rotations	153
Fracture Orientations	153
Fracture Apertures	153
Structural Position and Fracture Densities and Volumes	154
Fracture Changes Vertically in the Well	154
Optimal Drilling Direction	155
Recommendations	156
Aperture Measurements	156
Production and Optimal Drilling Direction	156
REFERENCES	158
APPENDIX 1. Occurrence - Visual Basic Program	167
Introduction	167
Program	168
Dialog Boxes	172
APPENDIX 2. Intercept and Flow Diagrams - Visual Basic Program	174
Introduction	174
Program	174

List of Figures

Figure 1-1: Location map (modified from Barss and Montandon, 1981)	4
Figure 1-2: Triassic stratigraphic section (from Rice, 1997, modified from Davies 1992)	6
Figure 1-3: Folding style (modified from Barss and Montandon, 1981)	12
Figure 1-4: Study area depth map on top of Triassic	13
Figure 1-5: FMI wellbore coverage (modified from Schlumberger, 1992, with permission)	16
Figure 1-6: FMI image of fractures and bedding (Schlumberger, 1992, with permission)	17
Figure 1-7: Schematic fracture profile (from Aguilera, 1995)	20
Figure 1-8: Fracture classifications and naming conventions (from Jamison, 1995)	24
Figure 1-9: Kinematic development of a fault propagation fold (modified from Tearpock and Bischke, 1991)	28
Figure 1-10: Inferred strain relationships for a fault-bend fold (from Erickson and Jamison, 1995)	29
Figure 1-11: Buckle fold strain model (modified from Ramsay, 1967)	32
Figure 2-1: Fracture spacing	45
Figure 2-2: Fracture occurrence applied to stereonet contouring and rose diagram fracture frequency	50

Figure 2-3: Predicted fracture spacing along an arbitrary line	51
Figure 2-4: Fracture intercept diagram (fracture density) and fracture flow diagram (fracture volume)	53
Figure 3-1: Well 1 bedding and fracture data	61
Figure 3-2: Well 1 well path	62
Figure 3-3: Well 1 occurrence correction, flow and intercept diagrams	63
Figure 3-4: Well 1 fracture aperture relationships	65
Figure 3-5: Well 1 flow and intercept diagrams by divided units	66
Figure 3-6: Well 2 bedding and fracture data	69
Figure 3-7: Well 2 well path	70
Figure 3-8: Well 2 occurrence correction, flow and intercept diagrams	71
Figure 3-9: Well 2 fracture aperture relationships	73
Figure 3-10: Well 2 flow and intercept diagrams by divided units	74
Figure 3-11: Well 3 bedding and fracture data	76
Figure 3-12: Well 3 well path	77
Figure 3-13: Well 3 occurrence correction, flow and intercept diagrams	78
Figure 3-14: Well 3 fracture aperture relationships	80
Figure 3-15: Well 3 flow and intercept diagrams by divided units	81
Figure 3-16: Well 4 bedding and fracture data	83

Figure 3-17: Well 4 well path	84
Figure 3-18: Well 4 occurrence correction, flow and intercept diagrams	85
Figure 3-19: Well 4 fracture aperture relationships	87
Figure 3-20: Well 4 flow and intercept diagrams by divided units	88
Figure 3-21: Well 5 bedding and fracture data	91
Figure 3-22: Well 5 well path	92
Figure 3-23: Well 5 occurrence correction, flow and intercept diagrams	93
Figure 3-24: Well 5 fracture aperture relationships	95
Figure 3-25: Well 5 flow and intercept diagrams by divided units	96
Figure 3-26: Well 6 bedding and fracture data	98
Figure 3-27: Well 6 well path	99
Figure 3-28: Well 6 occurrence correction, flow and intercept diagrams	100
Figure 3-29: Well 6 fracture aperture relationships	102
Figure 3-30: Well 6 flow and intercept diagrams by divided units	103
Figure 3-31: Well 7 bedding and fracture data	105
Figure 3-32: Well 7 well path	106
Figure 3-33: Well 7 occurrence correction, flow and intercept diagrams	107
Figure 3-34: Well 7 fracture aperture relationships	109

Figure 3-35: Well 7 flow and intercept diagrams by divided units	110
Figure 3-36: Well 8 bedding and fracture data	112
Figure 3-37: Well 8 well path	113
Figure 3-38: Well 8 occurrence correction, flow and intercept diagrams	114
Figure 3-39: Well 8 fracture aperture relationships	116
Figure 3-40: Well 8 flow and intercept diagrams by divided units	117
Figure 3-41: Well 9 bedding and fracture data	119
Figure 3-42: Well 9 well path	120
Figure 3-43: Well 9 occurrence correction, flow and intercept diagrams	121
Figure 3-44: Well 9 fracture aperture relationships	123
Figure 3-45: Well 9 flow and intercept diagrams by divided units	124
Figure 4-1: Occurrence weighted rose diagrams for all wells	126
Figure 4-2: Fracture aperture distributions for each well	130
Figure 4-3: Orientations of large aperture fractures	133
Figure 4-4: Structural position versus fracture density	135
Figure 4-5: Structural position versus open fracture volume	138
Figure 4-6: Fracture density and volume versus lithology	141
Figure 4-7: Optimum drilling inclination and azimuth	145

Figure 4-8: Well drill directions compared to optimal direction	148
---	-----

Chapter 1

Introduction and Background

Introduction

In a recent publication the Triassic trend in northeastern British Columbia (NEBC) was quoted as being, "the most exciting - and successful - frontier play in western Canada" (Montgomery, 1994). The trend, often called the Sukunka-Bullmoose trend, is made up of a number of gas pools in folded carbonates of the inner Rocky Mountain Foothills. The Sukunka-Bullmoose trend is long (approximately 100 kilometers), but narrow (approximately 20 kilometers) and is located west of the British Columbia and Alberta border and south of the Pine River (Montgomery, 1994). In the late 1980's and early 1990's the trend attracted a lot of attention and drilling activity. However, in recent years, industry interest and activity in the trend has declined.

Natural gas is produced from the upper Triassic Pardonet and Baldonnel formations. The reservoir rocks have low matrix porosity (5-10 percent) and permeability (0.01 - 1.0 md), (Rice, 1997). Commercial gas flow is dependent on the structurally formed fractures in complex, folded anticlines. In high production wells, because of the fracture permeability, flow rates of 30-80 mmcf/day are common and absolute open flow (AOF) rates as high as 223 mmcf/day have been recorded (Barss and Montandon, 1981).

The Triassic play is still considered a frontier play in the Western Canadian Sedimentary Basin, a basin that for the most part is very mature. The immaturity of the Sukunka-Bullmoose trend is due in great part to the expensive operational cost of

finding and developing gas resources. Modern 2D seismic acquisition costs approximately \$25,000/kilometer in the rugged terrain of the western foothills. Well costs can exceed \$10,000,000, with expensive road construction and often multiple attempts at reaching narrow drilling targets.

Amoco Canada Petroleum Company Limited was also active in this trend in the late 1980's and the early 1990's. The nine wells that were studied in this thesis were drilled between 1991 and 1996 by Talisman Energy Incorporated, as the operator, with Amoco as a 50% partner. During the well drilling program, the two companies discussed approaches to optimize the drilling program through the folded Triassic reservoir.

Amoco believed that it was important to drill vertically through the steeply dipping front limbs of the folds. They believed that the front limbs were the most intensely fractured portion of the fold and provided the maximum gas flow rates. Amoco's approach was problematic because seismic data were not accurate enough to pinpoint the front limb (the near vertical limbs were poorly imaged on seismic sections). If a well missed the front limb in a foreland position, it was difficult and expensive to redirect the well towards the limb. Talisman supported a more cautious approach and opted for targeting the crest or backlimb position when the crest was narrow.

There were also discussions between the two companies about doing directional short whip horizontal drilling. Both companies believed that there were advantages to drilling "horizontally" (actually parallel to bedding, even if the bed is not horizontal) in the upplunge direction of the fold axis (generally northwest or southeast).

In this thesis, fracture data collected by Formation MicroScanner tool (FMS) and Fullbore Formation MicroImager (FMI) tools in nine wells are interpreted and analyzed

to determine the optimal drilling direction in the folded Triassic of the Sukunka-Bullmoose trend. The goal of the study is to use the fracture and bedding data to characterize fracture morphology, fracture/aperture relationships, fracture/fold structure relationships and to develop a criterion and technique to determine the optimal drilling direction.

The thesis is structured as follows. Chapter 1 provides background information relevant to this study. Chapter 2 details the method of analysis. Chapter 3 examines the data analyses for each well. Chapter 4 discusses the results, comparing wells and recommending how the results can be implemented in future drilling programs. Chapter 5 summarizes the key conclusions and recommends work on unsolved problems resulting from this study.

Study Area

The nine wells were drilled in an area of approximately 320 square kilometers (Figure 1-1), that Amoco calls the Brazion area of northeastern British Columbia (NEBC). The Brazion area is within the larger Sukunka-Bullmoose gas trend. The area is bounded to the south and east by the Sukunka River and bounded to north by the Brazion and Burnt Rivers. The western boundary is just east of the Rocky Mountain Front Range thrust.

The wells were drilled between 1991 and 1996. All nine wells tested gas and some had very encouraging initial rates of over 50 mmcf/day. Seven of nine wells have been tied into a sour gas line and have produced commercial quantities of gas. The remaining two wells have been suspended or abandoned. Although the initial rates were very encouraging, many of the wells will provide less reserves than initially predicted. Amoco

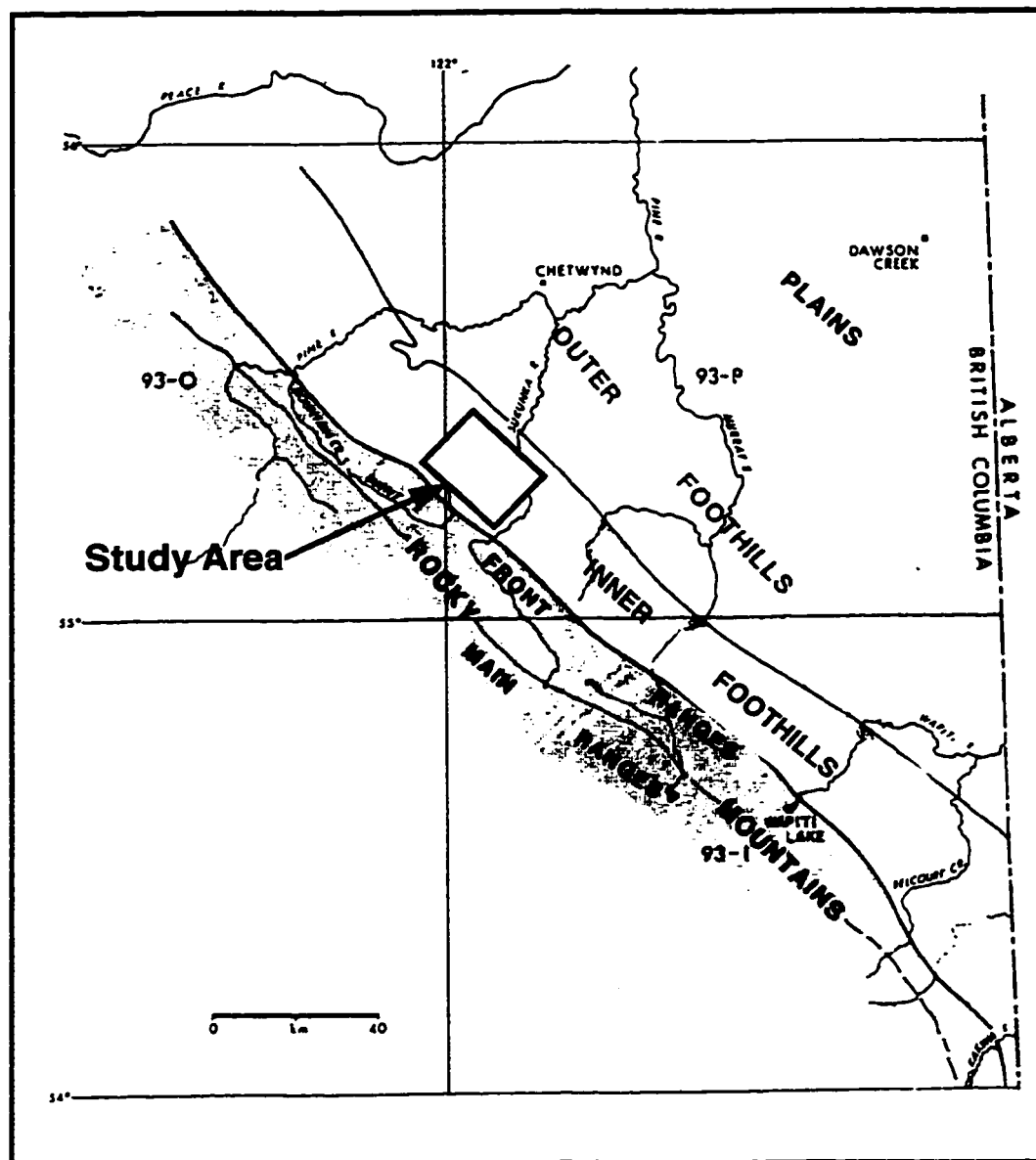


Figure 1-1: Location map (modified from Barss and Montandon, 1981).

The study area is in the shaded box.

reevaluated the area in 1996 and as a result decided to dilute their interest in many of the NEBC foothills properties.

The wells were drilled on several distinct structures and producing pools and intersected the Triassic folds in a number of different structural positions. The nine well data sets provide fracture samples from the crest, forelimb and backlimb of the folds. There are no core data from the wells, however, there is a comprehensive set of modern well logs recorded for each well. The data set used in this study is the largest set used in any published study of NEBC Triassic fracturing.

Stratigraphy

Figure 1-2 shows the stratigraphy in the Sukunka - Bullmoose area of NEBC. Detailed descriptions for the entire section are summarized by Barss and Montandon (1981) and Montgomery (1994). This thesis will not describe the entire section but will focus on the Triassic strata and the Jurassic Fernie shale.

The Triassic stratigraphy in NEBC has been described in numerous studies and papers including: Gibson (1972, 1975, 1992); Barss and Montandon (1981); Gibson and Edwards (1990); Davies (1992); Barclay (1993); Bird et al. (1994) and Montgomery, (1994). The Triassic succession is bounded between two regional unconformities. The base of the Triassic succession is bounded by a Permian unconformity and the top is bounded by an unconformity at the base of the Jurassic Fernie shale (pre-Cretaceous unconformity). Three transgressive-regressive cycles are interpreted during the Triassic Era (Bird et al. 1994).

The Montney Formation is the first transgressive/regressive cycle in the lower Triassic. In the study area, this cycle is an approximately 300 m thick, distal shelf facies,

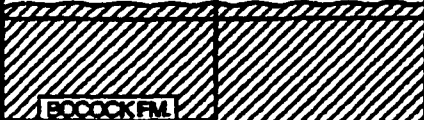
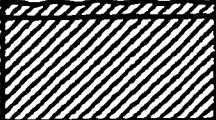

PERIOD / EPOCH / AGE			FOOTHILLS / FRONT RANGES			PLAINS		PLAINS			
			SIKANNI CHIEF- PINE RIVERS		SUKUNDA- BOW RIVERS	PEACE RIVER SUBSURFACE GIBSON & BARCLAY, 1999		PEACE RIVER SUBSURFACE THIS PROJECT			
JURASSIC			FERNE FM.		FERNE FM.		FERNE FM.		FERNE FM.		
TRIASSIC	LATE	RHAETIAN									
		NORIAN								BOCCOCK FM.	
		PARDONET FM.									
	CARNIAN	LUDWINGTON FM.	BALDONNEL FM. Ducette Mbr.	WHITEHORSE	Winnifred Mbr. Brewster 1st. Mbr.	SCHOOLER CREEK GP.	PARDONET FM.	UNIT X = BOCCOCK PARDONET FM. BALDONNEL FM.			
			CHARLIE LAKE FM.		Starlight Evaporite Mbr.		CHARLIE LAKE FM.				
			LIARD FM.		HALFWAY FM.		CHARLIE LAKE FM.				
	MIDDLE	LADINIAN	TOAD FM.	SPRAY RIVER GROUP	SULPHUR MOUNTAIN FM.	Liane Mbr.	DIABER GROUP	DOIG FM.	DIABER GROUP	DOIG FM.	
		ANISIAN				Whistler Mbr.		MONTNEY FM.		MONTNEY FM.	
		SPATHIAN				Vega Silt. Mbr.		Vega-Phreco Silt. Mbr.			
		SMITHIAN	Phreco Silt. Mbr.								
DIENERIAN		GRAYLING FM.									
GRIESBACHIAN											
PERMIAN			ISHEEL GROUP								

Figure 1-2: Triassic stratigraphic section (from Rice, 1997, modified from Davies 1992).

composed of mainly siltstone and shale (Barss and Montandon 1981; Montgomery 1994). To the east, the Montney facies represents a shallower water environment. At the base is a transgressive sandstone topped by a prograding shore facies which includes calcareous and dolomitic siltstones (Montgomery 1994).

The second cycle includes, from bottom to top, the Doig, Halfway and Charlie Lake formations. The Doig Formation is approximately 75 m thick. The base of the Doig Formation is marked by a highly radioactive conglomerate lag (Montgomery 1994). This is overlain by calcareous siltstone and carbonaceous shale that thins from west to east (Montgomery 1994). The upper Doig section coarsens upward into the Halfway shoreface sands (Montgomery, 1994). The sequence continues to shallow into the overlying Charlie Lake Formation (CLLK). The Charlie Lake is an evaporitic sequence, approximately 350 m thick in the study area (Barss and Montandon, 1981). It comprises anhydrite, dolomite, sandstone and siltstone (Barss and Montandon, 1981).

At the top of the Triassic section, the last transgressive/regressive cycle includes the reservoir rocks in the Brazion area. The last cycle is divided into the Baldonnel and Pardonet formations. The Baldonnel Formation is the lower formation and marks the onset of a marine transgression over the restricted and saline environment of the Charlie Lake evaporites (Davies, 1992). The Baldonnel Formation is approximately 50 to 80 m thick in the Sukunka-Bullmoose area and is a shallow water carbonate facies consisting of limestone, dolostones, argillaceous siltstones and fine grained sandstone (Montgomery, 1994). The Pardonet Formation represents deeper water outer shelf facies (Davies, 1992) and is a mixture of carbonaceous and argillaceous limestone,

siltstones, dolostones and shale (Montgomery, 1994). The Pardonet Formation is approximately 60 m thick in the Brazion area.

The Baldonnel and Pardonet formations have each been divided into four sub-units, (B1 to B4 for Baldonnel and P1 to P4 for Pardonet, numbered from bottom to top), based on gamma and sonic log signatures (Barss and Montandon, 1981). The lower two units, B1 and B2, are largely dolomitized and are the primary reservoir rock in the Brazion area (Rice, 1997). The Baldonnel B3, B4 and Pardonet P1, P2 units have less dolomite and more sandstone, silt and limestone (Rice, 1997). The B3, B4, P1 and P2 units were deposited during a slight regression (Rice, 1997). The Pardonet P3 unit changes from a shallow marine facies in the east to a slope and distal slope facies to the west (Rice, 1997). In the eastern part of the Brazion area, the P3 unit is dolomitized and provides a second reservoir. To the west the P3 unit is not a reservoir facies. The Pardonet P4 unit changes quickly from east to west, from shelf to distal slope pelagic sediments. The P4 unit is not a reservoir unit.

The top of the Pardonet is marked by a disconformable surface (Montgomery, 1994). The Jurassic Fernie Formation overlies the unconformity. The Lower Fernie section consists of a carbonaceous shale, thin siltstones, and black, phosphatic limestone (Montgomery, 1994). This lower section is considered to be both the seal and source rock for the Upper Triassic reservoirs. The Upper Fernie section coarsens upward from a shale at the base to interbedded shale and fine grained sandstone (Montgomery, 1994). The Fernie is approximately 250 - 350 m thick in the Brazion area.

Structural Geology

There are significant changes in the structural style of the Canadian Rocky Mountains between Alberta and NEBC (Fitzgerald, 1968; Thompson, 1979, 1982, 1989; McMechan, 1985, 1987; McMechan and Thompson, 1989, 1993; Montgomery, 1994). In the south, the orogen is built up of large, continuous thrust sheets. The southern part of the orogen can be divided into four distinct provinces defined by large but distinct thrust complexes (Montgomery, 1994). The large thrust sheets in the southern Canadian Rockies are replaced by smaller, less continuous thrust faults and tight folding in NEBC. In NEBC there are three distinct provinces (Thompson, 1989). The Outer Foothills on the eastern side of the belt are distinguished by low amplitude subsurface structures with very little topographic expression. To the west, there is a sharp boundary between the Outer and Inner Foothills, where the subsurface folds become higher in amplitude and are clearly expressed by surface topography. The Inner Foothills are bordered to the west by the Rocky Mountains which are generally marked by a thrust that carries Paleozoic rocks that form outcrop ridges.

Thompson (1989), argues that the change in structural style between the north and south is primarily due to changes in stratigraphy. In the south, the sequences are dominated by massive carbonates separated by thinner shales. These large carbonate sheets are difficult to fold and instead, are shortened by duplication through thrust faulting. To the north, the facies are in a more distal position. The thinner competent beams are separated by thicker sections of structurally incompetent shales. Shortening by folding is possible because the competent beams can bend and buckle between detachment horizons within the thicker incompetent section.

Beattie (1984) compared changes in structural style at two locations in Devonian strata, that supported the importance of stratigraphy on structural style. He compared the structures associated with the Bare Thrust at Rough Mountain and Mt. Michener. The facies in the lower Fairholme Group change from carbonate reef facies (Rough Mountain) to a shale channel facies (Mt. Michener). In the carbonate facies the structures are simple broad parallel folds. The folds are more complex and tighter with similar type folding in the shale facies.

Physical centrifuge modeling has been used to simulate changes in structural style due to changes in lithology. Dixon (1995) designed a model that is similar to Beattie's (1984) field study. The model was designed using material of different strengths to represent competent and incompetent rocks. Three different geologic facies were modeled. Competent material was used to model the on-reef facies. A mix of competent and incompetent material was used to model a mixed reef/basin facies. Incompetent material was used to model the basin, off-reef facies.

Dixon (1995) deformed the model in a centrifuge and the structural style for each simulated facies was observed. The modeled on-reef facies tended to deform by thrust faulting. The modeled mixed facies tended to deform by broad folding instead of by thrust faulting. The modeled off-reef facies deform by tighter and more complex folding.

Within the Inner Foothills of the Sukunka-Bullmoose trend, the structural style is consistent with the folding observations described above. The Upper Triassic is a relatively thin competent beam (Pardonet plus Baldonnel thickness is between 80 - 150 m) between the two potential, major incompetent detachment surfaces. The upper detachment horizon is the Jurassic Fernie (approximately 300 m thick) shale and the

lower detachment horizon is the Lower Triassic Montney Formation (approximately 300 m thick) (Montgomery 1994). As a result, the structural style of the Upper Triassic is dominated by complex tightly folded/faulted anticlines, with a NW/SE axial trend (Barss and Montandon, 1981).

Barss and Montandon (1981) provided a series of structural cross sections, based on well data, confirming the above folding model. The sections showed folded structures that are northeast-verging with gentle backlimbs, steep forelimbs and sharp hinges (Figure 1-3). Many of the forelimbs are broken by small displacement thrust faults. The fold amplitudes are up to 800 m and usually involve the underlying Halfway Formation, (Cooper, 1991).

The Brazion study area is within the Inner Foothills structural province. The folds in the study area are tight and northeast-verging, however, the degree of asymmetry differs between structures (Figure 1-4). The structures are long and narrow with widths between many of the anticlines less than 2 km. However, the structures appear to continue along the axial plane strike for 10 km to over 20 km.

Figure 1-4 shows the well locations relative to the Brazion area structures. Wells 1 and 2 are drilled into the deepest (subsea depth) and most eastern structure. Well 3 was drilled into what appears as a strike continuation of the Well 1 and 2 structure. However, these two structures are separated by a significant saddle. To the west, a series of four shallower anticlines are positioned on a broader regional anticline. The regional anticline culminates to the south, in the West Sukunka Anticlinorium. Wells 4 to 7 are drilled on folds positioned on the regional high. A deep broad syncline separates the regional

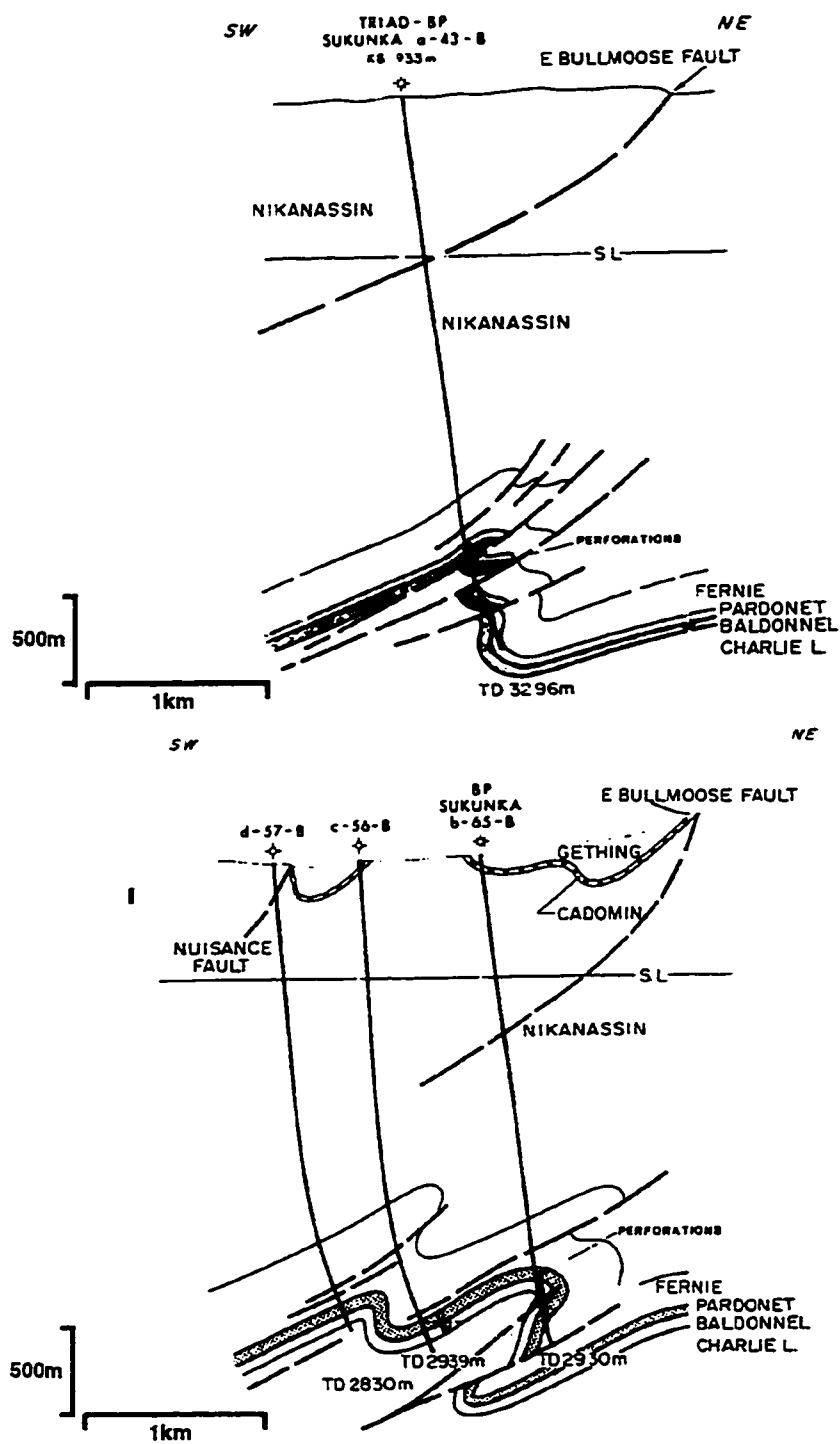


Figure 1-3: Folding style (modified from Barss and Montandon, 1981).

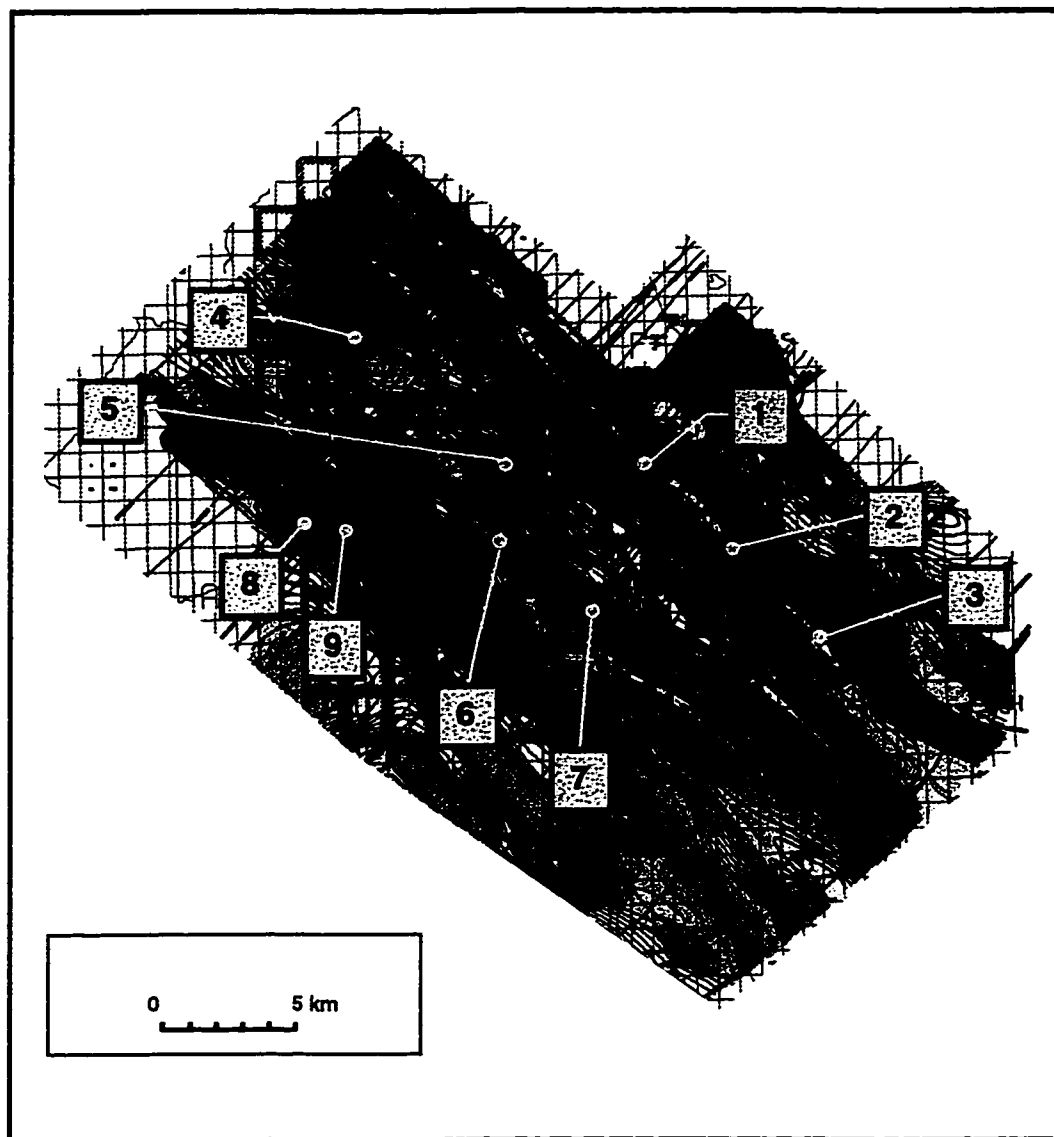


Figure 1-4: Study area depth map on top of Triassic.

The depth map is based on 2-D seismic control. Reds are higher subsea elevations than blues. The well positions are shown by the yellow dots.

anticline from structures to the west. Wells 8 and 9 are on two anticlines on the western side of the syncline.

The structures in the eastern portion of Figure 1-4 are near the eastern edge of the Inner Foothills. Structures on west side of Figure 1-4 are just east of the first thrust that carries carbonate rocks to the surface and marks the eastern boundary of the Rocky Mountains. It is generally accepted that the Upper Triassic structures become more complex and faulted to the west (i.e. structures associated with Wells 8 and 9 would be more complicated than those penetrated by Wells 1 and 2) (Barss and Montandon, 1981; Montgomery, 1994). The seismic and well data in this area do not support such a hypothesis. For example, on one depth-imaged 2D seismic line in this area, the entire front limb was imaged on the structure associated with Well 9. There was very little seismic evidence that the front limb was significantly faulted. In addition, Wells 8 and 9 revealed typical Triassic folding that was not overly complex.

Fracture Measurements From the FMI/FMS Tool

Bedding and fracture data used for the nine wells are interpreted from either FMS (Formation MicroScanner) or FMI (Fullbore Formation MicroImager) tools. Both tools function in the same way, but differ in resolution and the amount of borehole coverage. The FMS tool, Schlumberger's first resistivity imaging tool, was introduced in the mid-1980s. This FMS tool is available with either two or four pads of resistivity buttons, (two pad tool used in slim holes less than 16 cm in diameter). The FMI tool was introduced in 1991 to provide better resolution and coverage. The FMI tool has eight pads with 24 resistivity buttons per pad or a total of 196 resistivity buttons. In a 20 cm diameter borehole, with all buttons on, the FMS four-pad tool will cover 40% of the hole whereas

the FMI tool will cover 80% of the hole. The resolution, or the ability to distinguish separate fractures or beds, of the FMS four-pad tool is 7.5 mm whereas for the FMI tool it is 5 mm (Schlumberger, 1992). In general, wellbore coverage decreases as the hole diameter increases (Figure 1-5).

The tools operate in the same way as a conventional resistivity tool, however wellbore images are made by using a large number of electrodes or buttons. The images are produced by changes in the electrical current flowing between the upper electrode, housed at the top of the tool and the lower buttons located on pads at the base of the tool. The high frequency alternating current is modulated by microresistivity changes in the rocks nearest the button electrodes. Lower frequency alternating current is modulated by resistivity changes deeper in the formation (further from the borehole). The high frequency component is used to produce the images relating to lithology and fractures. Lower frequency data are needed to calibrate the high frequency data when doing fracture aperture measurements (Schlumberger, 1992).

The tools are equipped with an inclinometer that measures tool acceleration, for speed corrections, as well as borehole orientation measurements. The accuracy of the bore hole orientation is 2 degrees in azimuth and 0.2 degrees in deviation from vertical (Schlumberger, 1992). The tools are limited to operating in low resistivity drilling muds. The FMI tool operates best in water based drilling fluids with resistivities below 50 ohm-m (Schlumberger, 1992).

The analog electrical signals from the buttons are converted to digital signals and are processed into digital images. The images are represented in color with a scale from white, through orange, to black (Figure 1-6). The lighter images represent resistive

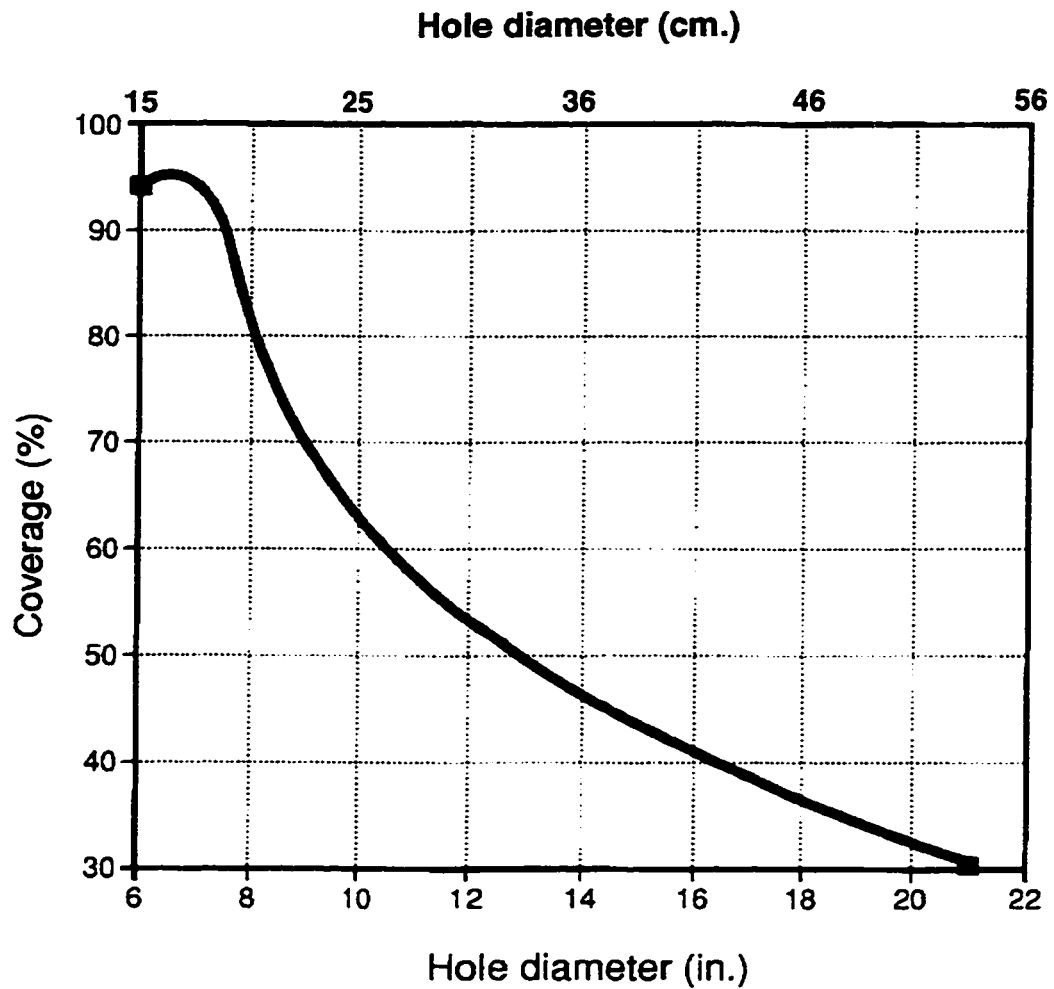


Figure 1-5: FMI wellbore coverage (modified from Schlumberger, 1992, with permission).

The curve shows the percent of wellbore coverage as a function of hole diameter.

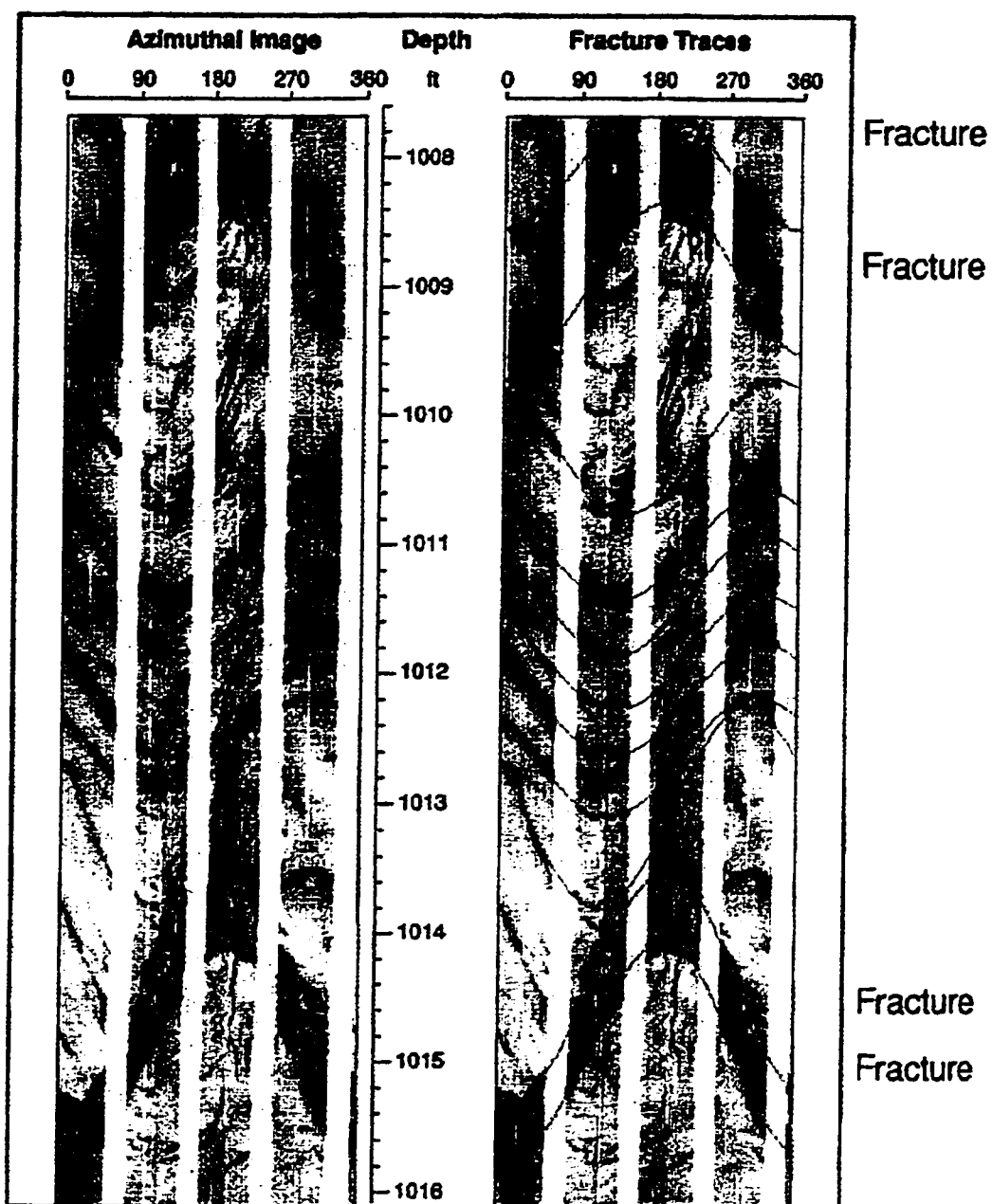


Figure 1-6: FMI image of fractures and bedding (Schlumberger, 1992, with permission) .

The blue curves show the planar open fractures on the image. The red lines show bedding planes. The orientation differences between the fractures and bedding are easily distinguished in this example.

material or low currents and are typical in tight rock that is not invaded by the drilling fluids. Darker images represent more conductive zones or higher currents and are a typical response of higher porosity zones or open fractures. The resistivity also depends on the lithology of the rock. Zones of high clay content are more conductive or darker, whereas zones of small grain size or higher amounts of carbonate or anhydrite are more resistive or lighter (Schlumberger, 1992).

The wellbore is represented as a two dimensional image for interpretation on a workstation. The image represents an “unrolling” of the 3D wellbore surface into a 2D image. The left edge of the image is typically the north orientation. From left to right, the image increases azimuth from north to east to south to west and back to north, or from 0 to 360 degrees. A planar surface, for example a fracture or bed, cutting the well bore at an angle will appear as a sine wave on the 2D image. The sine wave images can be automatically picked using Schlumberger software. These “picks” are then edited and augmented by an interpreter.

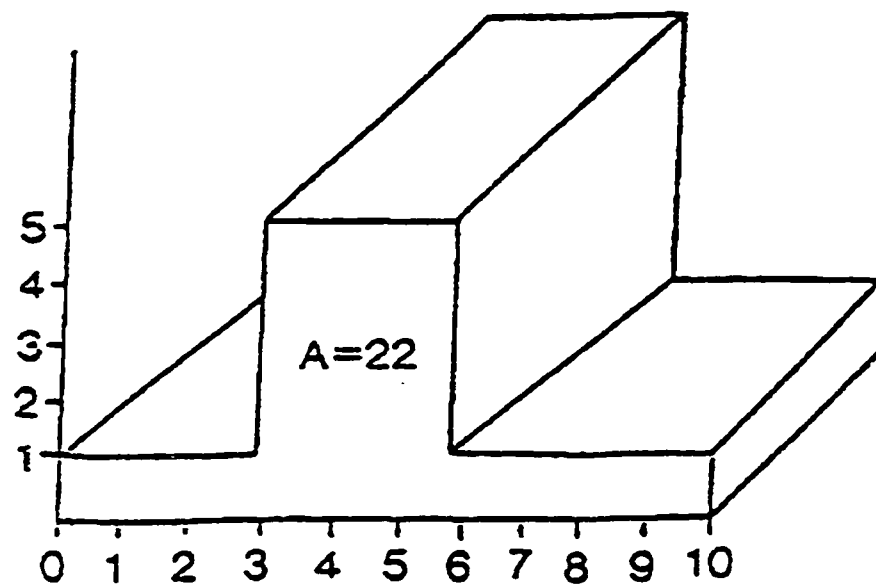
The amplitude of the sine wave measures the amount of dip on the interpreted plane relative to the wellbore. In a vertical well, a large sine wave amplitude represents a steeply dipping plane. However, the relationship between amplitude and dip is not as apparent in deviated wellbores. For example, in a horizontal well, gentle dips will have large amplitudes or the opposite relationship to vertical wells. The apparent dip is corrected to true dip and spatial orientation, transparent to the user, by the Schlumberger software.

Image interpretation requires knowledge of the geological section and skill as an FMI/FMS interpreter (interpretation examples and techniques are shown in papers by

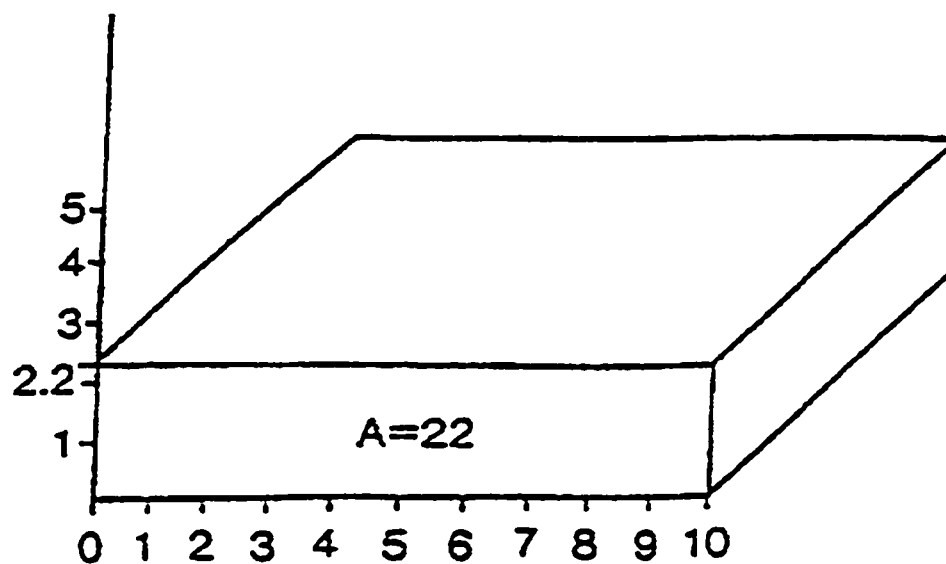
Bourke, 1989 & 1992; and Harker et al., 1990). The interpreter must be able to distinguish between bedding and fracture planes. Also, the interpreter must distinguish between natural fractures and drilling-induced fractures. Interpretation is especially challenging when the geologic section is complicated by severe changes in bedding dips and faulting. The best interpretations are made by a skilled interpreter who examines other data such as well logs and core, if available, or drilling samples.

Once the fractures are interpreted and distinguished from bedding planes, aperture calculations can be made. Fracture aperture is important because it enhances rock permeability which allows for higher gas flow rates. Schlumberger software can calculate two different aperture measurements, mean fracture aperture and hydraulic fracture aperture. The mean fracture aperture measures the width of the fracture opening. Hydraulic fracture aperture is the measurement that relates to gas flow from the reservoir. Aguilera (1995) described the difference between these two different aperture measurements. A summary of Aguilera's (1995) description follows.

Figure 1-7 shows a schematic diagram of two fractures with different aperture profiles. Fracture 1 has variable fracture aperture, with a wider aperture in the center as compared to the sides. Fracture 2 has a constant fracture aperture. In cross-section, both fractures have the same area, 22 units. The mean fracture aperture is the arithmetic mean of the fracture apertures measured at different positions along the fracture. The arithmetic mean is the same for both fractures, that is, $22/10$ or 2.2 units. The hydraulic aperture is the cubic mean of the fracture aperture. It is calculated as the cube root of the sum of the cubes of each width element along the fracture profile. For Fractures 1 and 2 shown in Figure 1-7, the cubic means are:



FRACTURE 1



FRACTURE 2

Figure 1-7: Schematic fracture profile (from Aguilera, 1995).

The two fracture aperture profiles have the same arithmetic mean apertures but different hydraulic apertures. Gas will flow 3.6 times faster out of fracture 1 than fracture 2.

$$\text{Fracture 1: } F_{AH1} = \sqrt[3]{(3(1.0)^3 + 3(5.0)^3 + 4(1.0)^3) / 10} = 3.368,$$

$$\text{Fracture 2: } F_{AH2} = \sqrt[3]{10(2.2)^3 / 10} = 2.2$$

In the above example, both fractures have the same mean fracture aperture or there is the same amount of fracture opening exposed in the fracture profile. However, Fracture 1 has a larger hydraulic fracture aperture which is a more efficient conduit for flow. The flow rate is proportional to the hydraulic aperture cubed, that is, $q \propto F_{AH}^3$, where q is flow rate and F_{AH} is hydraulic fracture aperture. Therefore the relative flow rate difference between the two fracture profiles is:

$$\left(\frac{F_{AH1}}{F_{AH2}}\right)^3 = \left(\frac{3.368}{2.2}\right)^3 = 3.588.$$

The above ratio shows that Fracture 1 will theoretically flow at a rate 3.588 times faster than Fracture 2.

The apertures used in this thesis are calculated in Schlumberger software package FracView. The aperture calculations are done by the software using an inverse finite-element model. The finite-element approach is outlined in a paper by two Schlumberger researchers (Luthi and Souhaite, 1990). The aperture model is dependent upon the ratio of actual formation resistivity to the mud resistivity. Accurate measurement of mud resistivity is critical to absolutely calibrate the imaged aperture to the true fracture aperture size.

The inverse model (Luthi and Souhaite, 1990) was used in aperture measurements of fractures in basement rock in Moodus, Connecticut. In the basement rock, computed fracture apertures ranged in size from 10 μm to 1 mm. The vertical resolution between fractures was approximately 1 cm apart. Luthi and Souhaite (1990) also compared the

calculated fracture apertures to aperture measurements from in situ Stoneley wave reflection measurements. There was good agreement between these two approaches for the wider aperture fractures.

Aguilera (1995) has used aperture measurements from FMI/FMS logs to compare production rates between wells. From his experience, fracture aperture measurements from the logs are a good measurement of relative fracture aperture within a wellbore, but are poor absolute measures between wells. He found that a calculated large fracture aperture in a well does not necessarily mean good productivity when compared to a small fracture aperture in an offset well. Errors will result if the mud or formation resistivity for the flush zone or mud-invaded zone are not accurately known. In addition, the finite-element model makes assumptions about the fracture morphology that may not be appropriate in many cases.

Fracture Classification

Fracture classification can be subdivided into three different types of classifications. One classification arises from rock lab experiments (Stearns and Friedman 1972; Nelson, 1985; Aguilera, 1995) where three fracture types have been classified: shear, extension and tension fractures. Shear fractures occur when movement on the fracture surface is parallel to the fracture surface. An extensional fracture occurs when the fracture aperture increases by movement normal to the fracture plane, i.e. movement parallel to the minimum principal stress direction. The minimum principal stress can be compressive or tensile. If the fractures are known to have formed under a tensile minimum principal stress regime, they are tension fractures. It is impossible to distinguish between extension and tension fractures unless the orogenic stresses are

known. In general, fractures in core and in the field studies are defined as either shear or extension (including tension) fractures.

Fractures can also be classified from a geological point of view as either regional fractures or tectonic fractures, (Stearns, 1968; Stearns and Friedman, 1972; Nelson, 1985; Aguilera, 1995). Regional fractures occur over large areas and change orientation only gradually over long distances. They tend to occur in two orthogonal sets at high angles to bedding. Tectonic fractures are associated with local geological structures. These fractures can be associated with local faulting and folding, resulting from basin extension, compression or shear.

The third classification of fractures is a subset of fracture groups that are associated with tectonic fractures and folding. There are eleven potential fracture sets associated with a simple fold (Stearns and Friedman, 1972). These different sets result from all possible orientations of the three principal stresses relative to the fold axis. A complete system of fractures would include two shear fractures and one extensional fracture. In rocks, the acute dihedral angle between the conjugate shear fracture planes usually approximates 60 degrees and is bisected by an extensional fracture.

Of the eleven possible fracture sets, only four are usually observed in the field and only two are commonly found (Stearns and Friedman, 1972). Stearns' four fracture sets are shown in Figure 1-8. The two most common sets are Types 1 and 2. The less common sets are Types 3a and 3b. The two common sets will be discussed in detail below.

Type 1 fractures result when the maximum principal stress, σ_1 , is parallel to the dip direction and in the same plane as bedding. The intermediate stress axis, σ_2 , is normal

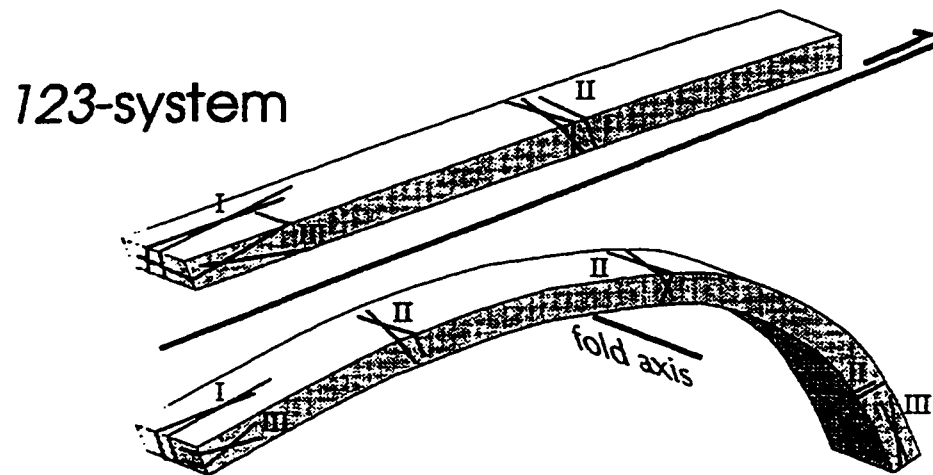
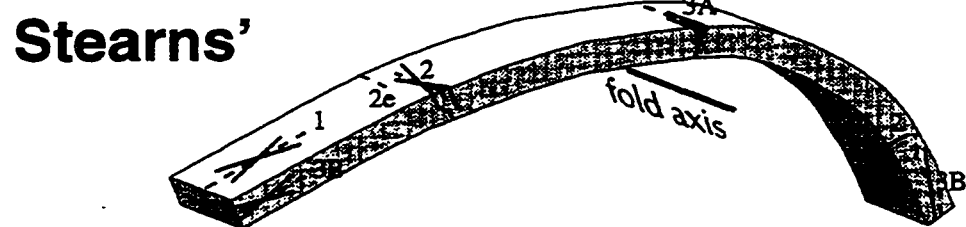
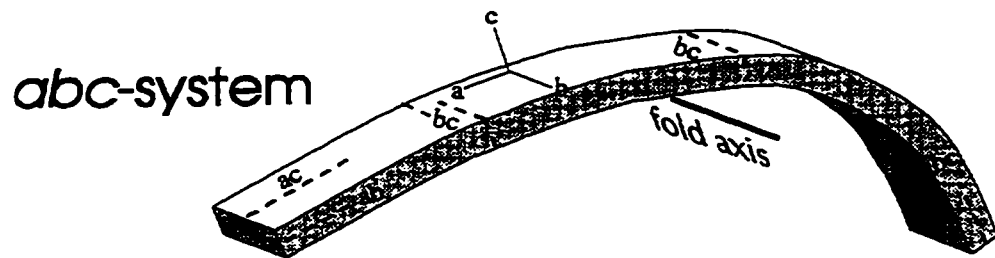


Figure 1-8: Fracture classifications and naming conventions (modified from Jamison, 1995).

to bedding and the least principal stress, σ_3 , is parallel to the strike of bedding. The extensional fracture is parallel to the bedding dip direction and the shear fractures would be approximately 30 degrees oblique to the dip direction. These fractures result in shortening of bedding in the dip direction and elongation in the strike direction.

Type 2 fractures result when σ_1 is parallel to the strike direction and in the same plane as bedding. The intermediate stress axis, σ_2 , is normal to bedding and the least principal stress, σ_3 , is parallel to the dip direction and in the same plane as bedding (i.e., the stress orientations are rotated by 90 degrees about the intermediate stress axis as compared to the stress directions for Type 1 fractures). The extensional fracture is parallel to the trace of the fold axis on the bedding and the shear fractures would be approximately 30 degrees oblique to the trend of the fold axis. These fractures result in shortening of bedding in the strike direction and elongation in the dip direction.

Stearns' classification assumes that the fracture geometries are the result of specific principal stress orientations. For example, Type 1 fractures, according to Stearns' classification, have extensional fractures parallel to the dip direction and shear fractures at oblique angles of approximately 30 degrees to the dip direction. In field observations, this is found in some cases to be correct but, in other instances, the orientations do not match observed extension/shear properties (Jamison, 1995). Jamison (1995) simplifies Stearns' classification by reducing fracture classifications to a I, II, and III orientation scheme. The fractures in Jamison's classification have the same orientations as Stearns' classification, but do not presume a specific orogenic control. Jamison's classification is purely based on fracture geometry and groups the shear and extensional conjugate pairs into a single set. For example, Stearns' Type 2 shear and

extensional fractures become Jamison's II fractures. Jamison's typing of fractures is similar to the abc system commonly used, but is much less confusing. A comparison between these three classifications is shown in Figure 1-8.

In this thesis, Stearns' classification will be used to describe fracture orientations and not to distinguish whether the fractures were formed by shear or extensional movement. Jamison's classification will also be used to describe the general orientation of fracture sets. The abc system will not be used.

Stearns' and Jamison's classifications of fracture orientations are made relative to the bedding planes and not to an absolute spatial position. Fracture orientations collected from different dip domains on a fold do not typically group into persistent sets of fracture geometries (e.g. Burger and Thompson, 1970). However, fractures will group into sets if their orientations are appropriately measured relative to bedding. Another method to accomplish the grouping of fracturing into sets is by rotating the fractures by an amount that would rotate the corresponding bedding dip domain to horizontal. The bedding rotation should attempt to reverse the folding process or unfold the fold. A common two step approach to unfold a plunging fold is to first rotate the plunging fold axis to horizontal, rotating the fractures and bedding dip domains by the same amount. Then the structure is unfolded by rotating each bedding dip domain (and its associated fractures) around the fold axis to horizontal.

Fracturing Inferred from Fold Models

Fold models are used to help predict fracture orientations and locations. Three models, fault propagation folding, fault-bend folding, and detachment or buckle folding, are presented below. The implications of these models on fracture prediction are

discussed for the models. The relevance of these models to the observed folding in Upper Triassic strata of NEBC is also considered.

Cooper (1991) examined a well drilled into an upper Triassic anticline in the Sukunka-Bullmoose trend. Cooper (1991) described the anticline as being caused by a tip fold terminating in the Charlie Lake Formation. The fault was interpreted as ramping up from the Toad/Grayling shales, carrying the Halfway Formation in the hanging wall. The small displacement faults in the front limb are not connected to the main tip fault, but are smaller faults terminating in the Charlie Lake Formation. Although there was no direct evidence of the fault in the Charlie Lake Formation, Cooper (1991) claimed that seismic evidence (not provided in the paper) supported the fault interpretation.

The tip fold model suggested by Cooper (1991) is the same model as Suppe's (1985) fault propagation fold model. Figure 1-9 illustrates the kinematic progression of a fault propagation fold. The fold develops as the fault tip ramps up through the stratigraphy. To compensate for increased displacement along the fault, the fold gains amplitude. As the fold develops, the hinges A and A', (and similarly B and B'), migrate away from each other. All the hinges are migrating with beds between A and A' (and similarly B and B') having either passed through A, from the crest to the front limb, or through A', from in front of the fold into the front limb.

Erickson and Jamison (1995) developed a kinematic finite-element model for the Suppe (1985) fault-bend fold. Strain relationships were inferred from the modeled stresses. Figure 1-10 shows the possible strain that could occur as beds passed through the flat-ramp-flat fault geometry. Extensional fracturing is inferred as bedding passes through the hinges due to changes in the fault plane. In Area 2, as the beds

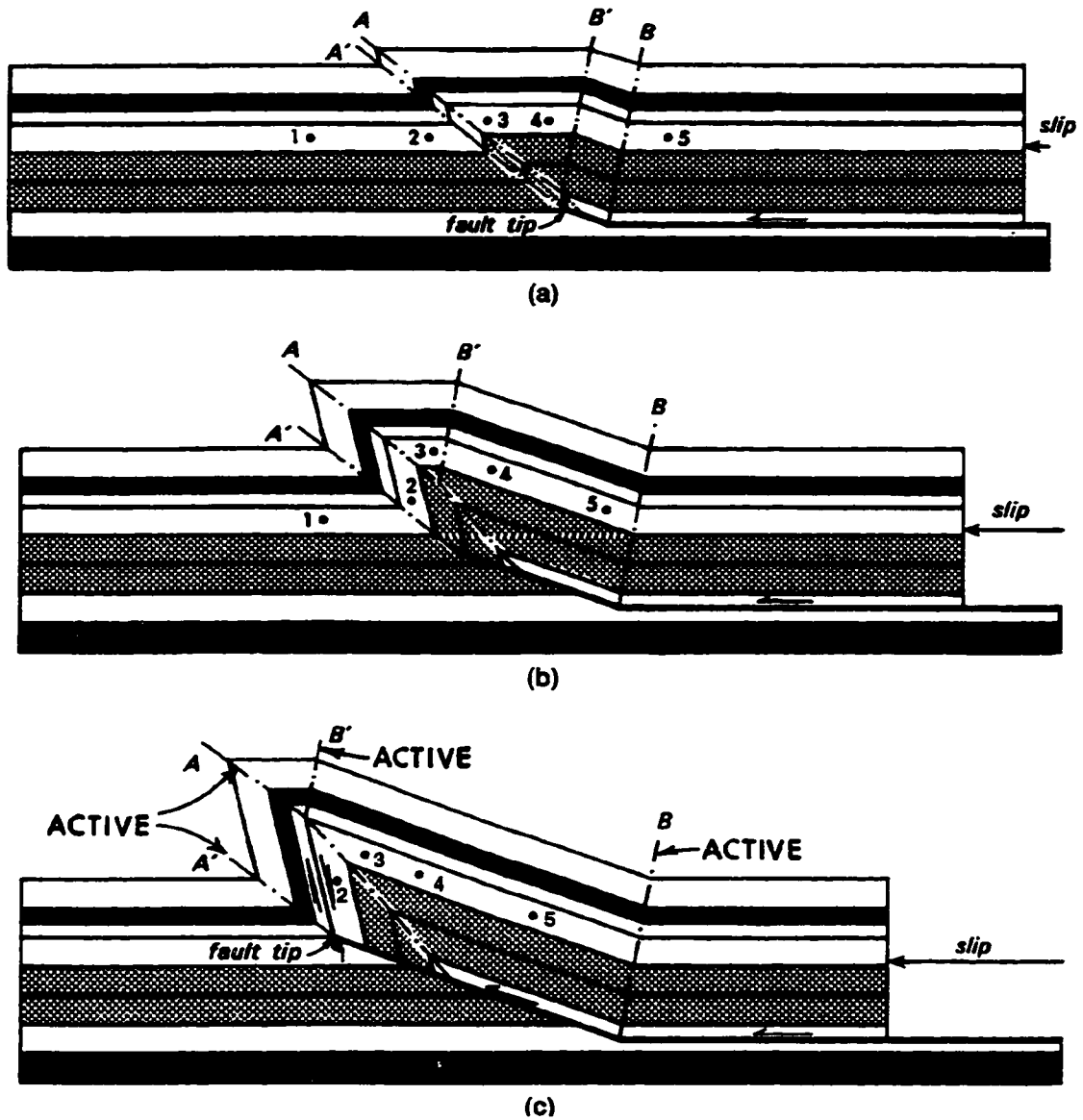


Figure 1-9: Kinematic development of a fault propagation fold (modified from Tearpock and Bischke, 1991).

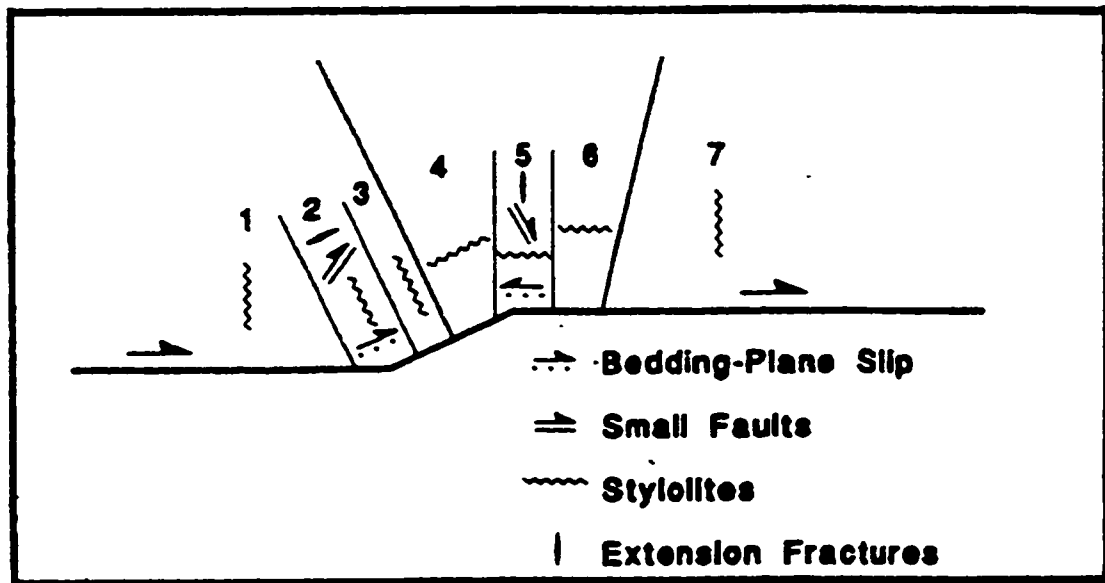


Figure 1-10: Inferred strain relationships for a fault-bend fold (from Erickson and Jamison, 1995).

climb up the ramp from the flat, transport-parallel extension fractures develop. These would be classified as III fractures, i.e. bedding parallel. In Area 5, as the beds cross from the ramp into the flat, transport-parallel extension fractures develop. These would be classified as II fractures, i.e. bedding perpendicular and parallel to strike. The strain model implies the formation of different stylolite orientations through the deformation process. Usually, stylolites are considered to impede flow through the rock. In addition, unlike open fractures, stylolites may not be apparent on FMI/FMS data.

A fault-bend fold is a simpler stress model than a fault propagation fold. For the fault-bend fold model, the fault plane is fixed and the hanging wall deforms as it passes over the flat-ramp-flat geometry. For the fault-propagation fold model, the fault plane extends as the fault tip propagates up the section. However, similarities between the kinematic models can be inferred. The beds fold at the hinge lines A' and B (Figure 1-9) in an analogous way to Area 2 (Figure 1-10). The resulting fractures on the tip fold model could be inferred as III type fracturing. The beds fold at the hinge lines A and B' (Figure 1-9) in an analogous manner to Area 5 (Figure 1-10). The resulting fractures on the tip fold model could be inferred to be II type fractures.

If Upper Triassic folding developed as a fault propagation fold, II type fractures will be present near the areas of the hinge lines at the crest (Figure 1-9). These fractures should extend down both limbs through all points that A' and B have migrated through. Towards the base of the limbs, III type fractures should be present. One would expect greater fracture intensity on the front limb side because of the increased bending of the beds through hinges A and A' as compared to B and B'. Strictly speaking, there should be less fracturing on the crest because it never passes through a migrating hinge.

Detachment folding is an alternative model for Upper Triassic folding. Detachment folding assumes the detachment horizon forms parallel to sub-parallel to bedding, below the fold. As the fold rises above the detachment surface, incompetent material must move in to fill the void. In the models, the folds are usually presented as being either symmetric, concentric buckle folds or angular symmetric or asymmetric folds. The hinges can either be fixed (relative to bedding) or migrating.

Ramsay (1967) examined the folding and fracturing of rock in a buckle fold model (Figure 1-11). Figure 1-11a shows an idealized buckle fold with strain ellipses. In the upper layers of the crestal region, the rock strain is extensional. The resulting fractures would be Type 2 open fractures (Figure 1-11b). Down through the fold at the hinge the strain decreases to a neutral surface. At the neutral surface there is zero strain and little fracturing should occur (Figure 1-11b). Below the neutral surface, the strain will become compressive. In this zone, the strain will be accommodated by vertical stylolites or small reverse faults. Type 3 fractures that occur in the lower zone would be associated with faulting and should be less open and possibly at lower angles to bedding.

Ramsay's (1967) strain relationships are reversed in the synclines. The upper units of the syncline will have compressional stress with Type 3 faulting and stylolite strain. Below the neutral surface, the strain is extensional with open Type 2 fractures.

There are several problems with applying Ramsay's (1967) ideas to NEBC. Firstly, the Triassic folds tend to be sharp hinged folds rather than concentric buckle folds. In the hinge, Ramsay's model is more applicable. Away from the hinge, in zones of no curvature, Ramsay's model does not predict strain patterns. Secondly, to apply Ramsay's model to fracture prediction, the position of the neutral surface must be

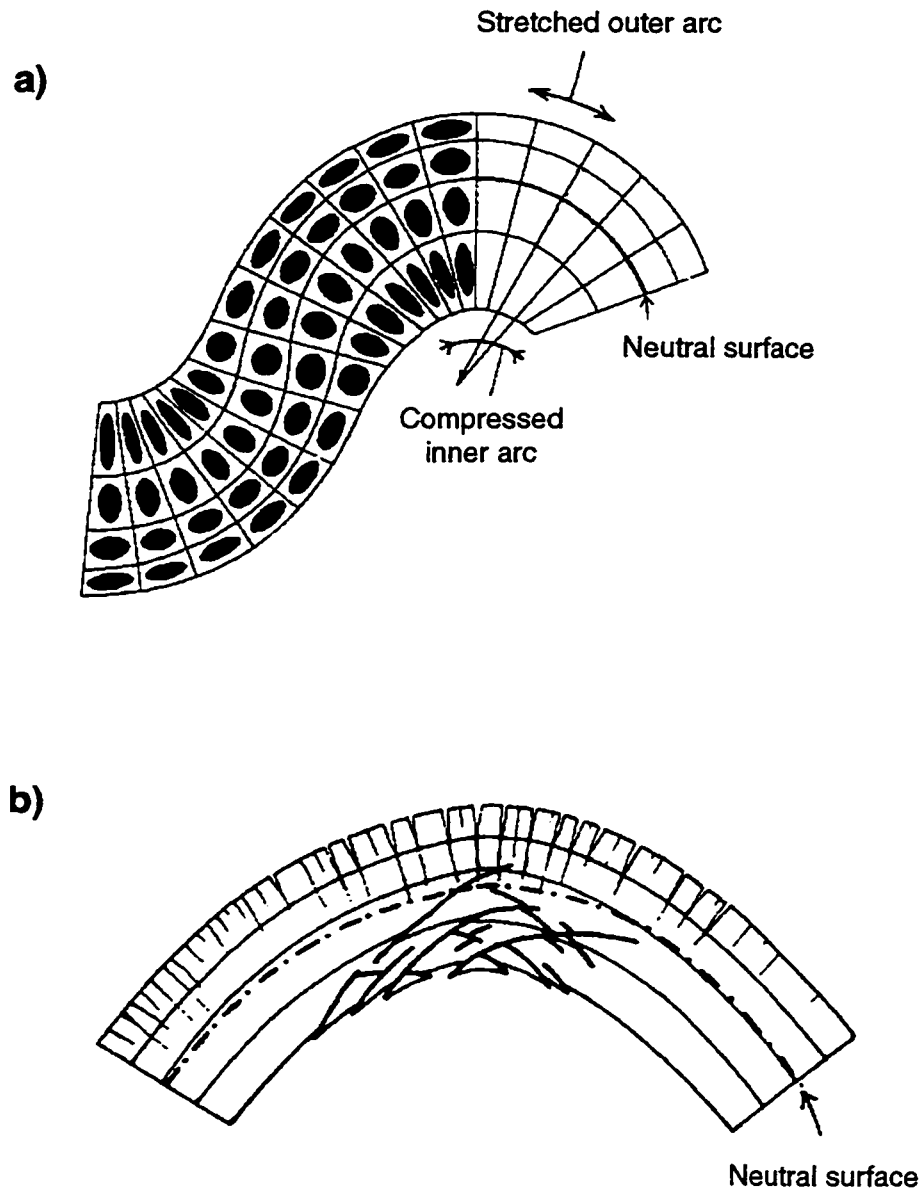


Figure 1-11: Buckle fold strain model (modified from Ramsay, 1967).

Figure 1-11a shows the strain ellipses for a buckle fold model. Extensional strain occurs above the neutral surface in the crest and below the neutral surface in the syncline. Compressional strain occurs below the neutral surface in the crest and above the neutral surface in the syncline. Figure 1-11b shows the expected strain on the crest of the buckle fold.

known. The surface must be bounded between the upper and lower fold detachment surfaces. In the Triassic, the lower detachment is likely in the Montney shales. The upper detachment is in the Fernie shales or above in the Cretaceous shales.

Unfortunately, with these broad band detachment levels, the neutral surface could be either above, below or within the Pardonet or Baldonnel Formations. Not knowing the position of the neutral surface makes applying Ramsay's model to prediction of fracturing in the upper Triassic difficult. Lastly, Ramsay's model assumes homogeneous rock. The rocks between the Triassic detachments are layered with different lithologies and there are likely multiple neutral surfaces and multiple layers of strain patterns.

Homza and Wallace (1995) investigated the kinematic development of angular detachment folds. Through geometric arguments they demonstrated that both symmetric and asymmetric folds could be formed above a single detachment surface, however the hinges must migrate. If the detachment depth is allowed to vary, there is a wider range of geometries and kinematic developments that are possible; both symmetric and asymmetric folds with either fixed or migrating hinges can occur.

The geological implication of Homza and Wallace's (1995) kinematic model is that if the incompetent detachment zone is relatively thin and constrained, then only detachment folds with migrating hinges can form. The migrating hinge model would predict fracture characteristics similar to the fault propagation fold model. That is, fractures form as the bedding plane passes through the hinge zone. Fracturing will intensify when bedding passes through hinges with increasing curvature. Therefore, for the asymmetric folds in NEBC, the fracturing should be more intense in the front limb than the backlimb. However, unlike the fault propagation model presented above, the

crest could have well-developed fracturing if the crestal bedding had passed through a hinge zone.

According to the Homza and Wallace (1995) model, if there is a thick incompetent layer for variable detachment zones, then a fixed hinge fold could form. A fixed hinge model would result in the greatest fracture intensity in and near the hinge zone and less on the limbs. Fracture would be greatest in hinges with large curvature. For the folds in NEBC, greatest fracturing would be in front limb hinge zone.

Although the structural style of the Upper Triassic of NEBC is dominated by folding, the development of the folds is still debatable. There is little Triassic outcrop in the immediate study area to analyze fracturing across a fold from the back limb, through crest, to the front limb. Instead researchers are limited to a small sampling of log data and even smaller sampling of core data. FMI/FMS logs do not image fracturing but, image only open fractures. As a result, a fold model for the folds in NEBC may never be completely understood.

Previous Work

The results of previous studies of fracture orientations, apertures, densities and distributions around folds are summarized below.

In an early field study, Muecke and Charlesworth (1966) measured fracture orientations in folded Cardium sandstones in the foothills of the southern Rocky Mountains. They found four classes of fractures all oriented at high angles to bedding. The first class was oriented parallel to the structural trend and would be classified as Type 2 extension fractures (Stearns, 1968). The next two classes formed a conjugate

pair with an acute bisector perpendicular to strike. The conjugate pair would be classified as a shear set of Type 1 fractures (Stearns, 1968). The fourth class of fractures was oriented perpendicular to structural strike (Stearns' Type 1 extensional). Muecke and Charlesworth (1966) observed that the dihedral angle between the conjugate set decreased in angle from west to east. As a result, they concluded that the fourth class was composed of a set of conjugate fractures, but with a small, indistinguishable dihedral angle.

Burger and Thompson's (1970) paper examined fracture orientations of the Carmicheal Peak Anticline in Montana. They measured fracture and bedding orientations in limestones on both fold limbs and near the crest. Before rotating the data relative to horizontal bedding, fracture orientations from different locations on the fold did not group into distinct sets. However, after rotating the data, the fracture orientations divided into four major sets. They grouped the four fracture orientations into two conjugate shear sets. The one shear set matched Stearns' Type 1 shear fractures with a dihedral angle of 53 degrees and the second set matched Stearns' Type 2 fractures with a 63 degree dihedral angle. No extensional Type 1 or 2 fractures were reported in their paper.

Norris (1971) studied an anticline-syncline pair in the Lower Cretaceous Blairmore Group in the foothills of the southern Rocky Mountains. He observed two sets of fractures with orientations fitting Stearns' Type I and II classification. Both sets had a conjugate pair with dihedral angles of approximately 45 degrees. The fracture orientations, when bedding was rotated to horizontal, were consistent on both the east

and west limbs of the fold. He observed the fracture density to be greatest in areas of maximum bedding rotation and not necessarily in the hinge zones of the fold.

McQuillan (1973) did a regional study of small scale fracturing of limestone in the Asmari Formation in the foothills of the Zagros Mountains in Iran. He found that the fracture density was inversely proportional to the logarithm of bed thickness but was independent of structural position. He concluded that the fracturing predated the folding of the limestones and that the later rock strain, due to folding, took advantage of pre-existing fracture sets.

McQuillan (1974) used aerial photographs to identify fracture patterns on Kuh-e Asmari Anticline in southwest Iran. He observed two simple orthogonal fracture sets parallel and perpendicular to the fold axis. The fracture density depended on structural position. The density was the greatest in the crestal zone and in areas where the fold axis increased plunge. Lower fracture densities were observed on the limbs of the anticline.

Narr (1991) measured fracture density and orientations in the Monterey Formation in California. The Monterey Formation is a thick Miocene sequence of siliceous shale, chert, phosphatic shale, mudstone and dolostone. His data, including measurements from outcrop and well core, showed predominantly a single, Type 1 extension fracture orientation. In outcrop, fracture density was greater in thin beds and was dependent on lithology. Fracture density observed from core showed increases from ductile to more brittle lithologies. In core, the density also depended on structural position and was most intense in the hinge zones and in areas with increasing plunge.

Cooper (1991) interpreted fracture data from FMS log images from two wells in the Canadian Rocky Mountain Foothills. The first well was in the Sukunka-Bullmoose trend

of NEBC. The well penetrated Upper Triassic strata including the Pardonet, Baldonnel and Charlie Lake formations. The well was drilled into the front limb of a fold and entered Triassic strata just off the crest. The bedding dips increased along the well path through the Pardonet Formation and became steeper to nearly vertical through the front limb. Through the Baldonnel Formation the bedding dip decreased as the well path neared the axis of the front limb syncline. The well was drilled into the Upper Charlie Lake Formation and ended at the base of the front limb.

Three fracture orientations were observed on the FMS images in the first well. Cooper (1991) labeled these fracture sets 1, 2 and 3. Cooper's set 1 and set 3 fractures had orientations similar to Stearns' Type 1 and 2 fractures, respectively. However the fractures did not divide into distinct orientations of extensional and shear conjugate sets. Instead, the fractures had orientations spreading over a 60 degree arc, within the bounds of a conjugate set. Cooper's set 3 fractures had a strike orientation in the same direction as set 1 fractures (Type 1) but dipped moderately to the northwest.

Cooper (1991) found a decrease in fracture density in dolomitic siltstone of the lower Pardonet Formation. The fracture density decreased in a position away from the fold hinge zones. As a result, Cooper (1991) concluded that the decrease in intensity could be due to either lithology or structural position.

The fracture interpretation from the FMS image log in the first well was compared to core from the same well. The set 1 fracture density interpreted from the FMS image seemed slightly greater than fracturing observed in core. However, the set 3 fracture density was grossly underestimated by the image log as compared to core. The reason for the underestimation in density was because many of the set 3 core fractures were

mineralized and would show no resistivity contrast on the image log. Although mineralized fractures will not contribute to gas flow rates, they may impede flow through the formation.

The second well Cooper (1991) interpreted was drilled into a ramp anticline structure in the Alberta Foothills. The most dominant set of fractures in the Alberta well were Stearns' Type 2 fractures. The Type 2 fractures had orientations that compare to both conjugate shear and extensional Type 2 fractures. Another fracture set perpendicular to the fold axis (Stearns' Type 1) was also observed in the well.

Jamison (1995, 1997) did an analysis of fracture orientations, length, density and aperture at two outcrop locations on the Monkshood Anticline in NEBC. He defined the outcrop lithology as a, "thin to medium bedded (5 to 75 cm thick) very fine grained, cherty limestone and calcareous and/or dolomitic chert with minor occurrences of crinoidal lime grainstones" (Jamison, 1995, page 74). Jamison's (1995) study was very detailed with 14 stations at one outcrop and 12 stations at the second outcrop. Fracture data were sampled from both limbs of the fold and near the crestal hinge zone.

Most of the fractures in Jamison's (1995) study were oriented at high angles to bedding. The backlimb of the anticline was dominated by fractures oriented parallel or subparallel to the fold axis, (Type 2 fractures). On one of the outcrops the Type 2 fractures were slightly but consistently oblique to the fold axis. Type 1 fracture orientations were also observed on the backlimb but were less common and, in some cases, absent at specific station locations. In the forelimb, the fracture orientations were considerably more variable and included orientations of Type 1 and 2 fracture sets.

Jamison (1997) observed that the fractures parallel and subparallel to the fold axis were often slightly dipping relative to bedding as opposed to being perpendicular to bedding. This dip was systematic and different on both limbs. The fracture orientations, when viewed on the unfolded beds, dip in opposite directions on the two opposing limbs. The fractures on the backlimb dip down in the foreland direction (east) and fractures on the forelimb dip down in the hinterland direction (west). Jamison (1997) concluded that fracture dip was a result of the fractures forming sometime after the folding had initiated.

A surprising observation from Jamison's (1997) study was that the most intensely fractured zones were not associated with bedding curvature or faulting. The two most intensely fractured zones were in the middle of the planar limbs, one on the backlimb and one on the forelimb. However, in general, fracture density was essentially identical on both limbs of the fold. In addition, there were outcrop areas near the anticlinal hinge that displayed very little fracture development.

Jamison (1997) also measured fracture aperture and calculated a mean fracture aperture at each station. Between stations, the mean aperture varied up to two orders of magnitude from 20 μ m to 2 mm. Four stations with the largest mean aperture were: two stations in the mid-backlimb position; the upper forelimb position and; one station in the mid-forelimb, just above a forelimb fault. The large mean aperture stations were not in areas of increased bedding curvature.

Nelson and Serra (1995) discussed the dependence of fracture spacing on both lithology and structural position. Their paper was based on four folded carbonate outcrop studies. They concluded that fracture intensity was dominantly controlled by lithology, especially in non-hinge zones. They predicted that zones in the favorable

fracture lithology (brittle rocks, e.g. dolostone) could have greater fracture intensity than poor fracture lithologies (more ductile rocks, limestone) in the high curvature hinge zone. Also they concluded that brittle rocks will increase fracture intensity less in the hinge zone as compared to more ductile rocks. They gave the following rule of thumb for changes in fracture intensity as a function of carbonate lithology and structural position, "Limestone backlimb fracture intensities could increase four to eight times within the hinge zone, whereas dolomites might increase only two to three times" (Nelson and Serra, 1995).

Cooper et al. (1998) presented a paper that compared flow rates from a vertical well to a side-track horizontal well. The wells were drilled into the Pardonet and Baldonnel formations, in the Boulder Field of NEBC. This field is just north of the thesis study area. The initial vertical well tested gas at 14 mmcf/day and was deemed uneconomic because of low flow rates. The side-track was drilled to encounter more fractures and improve gas flow rates. The well was side-tracked into the lower Baldonnel Formation drilling in a downplunge direction. The well tagged the top of the Charlie Lake Formation and then penetrated the Baldonnel Formation in reverse sequence. The total horizontal deviation was 670 m from the kick-off point. The new well was tested with initial flow rates of >30 mmcf/day and was tied into the gas processing system.

Yose et al. (1998) presented a poster with an FMI fracture study from Norman Wells, NWT. Their study examined a Devonian limestone reef. The reef is naturally fractured but is not fractured by complex folding. They compared the FMI images to oriented core samples. They found that the FMI images accurately measured the orientations of the fractures. However, the images slightly underestimated the number of open fractures,

representing approximately 70% of the fractures seen in core. The unseen fractures had very small apertures. Also, the image log did an excellent job of differentiating between natural fractures and drilling-induced fractures.

Based on the previous studies it is difficult to make generalizations about how fracture orientations, apertures, densities and distributions vary around folds in different lithologies and at different depths, and how these parameters effect reservoir quality. Clearly, what is needed is systematic measurement of all these parameters at each of several sites and the development of a method for quantifying the relationships between these parameters.

Chapter 2

Analysis Method

Introduction

Chapter 2 outlines the data analysis procedure used to predict optimal drilling direction. The data analysis is a three part process. First, the data are interpreted from FMI or FMS image logs. Second, the occurrence weighting is calculated by measuring the angular relationship between the well path and the fractures. The weighting is applied to correct the sampling bias, resulting in a truer measurement of fracture density and orientation distributions. The third part of the analysis is an application of a two step rotation to the fracture planes. The rotation procedure is done to unfold the fold to more easily compare fracture orientations from different folds or dip domains. After the rotations are applied to the fracture planes, occurrence weighted contoured stereonet, rose diagrams, fracture intercept and fracture flow diagrams are constructed. These diagrams are used in Chapters 3 and 4 to compare fracturing within and between wells. The following sections detail the three part data analysis.

Data Interpretation

The data used in the analysis were collected from FMI (Wells 1,2,3,5,7,8 and 9) and FMS (Wells 4 and 6) image interpretations of the nine wells in the study area. The FMI/FMS interpretation is challenging because the upper Triassic is often complexly folded. The best interpretation requires an experienced interpreter who is familiar with the stratigraphic section. For this aspect of the study, Craig Rice (Amoco) interpreted

the FMI/FMS data using Schlumberger software. An iterative approach was used that spanned several years of interpretative work. Rice used his final interpretations in a year long petrophysical analysis completed in 1997.

Three measurements are made from the image logs: bedding orientations, fracture orientations and hydraulic fracture apertures. To differentiate fractures from bedding planes, the interpretation was supported by the use of other logs (e.g. gamma ray) and drilling samples. Every attempt was made to pick every observed fracture on the image logs. Each fracture plane was assumed to completely cross the image log. Although this was not always true, the majority of the fractures did appear to completely cover the image.

The hydraulic aperture for each fracture was calculated using the Schlumberger finite-element model in the program FracView. As discussed in Chapter 1, an important input parameter needed to calculate hydraulic aperture is the drilling mud resistivity. The wide range of aperture values between wells (see Chapter 4) suggested that the mud resistivity may not accurately be calibrated between wells. For this thesis, as suggested by Aguilera (1995), the aperture comparisons will be emphasized primarily within wells rather than between wells.

Fracture Frequency and Spacing

Fracture frequency and spacing are measurements of fracture density in the rock. Fracture frequency is the number of fractures per meter. The reciprocal of fracture frequency is fracture spacing. Fracture spacing gives an average measure of the distance between fractures. For example, if 8 fractures are measured along a 2 meter

scan line, then the fracture frequency is (8 fractures)/(2 meters) or 4 fractures per meter. The fracture spacing is the reciprocal or $2/8$ or 0.25 meters between fractures.

The technique used for measuring frequency and spacing depends on how data are collected. The simplest approach to calculating fracture frequency is along a scan line. The frequency of fracturing along this line is simply the number of fractures per unit length measured on the line (i.e., fracture number/meter). Fracture frequency can also be measured over an area (on a planar surface) instead of along a length. The frequency measurement over an area is the length of fractures per unit area (i.e. meter/meter²). Similarly, if the fracture area could be measured in a volume of rock, then the frequency measurement would be fracture area per unit volume (i.e. meter² /meter³).

When measuring fractures along a scan line, the fracture sampling is biased by the orientation of the scan line (Figure 2-1). Fracture sets with normals to the fracture planes parallel to the scan line are optimally sampled and the resulting frequency measurement is a true representation of the fracture frequency. If the normal to the fracture plane is perpendicular to the scan line (the scan line is parallel to the fracture set orientation) the fractures will not be observed on the scan line. Frequency measurements made from scan lines will underestimate the true frequency as the angle between the fracture normal and scan line increases from zero to ninety degrees.

A simple method to analyze scan line data (Terzaghi, 1965; Hudson and Priest, 1979; and La Pointe and Hudson, 1985) assumes the fractures occur in sets at right angles to the reference plane (e.g. bedding). Three limitations of this method are: the

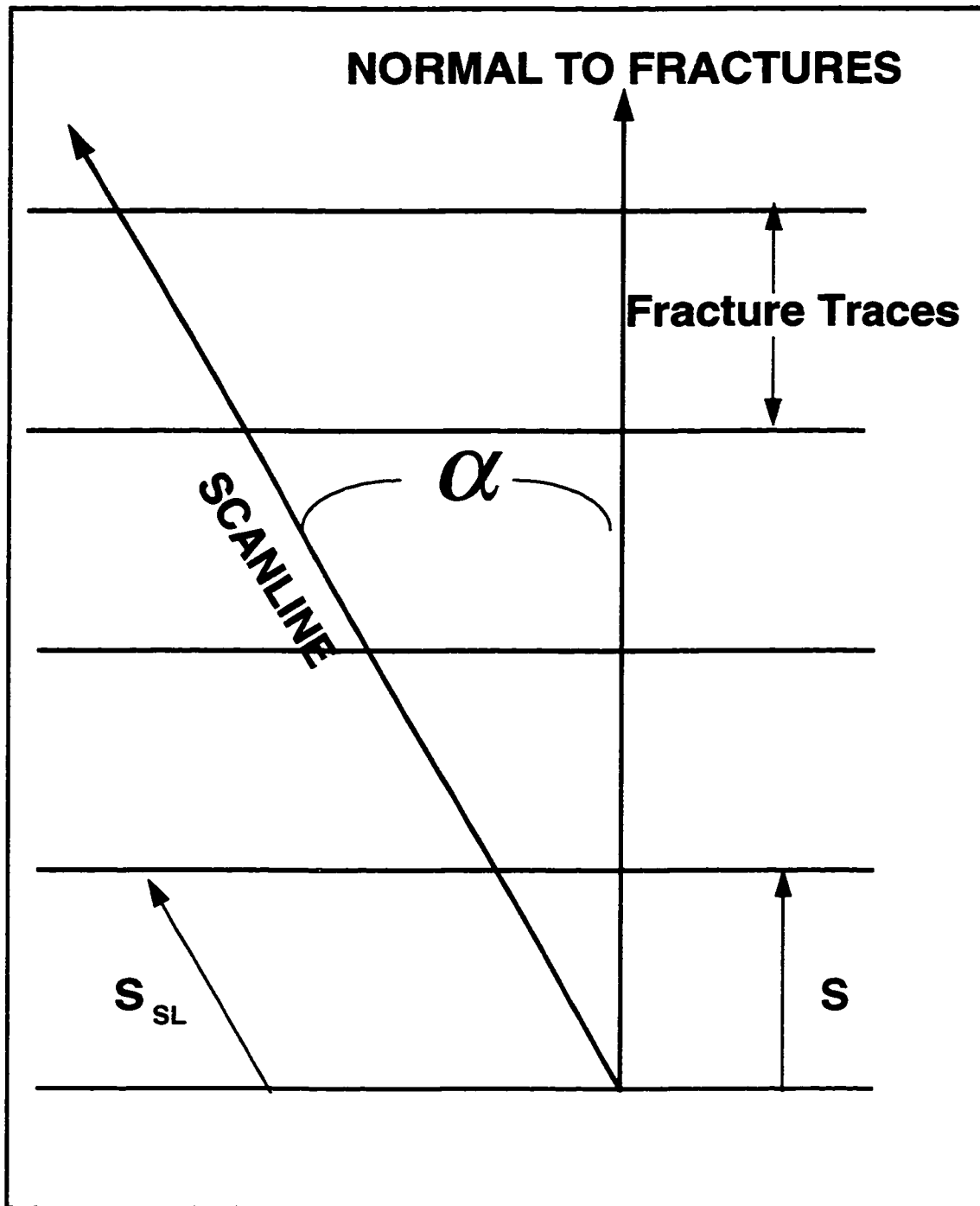


Figure 2-1: Fracture spacing.

The apparent fracture spacing along a line is dependent on the angle between the scan line and the fracture trace.

assumption that fractures occur in sets; the assumption that fractures are perpendicular to the reference plane and; fracture measurements must be made on a reference plane. The above approach is not suited for well data because wells are rarely drilled parallel to a single reference plane and the fractures are not necessarily at right angles to the reference plane.

A more complete analysis assumes fracture sets are oriented in three dimensions (Nolen-Hoeksema and Howard, 1987; Narr, 1996). Although this approach is valid for well data it still assumes that fractures occur in sets. When grouping the fractures into sets, an interpretation must be made as to the average orientation of the set and the range of angles that will be included in each set. Typically, for practical reasons, only several sets are considered and the grouping causes a decrease in resolution of the potential fracture orientations. Additionally, infrequent fractures not falling into an obvious set may be ignored or discarded. However, apparently infrequent fractures on the scan line could be sub-parallel to the line and hence are underestimated due to the sampling bias.

An elegant and general approach (Lacazette, 1991) does not subdivide fractures into sets. Instead, Lacazette's (1991) approach works on any arbitrarily oriented scan line and randomly distributed fractures in three dimensional space. In the following section, Lacazette's (1991) method for calculating fracture frequency will be discussed.

Occurrence Measurements

To help understand Lacazette's method, a single fracture set is considered. Figure 2-1 shows how fracture frequency F is calculated from the apparent fracture frequency F_{SL} measured along a scan line. If α is the angle between the normal to the fracture set

and the scan line, then the minimum fracture spacing S is calculated from the apparent fracture spacing S_{SL} by:

$$S = S_{SL} * \cos \alpha \quad (1)$$

and the maximum frequency of the fractures F is:

$$F = \frac{1}{S} = \frac{1}{S_{SL} \cos \alpha} = \frac{F_{SL}}{\cos \alpha} \quad (2),$$

where F_{SL} is the apparent fracture frequency in the scan line direction.

Equation (2) is true for any scan line oriented at an angle α to the fracture set normal. The possible scan lines, at angle α , lie on a cone in three dimensional space with the normal to the fracture plane at the center of the cone and α as the half apical angle. All scan lines on the cone will give the same apparent fracture frequency and spacing.

A simple example can be used to illustrate the definitions in Equations 1 and 2. Suppose a scan line is at $\alpha = 45^\circ$ to the fracture set normal and the apparent fracture spacing measured on the scan line is 0.28m. The apparent fracture frequency on the scan line is:

$$F_{SL} = \frac{1}{S_{SL}} = 3.6 \text{ fractures per meter.}$$

The minimum fracture spacing, measured in the direction of the normal, is

$S = S_{\alpha} \cos \alpha = 0.2$ meters and the maximum fracture frequency, in the normal direction, is:

$$F = \frac{1}{S} = 5 \text{ fractures per meter.}$$

Lacazette (1991) used an idea that he defines as “occurrence” to eliminate the need to subdivide fractures into sets. Occurrence is defined as:

$$\text{Occurrence} = W = \frac{1}{L \cos \alpha} \quad (3)$$

Where L is the length of the scan line and α is the angle between the scan line and the normal to the fracture. Lacazette (1991) referred to occurrence as “the frequency of a single fracture”.

Fracture frequencies can be calculated by summing the occurrences for each fracture. This is best illustrated by an example. Suppose in the previous example that the length of the scan line L was 2 meters. The occurrence for a single fracture is:

$$W = \frac{1}{L \cos \alpha} = \frac{1}{2 \cos 45} = 0.71 \text{ m}^{-1}$$

The apparent fracture frequency (previously calculated) along the 45 degree scan line is 3.5 fractures per meter. Therefore, over the 2 m length, there are 7 fractures (2 x 3.5). The maximum fracture frequency is then solved by summing up the occurrences for each of the 7 fractures:

$$F = \sum_L W_i = \sum_{i=1}^7 W_i \quad (4)$$

$$= 0.71 + 0.71 + \dots + 0.71$$

$$= 7 (0.71) = 5 \text{ fractures per meter.}$$

Occurrence can be considered as a weighting for each fracture. If the scan line is nearly normal to the fractures ($\cos \alpha \sim 1$), the weighting is low. If the scan line is nearly perpendicular to the fracture normal line ($\cos \alpha \ll 1$), then the weighting is large. The weighting can be applied to both rose diagrams and stereoplots to correct the sampling bias due to the orientation of the scan line.

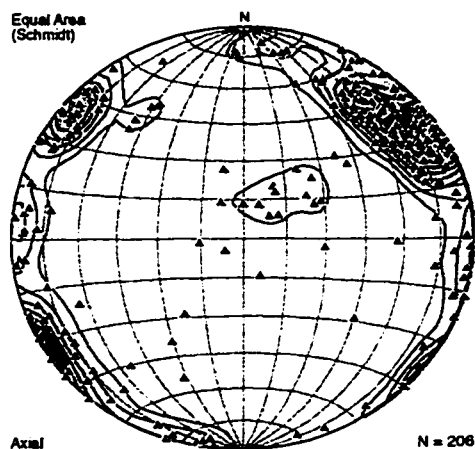
Figure 2-2 (from Well 1 of the study area) shows the effects of applying the occurrence weighting to the contouring on a stereonet and to the fracture distribution on a rose diagram. The well was drilled in a northeasterly direction. Fracture planes oriented sub-parallel to the drilling direction, (e.g. the set striking at 40 east of north), have a larger occurrence weighting. Fracture planes that are more perpendicular to the drilling direction (the set striking at 30 west of north) will have a smaller weighting. The weighted rose diagram and stereonet gives a better representation of the true fracture distributions.

Equation 4 is modified to solve for fracture frequency in a new direction PL. (PL, the predictive line, is at an angle β to the normal of the fracture set, Figure 2-3a). From Equations 2 and 4 the frequency of fractures in the direction PL is:

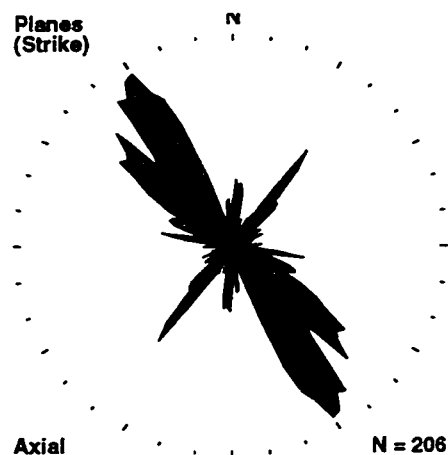
$$F_{PL} = F \cos \beta \quad (5) \text{ or,}$$

$$F_{PL} = \sum_i W_i \cos \beta \quad (6)$$

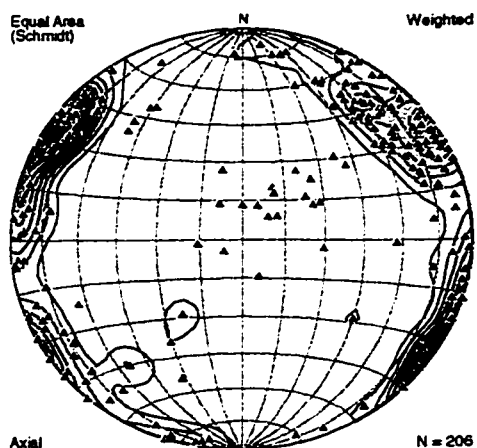
Equation 6 is modified to solve the general problem of fractures oriented in any direction. Figure 2-3b shows a more random distribution of fracture orientations. The fracture orientations, scan line (SL) and predictive line (PL), can be oriented in any arbitrary direction. For the i^{th} fracture, the occurrence is given by (Figure 2-3c):



a) raw fracture poles



b) raw fracture planes



c) occurrence weighted contouring



d) occurrence weighted planes

Figure 2-2: Fracture occurrence applied to stereonet contouring and rose diagram fracture frequency.

Figures 2-2 a & b show the stereonet contouring and rose frequency diagrams for the raw fracture data from Well 1. Figures 2-2 c & d show the stereonet contouring and rose frequency diagrams for the occurrence weighted fracture data from Well 1.

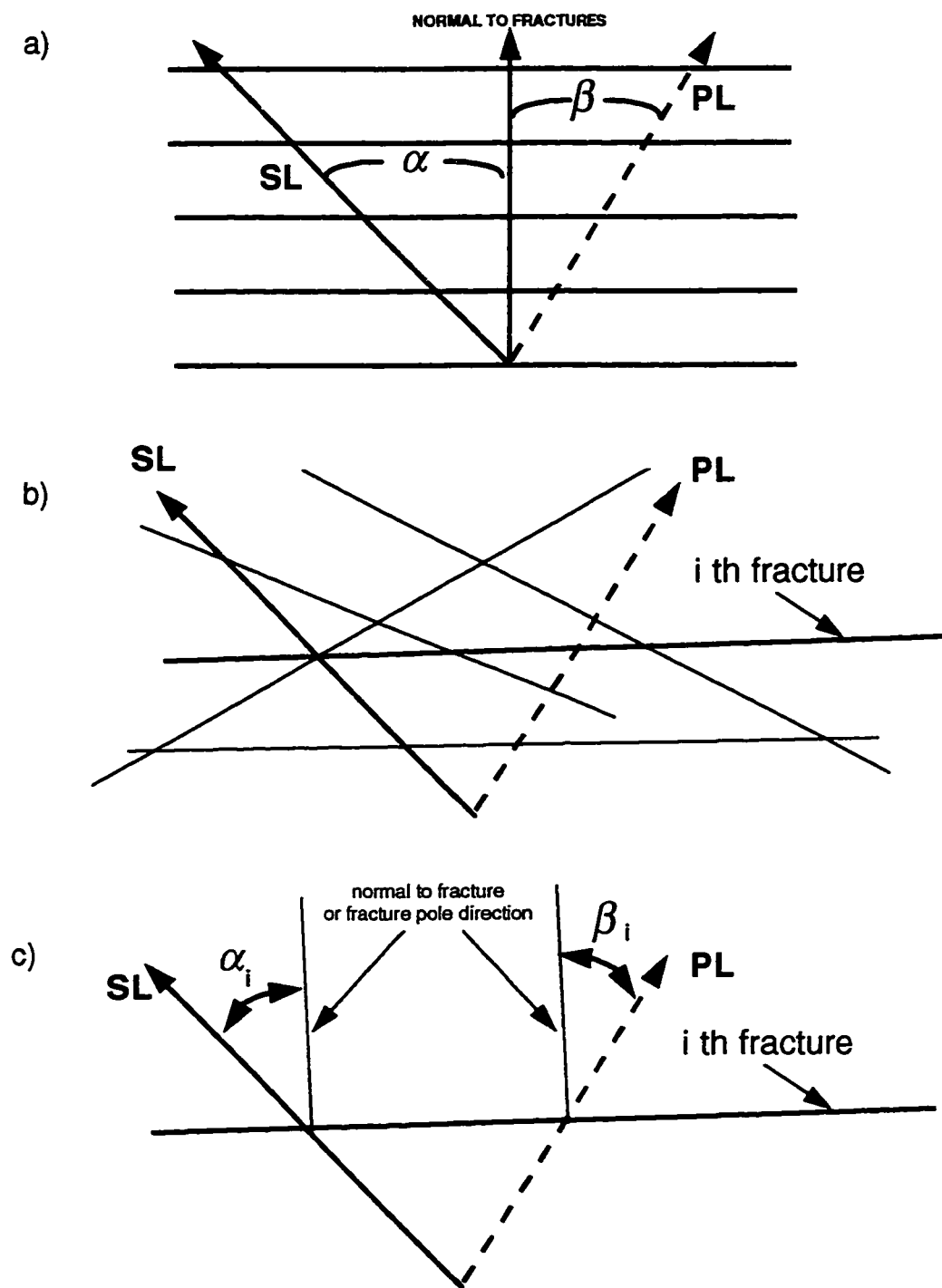


Figure 2-3: Predicted fracture spacing along an arbitrary line.

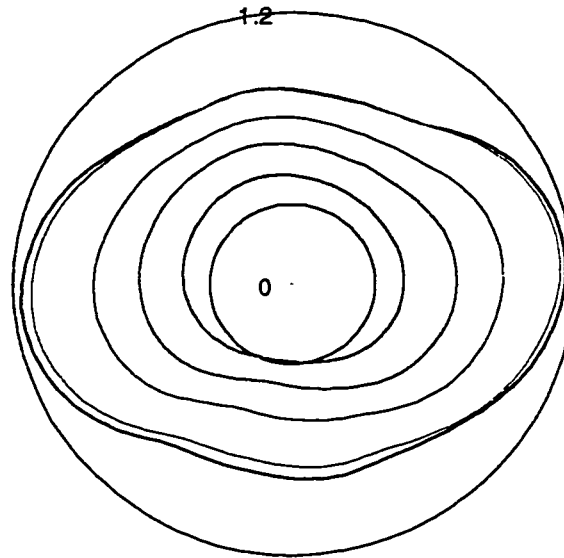
$$W_i = \frac{1}{L \cos \alpha_i} \quad (7)$$

and the frequency for fractures in the new direction is given by:

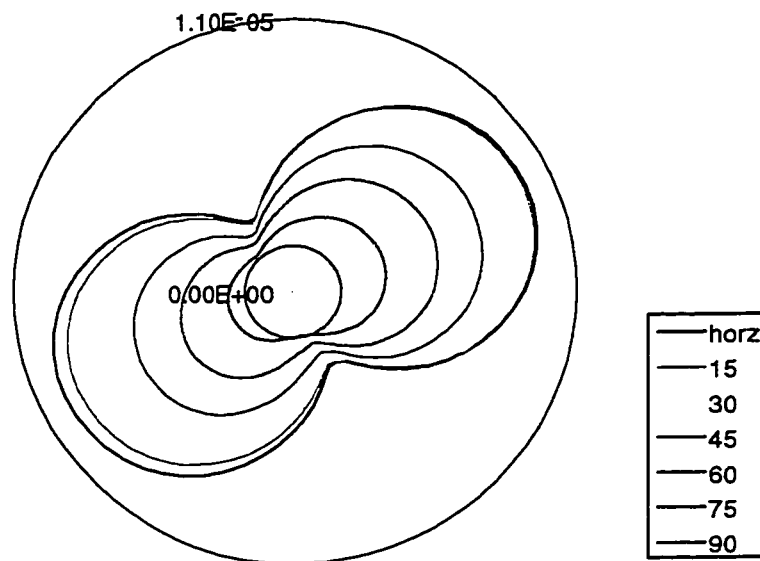
$$F_{PL} = \sum_i W_i \cos \beta_i \quad (8).$$

Equation 8 is extremely useful for well FMI or FMS data. The equation allows for a method where fracture data from a well are used to calculate the fracture frequency expected in other drilling directions. For each fracture encountered in the well, an occurrence weighting is calculated. Then by multiplying each occurrence by $\cos \beta_i$, (where β_i is the angle between the new direction and the pole of the i^{th} fracture or the direction of the fracture normal), and summing these values, a new fracture frequency is calculated. By repeating this process in multiple directions, a fracture intercept rate diagram is created, like in Nolen-Hoeksema and Howard (1987), however this is a more general solution.

Figure 2-4a shows a fracture intercept rate diagram calculated from the fracture data from Well 1. The polar diagram is a three dimensional representation of the expected number of fractures intercepted per meter drilled (fracture density). The seven oval curves represent different drilling inclinations in steps of 15 degrees from horizontal to vertical. The maximum number of fractures per meter drilled (approximately 1.2), is predicted by drilling horizontally in an east or west direction. The minimum number of fractures intercepted per meter, (approximately 0.82), for a horizontal well, would be in either a north or south direction. As the well inclination angle increases towards vertical the fracture intercept rate or density decreases.



a) fracture intercept diagram



b) fracture flow diagram

Figure 2-4: Fracture intercept diagram (fracture density) and fracture flow diagram (fracture volume).

Figure 2-4 shows the intercept diagram for Well 1. The circular to oval curves in these polar plots represent different drilling inclinations from horizontal to vertical. Distances from the center of the circle give the fracture density values (a) and fracture volumes per meter. The outside circle is the density (a) or volume (b) measurement at that distance.

Each term in the sum of Equation 8 is multiplied by the hydraulic aperture cubed (measured from the image log) for each fracture giving a fracture volume measurement. The sum of these terms gives the fracture flow intercept rate (again like Nolen-Hoeksema and Howard, 1987, however this is a more general solution) in the predicted line direction (PL) as shown in Equation 9:

$$Flow_{PL} = \sum_i W_i (\cos \beta_i) e_i^3 \quad (9),$$

A flow intercept rate diagram is made in a similar way to the fracture intercept diagram. However by weighting each term with the fracture aperture cubed, a measure of relative fracture volume per meter (fracture volume density) in various drilling directions is made. The optimal drilling direction (Nolen-Hoeksema and Howard, 1987), would be in the direction of the maximum flow intercept or fracture volume density.

Figure 2-4b shows the flow intercept rate diagram from the fractures interpreted in Well 1. The calculated optimum drilling direction is either to the northeast or southwest. The direction is skewed from east-west (maximum intercept rate) because the fracture planes striking NNW/SSE (nearly perpendicular to the optimum drilling direction) have the largest apertures. This effect is common in the study area and will be discussed in detail in Chapter 4. The optimal drilling inclination would be horizontal and drilling optimization decreases as inclination increases towards vertical.

Figure 2-4, demonstrating the effects of applying the occurrence correction, is not calculated from the raw fracture planes. Instead the fractures are rotated, relative to horizontal bedding, before the diagrams are constructed. Although occurrence can be

calculated on rotated beds it is more accurate and easier to apply the correction before the fracture rotations. The next section details the fracture rotation procedure.

Fracture Rotation

Most fractures in this nine well study occur at high angles to bedding. In addition, due to folding, there is a wide variation in dip domains within and between wells. As a result, the collected raw fracture orientations appear to be random and unsystematic. One approach to better analyze the fracture orientations is to divide the data into domains of constant bedding dip and present the data for each dip domain separately. This is the approach used by Cooper (1991). Although Cooper's (1991) method is appropriate for smaller data sets, it is better with large data sets to compare fractures to the same relative reference frame, i.e. bedding. This is accomplished by rotating data in each dip domain until bedding is horizontal. The rotation method is outlined below.

The fractures are rotated in a two step process. First, for each well, the trend and plunge of the fold axis is determined from the bedding poles within the Triassic strata. This is done by assuming the fold is cylindrical and doing a statistical eigenvector analysis. The first rotation removes the plunge of the fold by rotating the fold axis to horizontal in the trend direction. Both the bedding and fracture planes are rotated by the same amount in the first step. This rotation is small in eight of the nine wells with gentle plunge angles below 6 degrees. The plunge in Well 3 is unusually large at 13 degrees (see Well 3, Chapter 3 for reasons why).

Next, bedding orientations are divided into dip domains before applying the second rotation. The dip domains are grouped within each well in increments of 10 degrees after the fold plunge is rotated out. For each 10 degree increment, a contour analysis of

poles to bedding is done to calculate a maximum contour point for each dip domain. A second rotation is applied rotating the maximum contour value to vertical such that the bedding dip domain becomes horizontal. Each bedding dip domain and the fractures within that dip domain are rotated about the horizontal fold axis until all the bedding dip domains are horizontal. The orientations of the fractures relative to horizontal bedding can then be read off the stereonet.

Stereonet rotations are not linear functions. Therefore, rotating out fold plunge followed by rotation of dip domains to horizontal does not necessarily give the same answer if the order is reversed. The process used in this thesis assumes that the plunge developed near the end of folding. This assumption is not critical when the folds have small plunge angles, like the plunges of the folds dealt with here. However, in areas of steep plunge, the rotation order is important, and, in particular, the model of how the plunge was induced is critical.

Summary

The fracture analysis method in this thesis is unique. Lacazette (1991) developed his technique to design a computer algorithm to better grid fracture data for contouring on a stereonet. However, in this thesis, occurrence is used in the construction of weighted stereonets, rose diagrams, and intercept diagrams. Additionally, this analysis constructs these diagnostic diagrams using fractures rotated by an unfolding process.

The diagnostic diagrams outlined above are used in the next chapter to build a model for optimum drilling direction. It is important to note that the fractures are rotated before the intercept and flow diagrams are constructed. Therefore, optimum drilling direction is defined relative to bedding, not to absolute orientations in space.

Chapter 3

Structure and Fracture Analysis of Well Data

Introduction

Data for each well are shown in this chapter. The data are displayed using equal area stereonet, rose diagrams, fracture intercept diagrams and flow intercept diagrams. The stereonet is contoured using a Gaussian counting model with $K=100$ using Spheristat (version 2.1, Pangaea Scientific) software. The stereonet is contoured either using the raw data or occurrence weighted data. The rose diagrams show a smoothed relative frequency with a class interval of 5 degrees (program Spheristat). The rose diagrams are displayed for both the raw data and the occurrence weighted data.

The flow and intercept diagrams are calculated and displayed for the whole interval and for three divided intervals. The divided intervals are grouped based on gross lithologic packages. The upper interval includes the P4 and P3 units of the Pardonet Formation. This interval is primarily tight non-reservoir limestone and dolomite. The middle interval includes the P2, P1, B4, and B3 units of the Pardonet and Baldonnel formations. The middle unit is a mixed facies of silts, sandstones, limestones and dolomite. The lower unit includes the B2 and B1 units of the Baldonnel Formation. The lower unit is primarily limestone and dolomite, with rocks of greater porosity and reservoir quality. The upper, middle and lower units are divided out to examine fracture variations in the stratigraphic section. The tops for the intervals were interpreted from electric logs by Craig Rice.

Five common figure types are used for each well. The five figures are described below.

1. The first figure has two stereoplots. The first plot shows the raw bedding and fracture data before bedding rotation. The second plot shows the bedding and fracture data after bedding rotation.
2. The second figure is used to describe how the well was drilled. The second figure is made up of three parts showing: the well path in a vertical dip direction projection; the well in a vertical strike projection and; a stereoplot of the well survey points through the upper Triassic before and after bedding rotation. Projected bedding dips are displayed on the well sections.
3. The third figure is divided into six sub-figures. The first two figures (a&b) represent the fractures as poles on a stereonet and with their strikes plotted on a rose diagram. The second two figures (c&d) are the occurrence weighted stereonet and rose diagrams. The last two figures (e&f) show the intercept and flow diagrams for the entire interval. Six different well inclinations are displayed on the diagrams, from horizontal (0 degrees inclination) to vertical (90 degrees inclination) in 15 degree increments.
4. The fourth figure displays some key aperture relationships for each well. This figure is divided into four sub-figures. Figure (a) shows the aperture variation with depth on a log-normal graph. The depth is the measured drilling depth in the well. Figure (b) shows the variation of aperture versus the azimuth of the fracture orientation on a log-normal graph. The fracture azimuth is measured as the fracture's dip direction. The dip direction is 180 degrees from the fracture pole azimuth. Figures (c & d)

show the poles on a stereonet (c) and the strikes on a rose diagram (d) of the 10 % largest aperture fractures in the well.

5. The fifth figure shows the flow and intercept diagrams for three intervals in the well. The fifth figure is divided into six sub-figures. The figures on the left side of the diagram (a-1, b-1 and c-1) are intercept diagrams. The figures on the right hand side (a-2, b-2 and c-2) are flow diagrams. The two top figures (a-1 and a-2) are calculated from fractures in the upper unit (P4 through P3). The two middle figures (b-1 and b-2) are calculated from fractures in the middle unit (P2 through B3). The bottom two figures are calculated from fractures in the lower unit (B2 through B1).

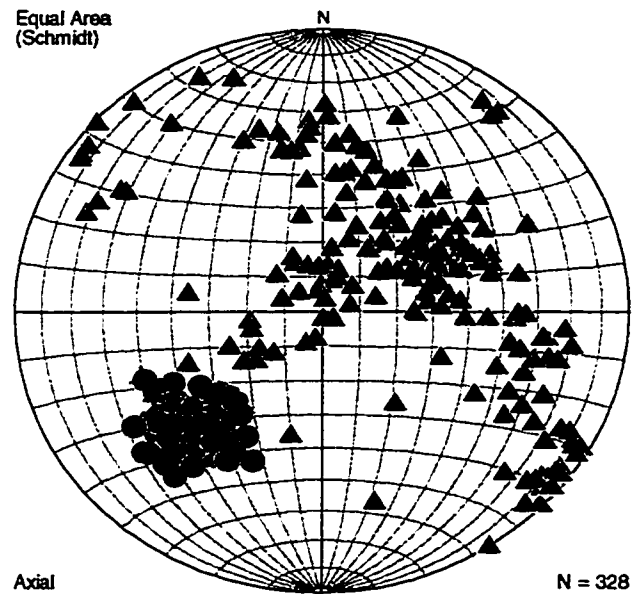
Well 1

Well 1 was drilled off the structural crest in a forelimb position. The well intercepted beds dipping at 40 to 50 degrees down to the northeast. The structural analysis using only the upper Triassic bedding poles gives an eigenvector fold axis with a plunge of 23 degrees toward an azimuth of 337 (23/337). This high angle of plunge is not believed to represent the true structural plunge and does not match the seismic maps in the area (Figure 1-4). The unreliable value is due to the limited sampling of dip domains on the limb of a fold. To calculate a more reliable fold axis orientation, bedding planes interpreted from the Fernie Group were included in the analysis (Joubert and Spratt, 1995). Including these beds led to a more believable fold axis of 05/135.

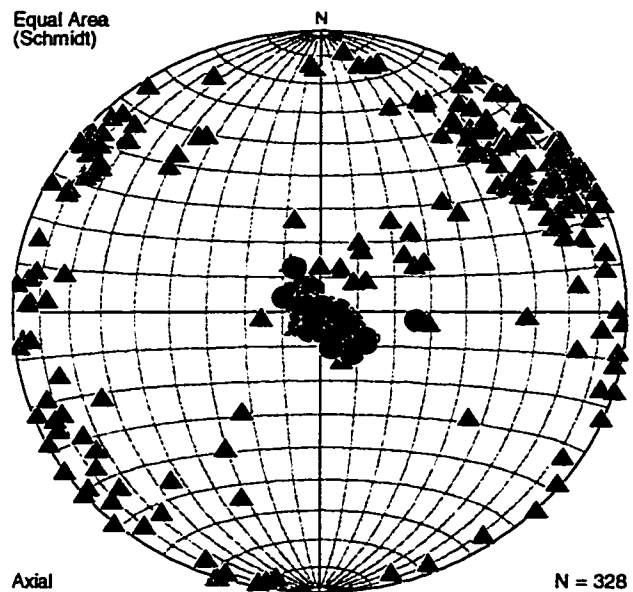
The fractures are rotated using the 05/135 fold axis as outlined in Chapter 2 by first removing the fold plunge followed by a rotation of the bedding dip domains to horizontal. The results of the rotations to the bedding and fracture poles are shown in Figure 3-1.

The well path in dip and strike views are shown in Figure 3-2. The well was drilled into the structure at an inclination of approximately 60 degrees. Relative to bedding, the well entered at a low angle of 30 degrees and increased angle through the upper Triassic section, exiting at approximately 60 degrees.

The rotated fracture poles and planes are shown in Figures 3-3, a & b. Most of the fractures are at high angles relative to bedding and fall into distinct sets. The most common set measured in the well bore has a strike orientation between 140 and 160 degrees, closely matching the orientation of Stearns' Type 2 fractures. There is another set striking at 040 degrees that classifies as a Type 1 fracture set. There are two other



a) bedding (circles) and fractures (triangles) before rotation



b) bedding (circles) and fractures (triangles) after rotation

Figure 3-1: Well 1 bedding and fracture data.

Stereonet projection of fracture and bedding poles before and after rotation.

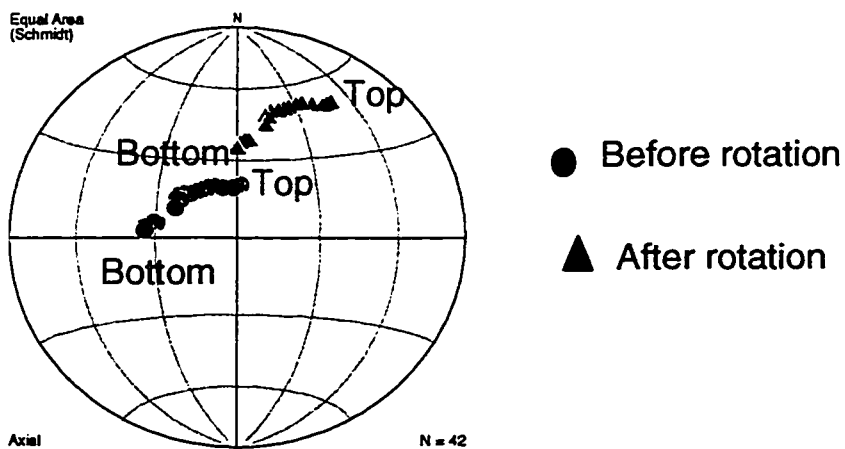
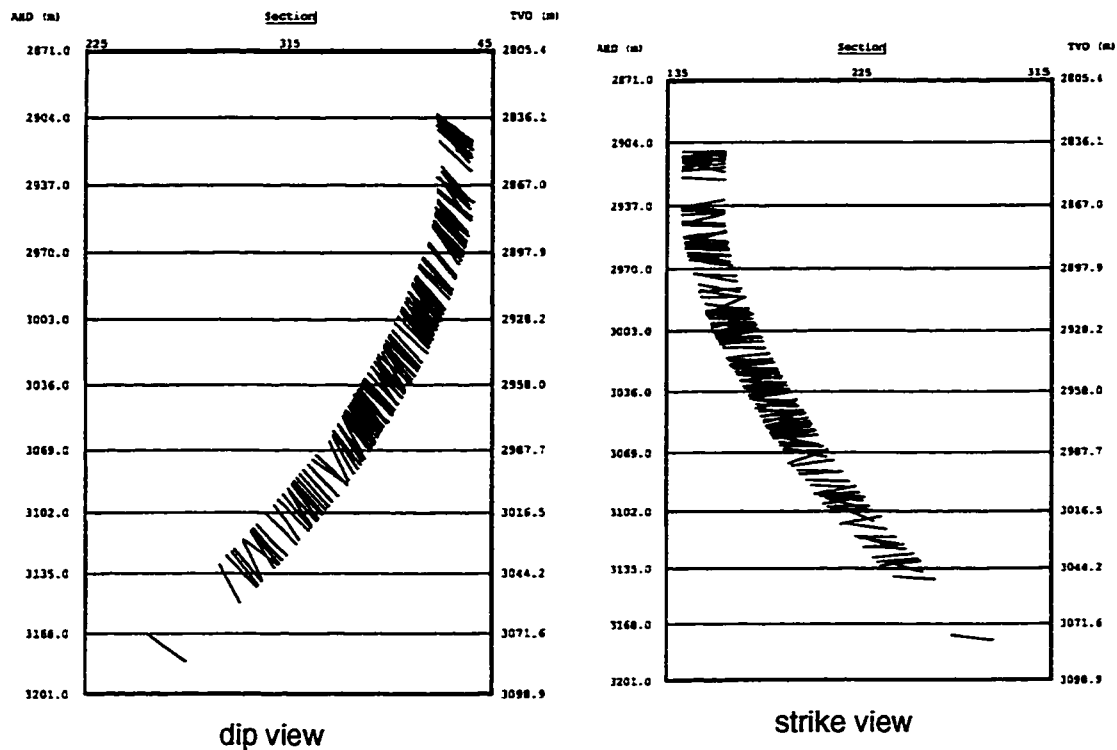
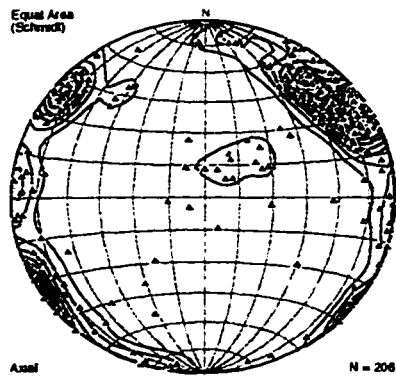
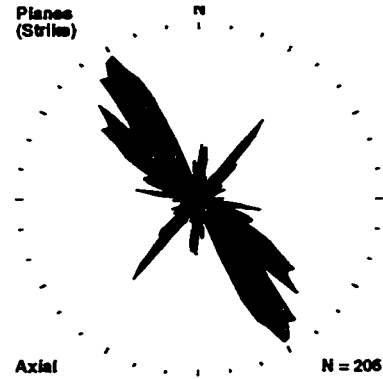


Figure 3-2: Well 1 well path.

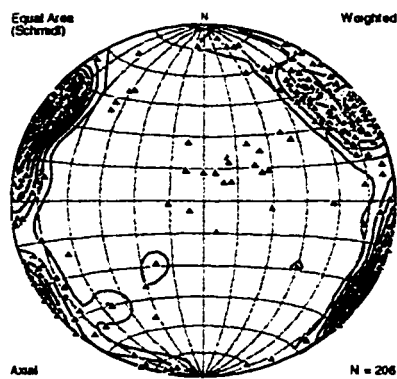
Well path is shown in dip and strike sections and in a stereonet projection of the well path before and after bedding rotation.



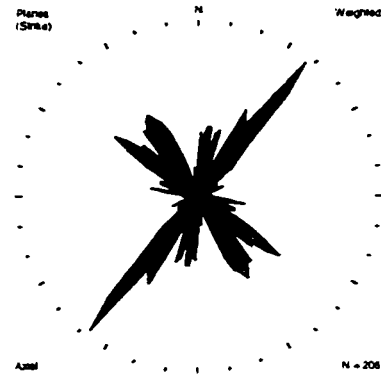
a) raw fracture poles



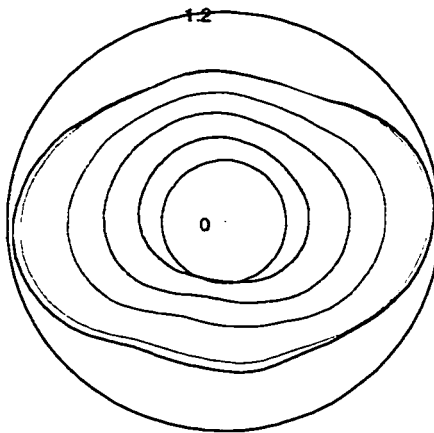
b) raw fracture planes



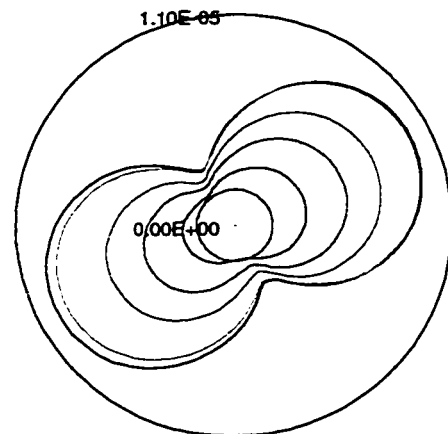
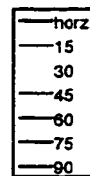
c) occurrence weighted contouring



d) occurrence weighted planes



e) fracture intercept diagram



f) fracture flow diagram

Figure 3-3: Well 1 occurrence correction, flow and intercept diagrams.

Rotated fracture poles and strikes before and after occurrence correction are shown in figures a through d. Fracture intercept and flow rate diagrams for upper Triassic interval are shown in figures e and f.

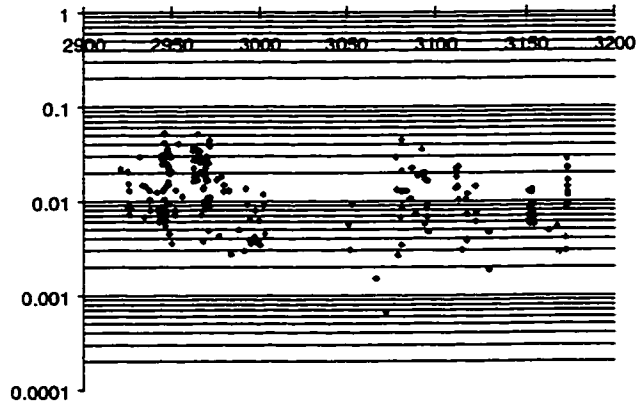
fracture sets, one at approximately 005 degrees and a second set at approximately 110 degrees.

Occurrence weighting (Figures 3-3 c & d) suppresses the abundance of Type 2 fractures and increases the apparent abundance of the other fractures, especially the Type 1 fractures. The Type 1 fractures are the most abundant set after the occurrence weighting is applied.

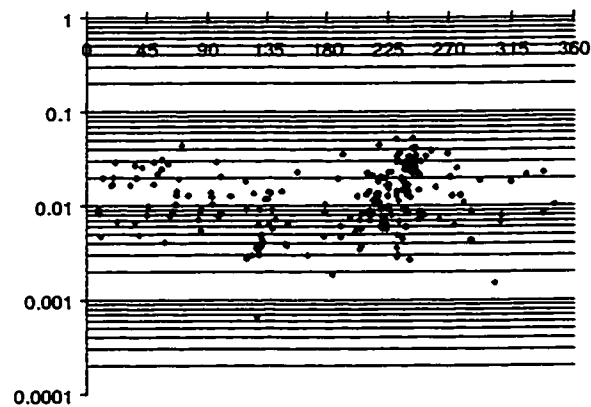
The fracture intercept and flow diagrams for the entire interval are shown in Figures 3-3 e & f. The fracture intercept diagram shows the maximum fracture sampling is predicted for drilling in an east or west direction, with a slightly higher intercept rate in the easterly direction than in the westerly direction. The fracture intercept rate increases as the sample direction changes inclination from vertical (90 degrees) to horizontal (0 degrees), relative to bedding.

The flow intercept diagram has maxima in the northeast and southwest directions, with the northeast direction being slightly better for drilling. The difference in direction of the maxima for the flow and intercept directions is due to the effect of the large fractures. Many of the Type 2 fractures (Figure 3-4) have large aperture fractures and direct the optimal flow intercept rate towards the northeast.

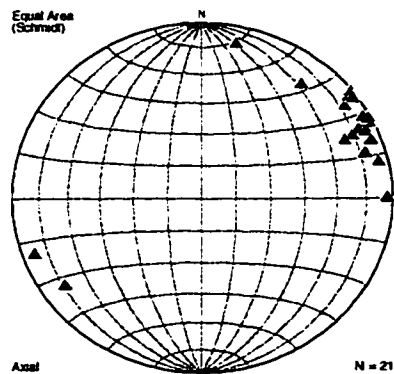
There are significant changes in fracture orientation, intercept rate and flow rate for different stratigraphic levels in the well (Figure 3-5). The maximum intercept rate orientation is: ENE/WSW in units P4 to P2; SE/NW in units P2 to B2 and; N/S in the B2 to CLLK units. The maximum intercept flow rates also have similar orientations to the intercept rate diagrams. The P4 to P2 interval is the most fractured with a maximum intercept rate of nearly 3 fractures per meter compared to 1 and 1.2 for the lower two



a) fracture aperture versus depth (m) in well.



b) fracture aperture versus dip direction azimuth.



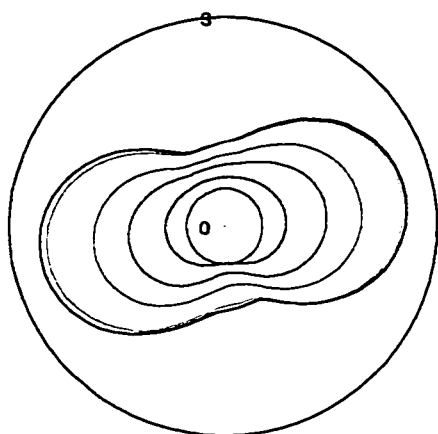
c) large aperture fracture poles



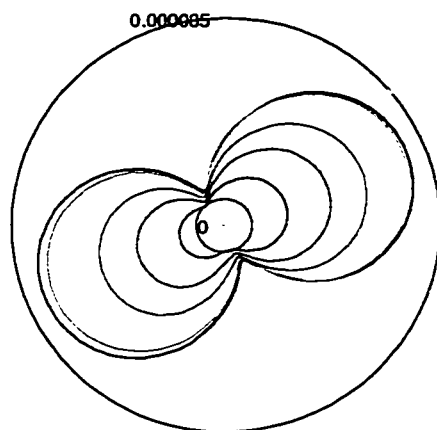
d) large aperture fracture strikes weighted rose diagram

Figure 3-4: Well 1 fracture aperture relationships.

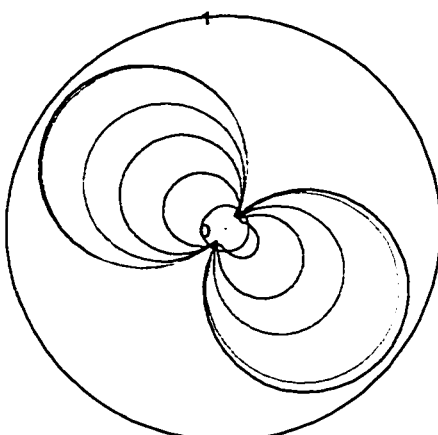
Fracture aperture relationships as a function of depth and azimuth (a and b). The 10% of fractures with the largest apertures are shown on stereonet and rose diagram (c and d).



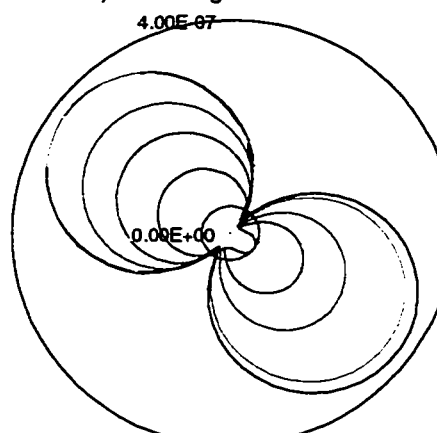
a-1) intercept diagram P4 to P2



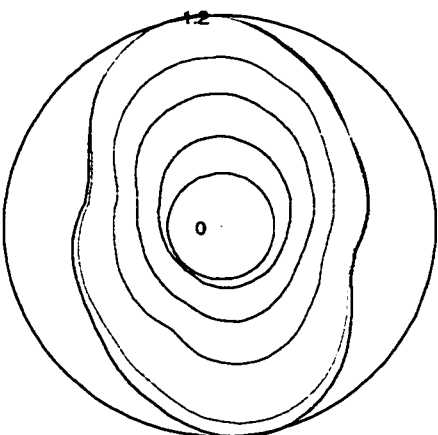
a-2) flow diagram P4 to P2



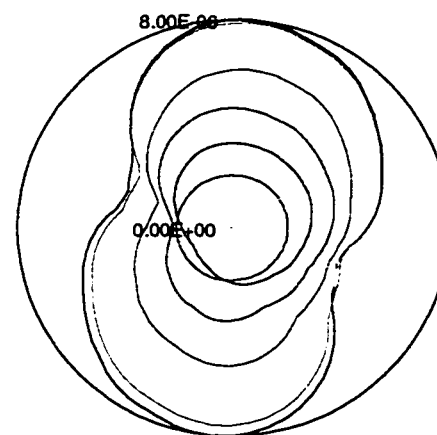
b-1) intercept diagram P2 to B2



b-2) flow diagram P2 to B2



c-1) intercept diagram B2 to CLLK



c-2) flow diagram B2 to CLLK

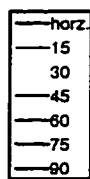


Figure 3-5: Well 1 flow and intercept diagrams by divided units.

The Pardonet and Baldonnell are divided into 3 intervals: a-1 and a-2 show the intercept and flow diagrams for units P4 to P2; b-1 and b-2 show the intercept and flow diagrams for units P2 to B2 and; c-1 and c-2 show the intercept and flow diagrams for the B2 to Charlie Lake Formation units.

stratigraphic intervals. The maximum flow rate changes dramatically between intervals.

The upper unit has the greatest volume of open fractures per meter, two orders of magnitude larger than the middle unit and four times greater than the lower unit.

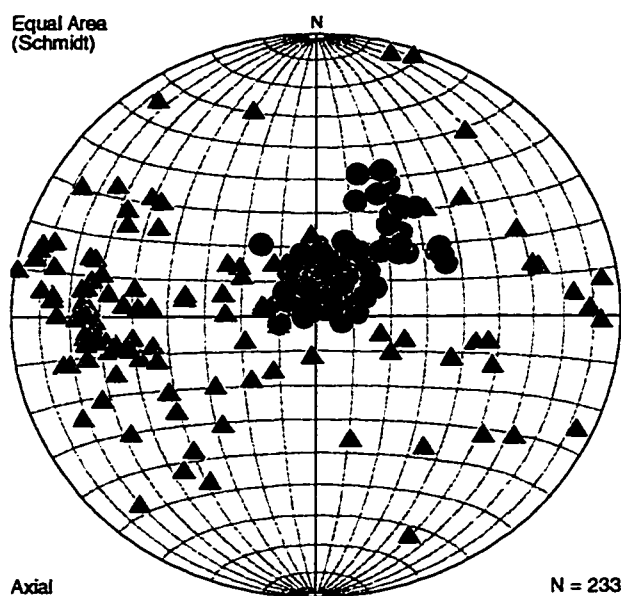
Well 2

Well 2 was drilled on a gently dipping backlimb. The bedding dips are approximately 10 degrees in the upper units. Deeper in the interval, the well crosses a hinge and the dips increase up to 46 degrees. The structural analysis using the upper Triassic bedding poles gave an eigenvector fold axis with a plunge of 06 degrees toward an azimuth of 135 (06/135). The fractures were rotated using this fold axis as outlined in Chapter 2 by first removing the fold plunge followed by a rotation of the dip domains. The resulting rotations are shown in Figure 3-6.

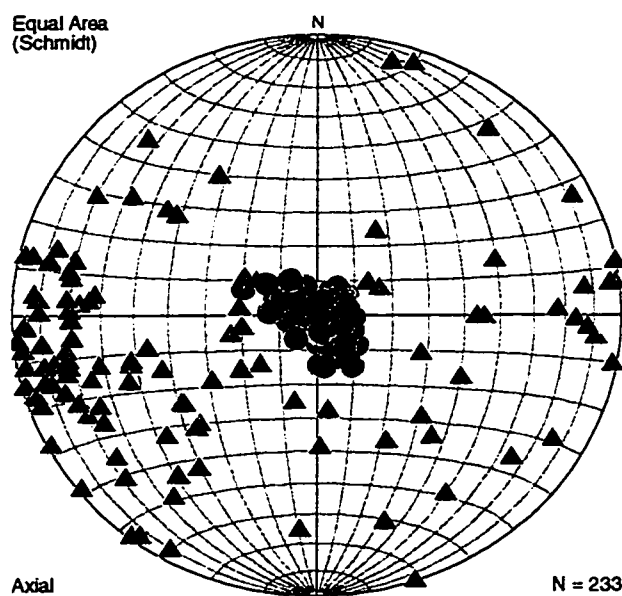
The well path in dip and strike views is shown in Figure 3-7. The well was drilled nearly vertically into the structure. Relative to bedding, the well entered at a high angle, nearly 90 degrees, and decreased angle across the fold hinge to approximately 60 degrees.

The rotated fracture poles and planes are shown in Figures 3-8, a & b. Most of the fractures are at high angles relative to bedding. The most common fracture set measured in the well bore has poles at high angles on the west side, having strike planes oriented between 160 and 190 degrees. This set is divided into three peaks with the maximum peak oriented at approximately 168 degrees. There are two other sets oriented at 035 degrees, classifying as Type 1 fractures and at 135 degrees, classifying as Type 2 fractures.

The occurrence weighted contoured stereonet and rose diagram (Figures 3-8 c & d) changes the relative size of the three peaks associated with the most abundant set. The maximum peak is now oriented at approximately 012 degrees (192 degrees). The occurrence weighting also decreases the relative abundance of Type 2 and 3 fractures.



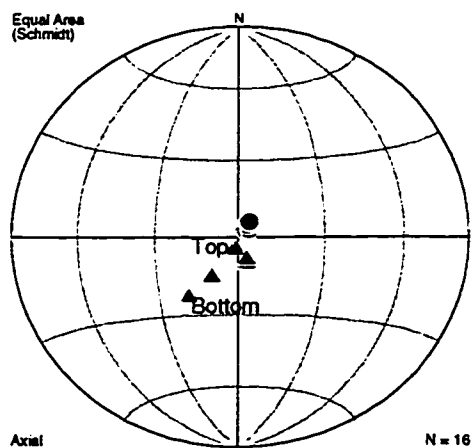
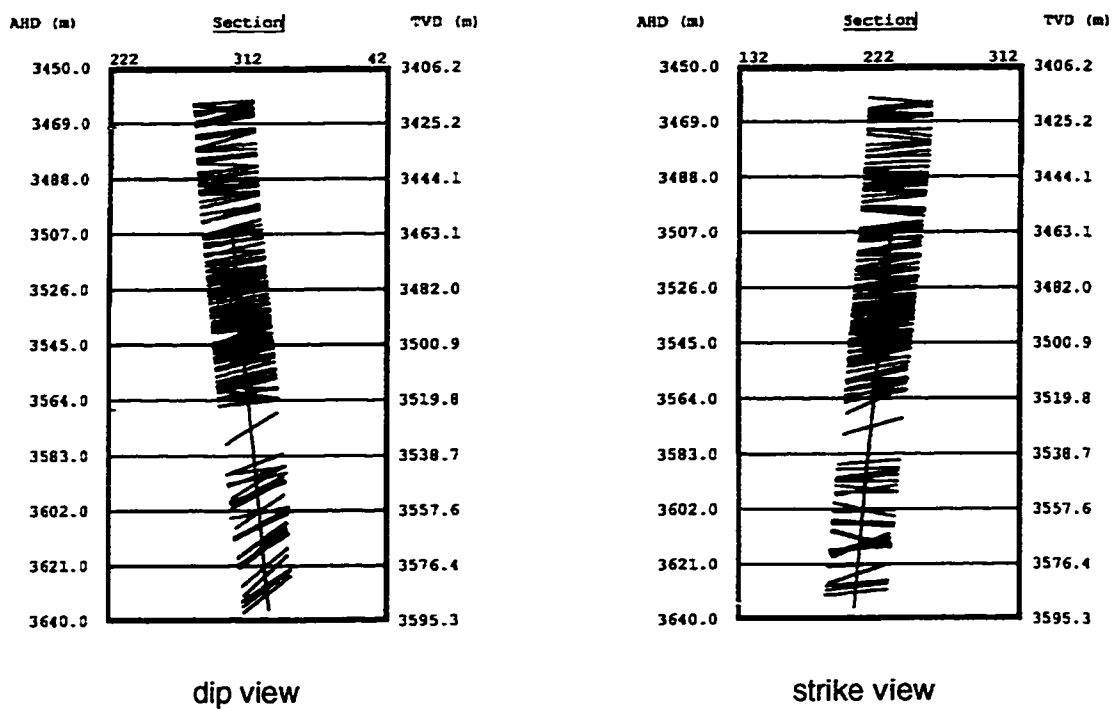
a) bedding (circles) and fractures (triangles) before rotation



b) bedding (circles) and fractures (triangles) after rotation

Figure 3-6: Well 2 bedding and fracture data.

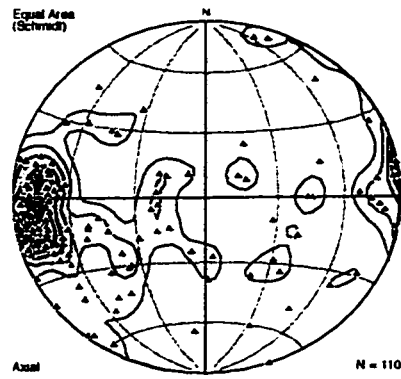
Stereonet projection of fracture and bedding poles before and after rotation.



- Before rotation
- ▲ After rotation

Figure 3-7: Well 2 well path.

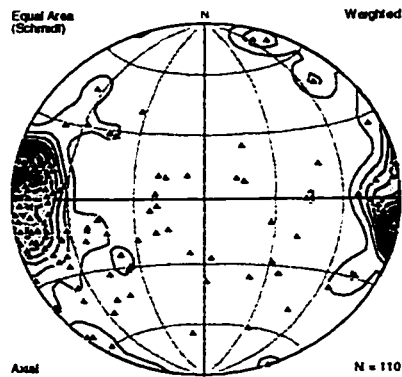
Well path is shown in dip and strike sections and in a stereonet projection of the well path before and after bedding rotation.



a) raw fracture poles



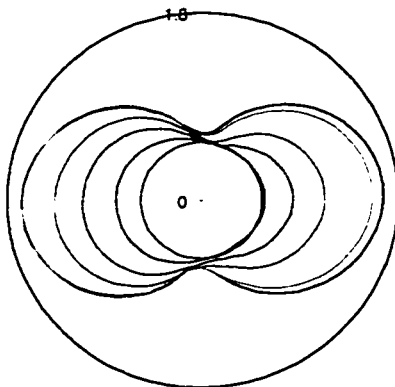
b) raw fracture planes



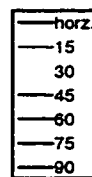
c) occurrence weighted contouring



d) occurrence weighted planes



e) fracture intercept diagram



f) fracture flow diagram

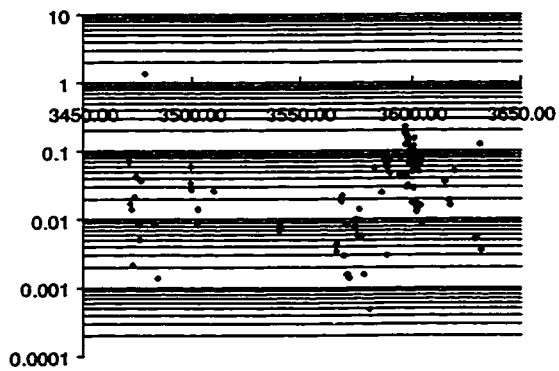
Figure 3-8: Well 2 occurrence correction, flow and intercept diagrams.

Rotated fracture poles and strikes before and after occurrence correction are shown in figures a through d. Fracture intercept and flow rate diagrams for upper Triassic interval are shown in figures e and f.

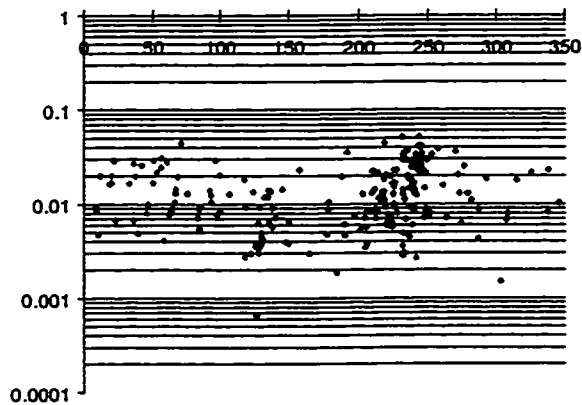
The fracture intercept and flow diagrams for the entire interval are shown in Figures 3-8 e&f. The fracture intercept diagram shows the maximum fracture sampling is predicted in an east or west direction, with a slightly higher intercept rate in the west direction. The fracture intercept rate increases as the sample direction changes inclination from vertical (90 degrees) to horizontal (0 degrees), relative to bedding.

The flow intercept diagram maxima are in the ESE and WNW directions, with the WNW direction being better particularly at the higher drilling angles. The difference in direction of the maxima for the flow and intercept directions is due to the larger fracture orientations and the occurrence weighting. The larger fractures are shown in Figure 3-9, c&d.

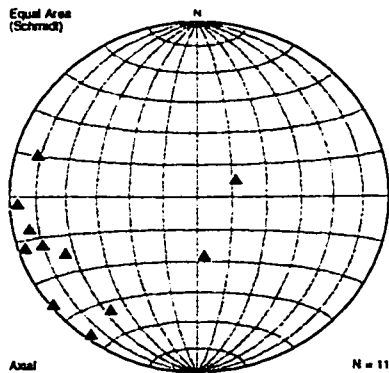
There are minor changes in fracture orientation with position in the well (Figure 3-10). The maximum flow and intercept rate rotates slightly from ESE in the upper unit to ENE in the lower unit. The B2 to lower B1 interval is the most fractured with a maximum intercept rate of nearly 15 fractures per meter compared to 3 for the upper unit and 0.4 for the middle unit. The maximum flow rate changes dramatically between intervals. The upper unit has the greatest volume of open fractures per meter even though this unit is less densely fractured. The fracture volume for the upper unit is largely influenced by one very large fracture aperture at a measured depth of approximately 3470 meters. The resulting volume is approximately 30 times greater than in the lower unit and many orders of magnitude greater than the middle unit.



a) fracture aperture versus measured drilling depth (m)



b) fracture aperture versus fracture dip direction azimuth



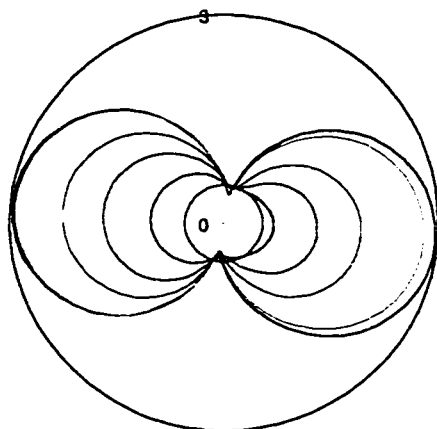
c) large aperture fracture poles on stereonet



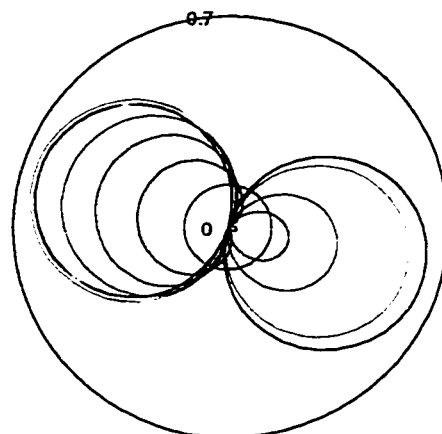
d) large aperture fracture strike direction on weighted rose diagram

Figure 3-9: Well 2 fracture aperture relationships.

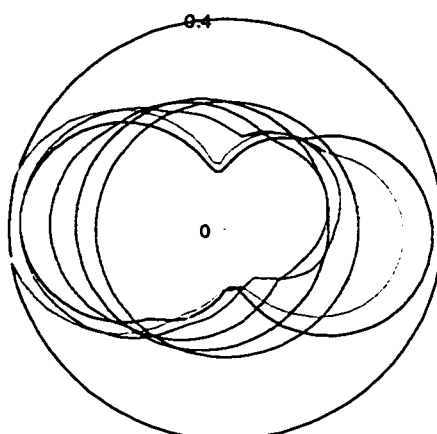
Fracture aperture relationships as a function of depth and azimuth (a and b). The 10% of fractures with the largest apertures are shown on stereonet and rose diagram (c and d).



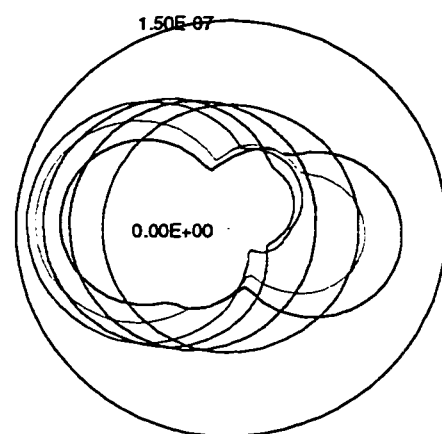
a-1) intercept diagram P4 to P2



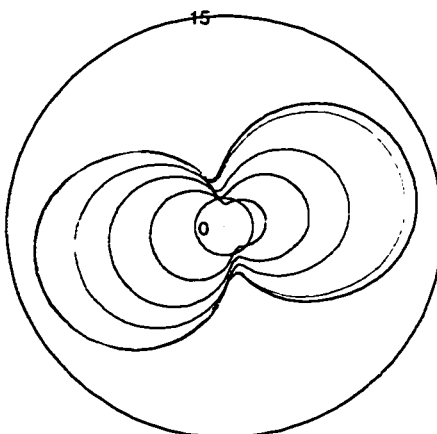
a-2) flow diagram P4 to P2



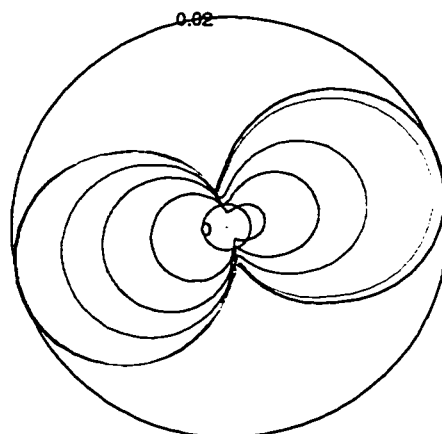
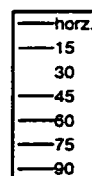
b-1) intercept diagram P2 to B2



b-2) flow diagram P2 to B2



c-1) intercept diagram B2 to lower B1



c-2) flow diagram B2 to lower B1

Figure 3-10: Well 2 flow and intercept diagrams by divided units.

The Pardonet and Baldonnel are divided into 3 intervals: a-1 and a-2 show the intercept and flow diagrams for units P4 to P2; b-1 and b-2 show the intercept and flow diagrams for units P2 to B2 and; c-1 and c-2 show the intercept and flow diagrams for the B2 to lower B1 units.

Well 3

Well 3 was drilled into a forelimb. The bedding dips increase from 30 degrees at the top to about 55 degrees in the middle interval. Then the well passes through a fault. The bedding dips beneath the fault are approximately 25 degrees and decrease to low angles in the Charlie Lake Formation. The structural analysis using the upper Triassic bedding poles gave an eigenvector fold axis with a plunge of 13 degrees toward an azimuth of 135 (13/135). Well 3 has the greatest plunge in the nine well study. However, seismic data does support such a significant plunge associated with this well (Figure 1-4). The fractures are rotated using this fold axis as outlined in Chapter 2 by first removing the fold plunge followed by a rotation of the dip domains. The results of the rotations to the bedding and fracture poles are shown in Figure 3-11.

The well path in dip and strike views is shown in Figure 3-12. The well was drilled at approximately 15 degrees from vertical towards the SW. Relative to bedding, the well entered at a high angle in the SE direction and decreased in angle towards the fault. The well path remained at a high angle relative to bedding beneath the fault.

The rotated fracture poles and planes are shown in Figures 3-13, a & b. Most of the fractures are at high angles relative to bedding with the majority of the fracture poles in the SE quadrant having a single strike orientation between 020 and 030 degrees. This set does not classify as a Stearns type fracture.

The occurrence weighted contoured stereonet and rose diagram (Figures 3-13, c & d) are nearly identical to the unweighted data.

The fracture intercept and flow diagrams for the entire interval are shown in Figures 3-13, e&f. The fracture intercept diagram predicts the maximum fracture sampling in a

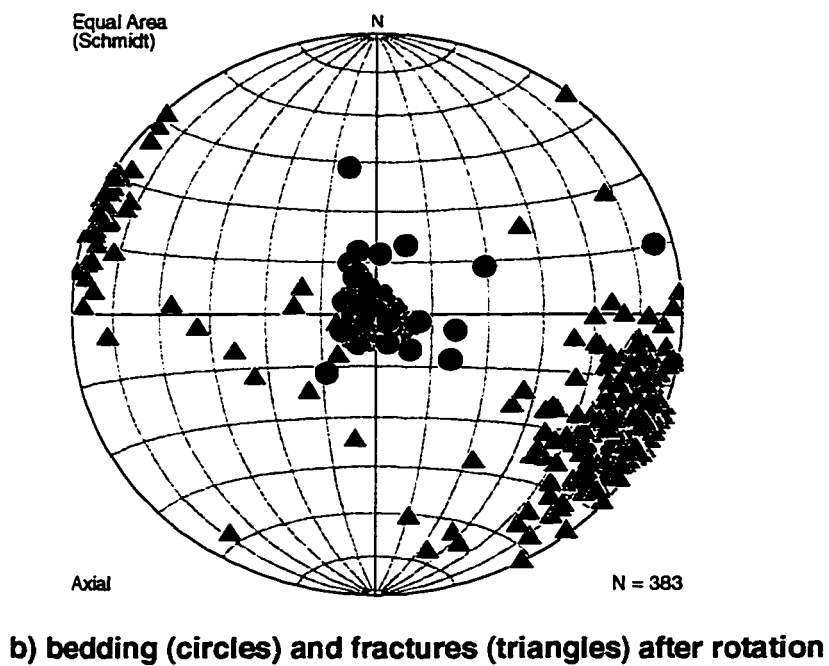
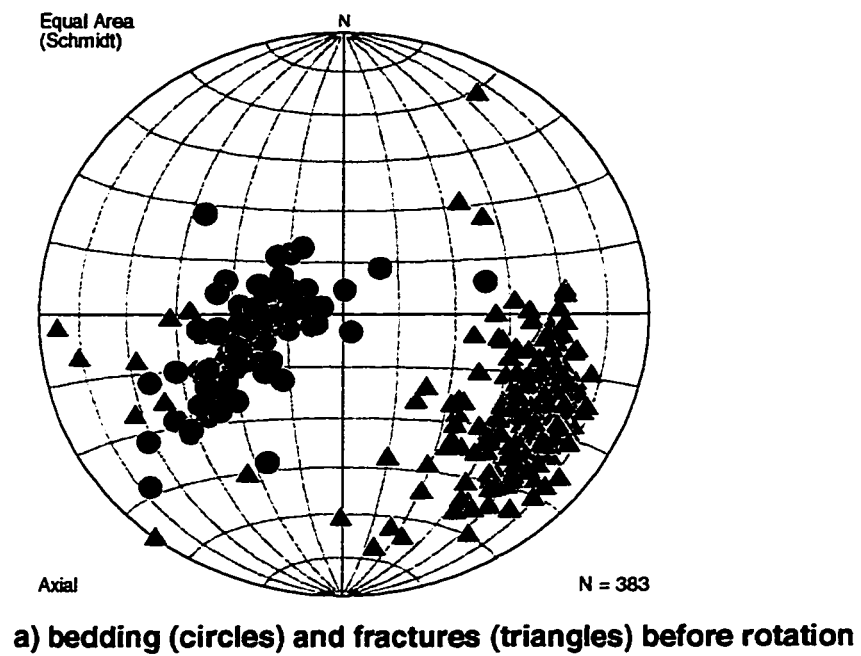


Figure 3-11: Well 3 bedding and fracture data.

Stereonet projection of fracture and bedding poles before and after rotation.

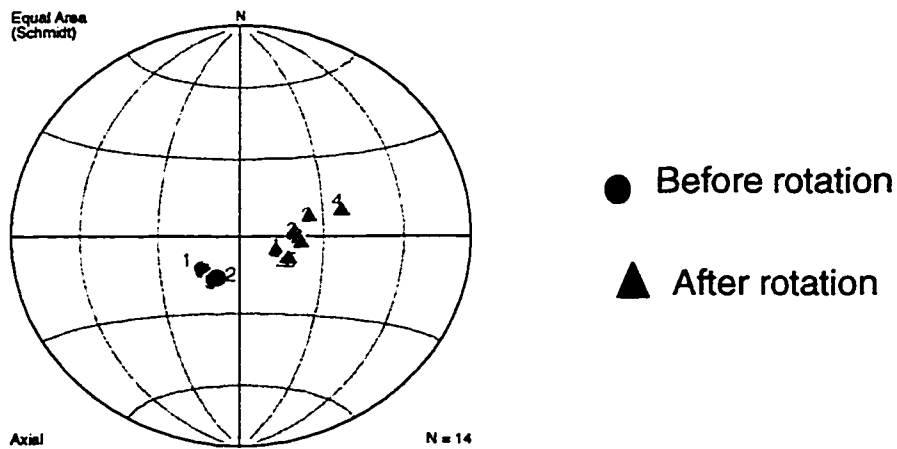
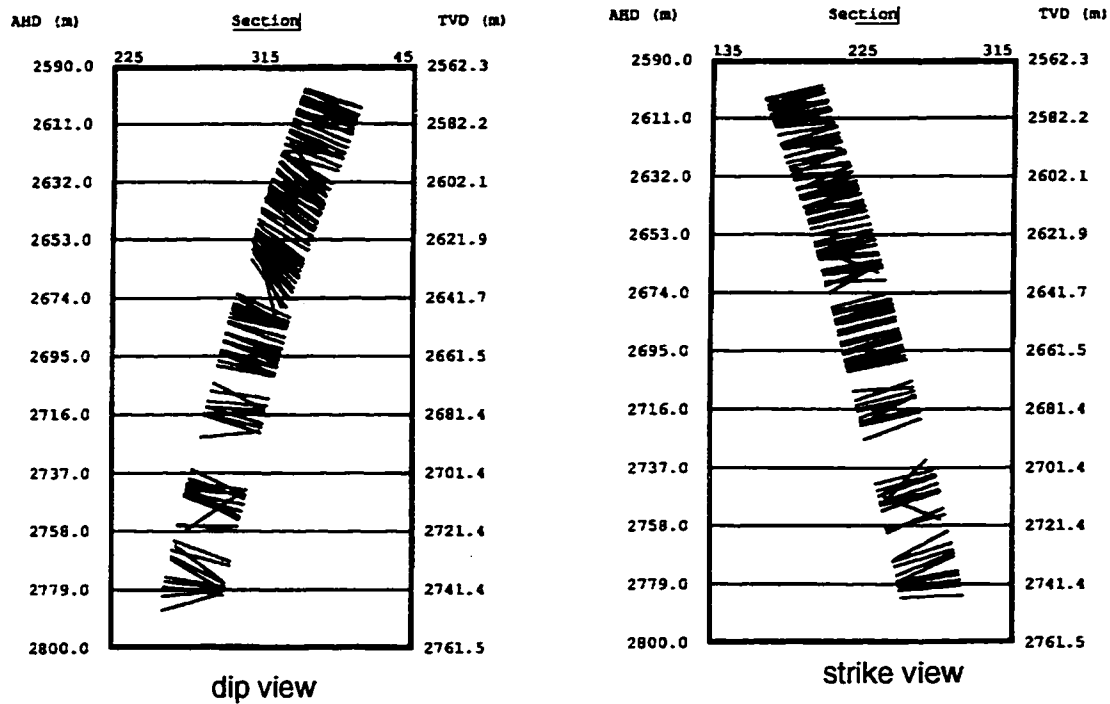


Figure 3-12: Well 3 well path.

Well path is shown in dip and strike sections and in a stereonet projection of the well path before and after bedding rotation.

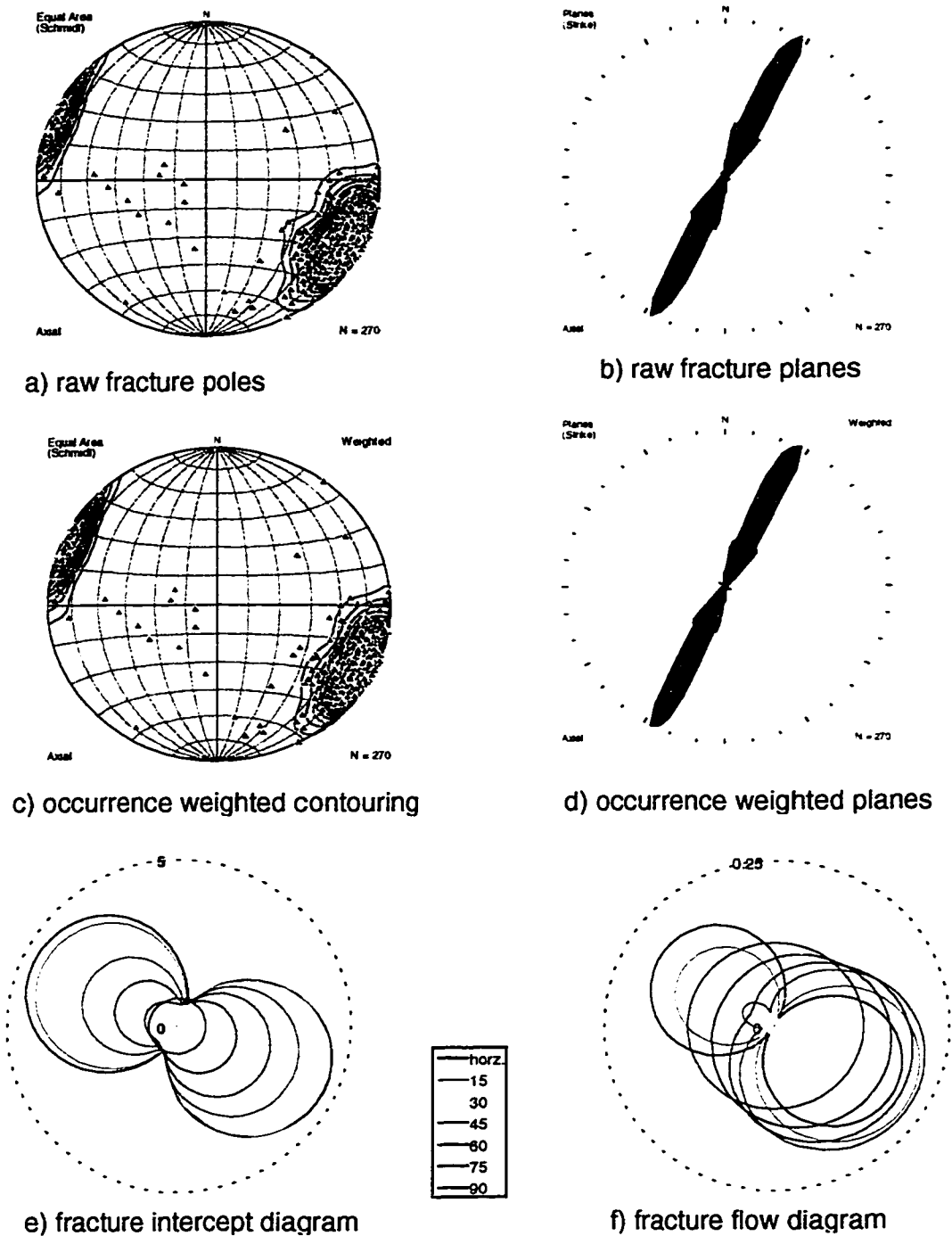


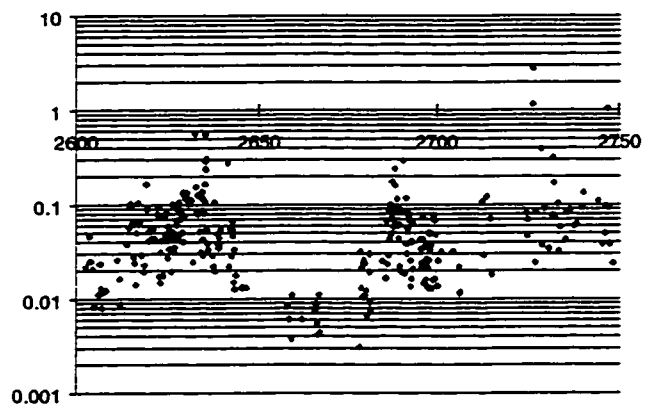
Figure 3-13: Well 3 occurrence correction, flow and intercept diagrams.

Rotated fracture poles and strikes before and after occurrence correction are shown in figures a through d. Fracture intercept and flow rate diagrams for upper Triassic interval are shown in figures e and f.

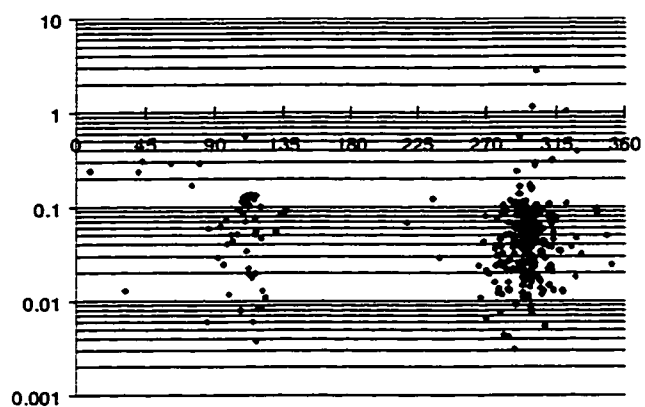
SE or NW direction, with a slightly higher intercept towards the southeast. The fracture intercept rate increases as the sample direction changes inclination from vertical (90 degrees) to horizontal (0 degrees), relative to bedding.

The flow intercept diagram predicts maxima in the SE and NW directions. There is an asymmetry with the eastern direction being significantly better particularly at the higher drilling angles. The maximum flow intercept is at moderate inclinations with the maximum at 30 degrees, followed by 45, 15, 60 and then horizontal. The unusual flow pattern is primarily due to two large aperture fractures in the lower unit that have poles at approximately 40 degrees in the SE direction (Figure 3-14c).

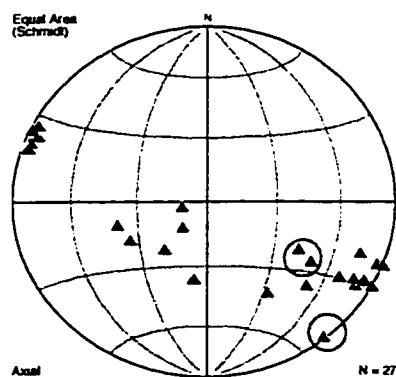
There is little change in fracture orientation with depth in the well (Figure 3-15), however, there are significant changes in the magnitude of the flow and intercept diagrams. The upper unit is the most fractured with a maximum intercept rate of nearly 10 fractures per meter compared to 4 for the lower unit and 1.6 for the middle unit. The lower unit has the greatest volume of open fractures per meter even though this unit is less densely fractured than the upper unit. The resulting volume is approximately 20 times greater than the lower unit and over two orders of magnitude greater than the middle unit.



a) fracture aperture versus measured drilling depth (m)



b) fracture aperture versus dip direction azimuth



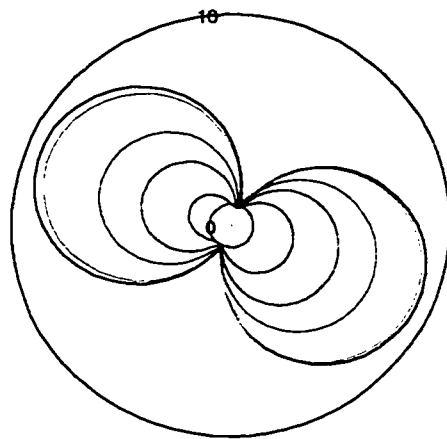
c) large aperture fracture poles on stereonet



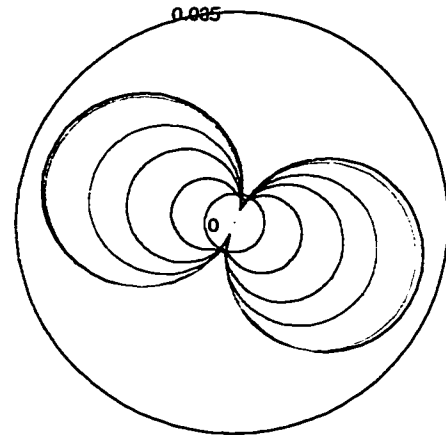
d) large aperture fracture strike direction on weighted rose diagram

Figure 3-14: Well 3 fracture aperture relationships.

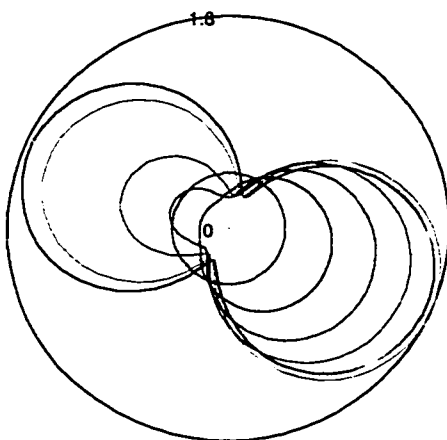
Fracture aperture relationships as a function of depth and azimuth (a and b). The 10% of fractures with the largest apertures are shown on stereonet and rose diagram (c and d).



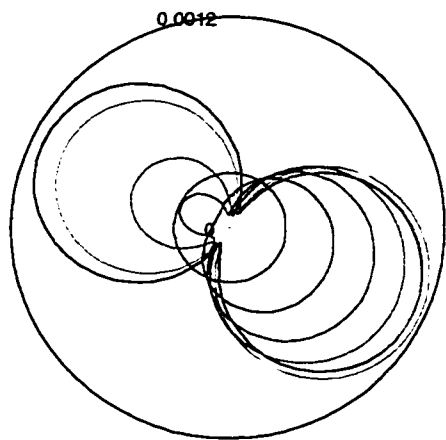
a-1) intercept diagram P4 to P2



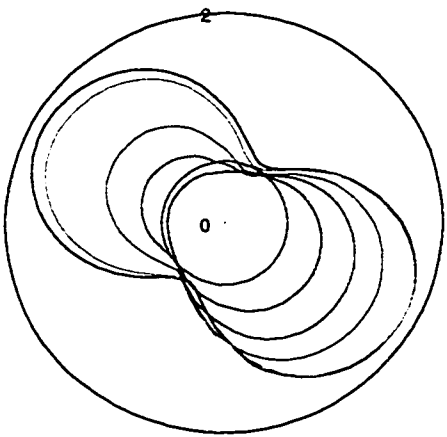
a-2) flow diagram P4 to P2



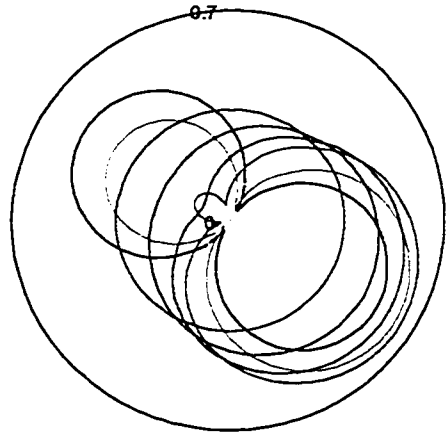
b-1) intercept diagram P2 to B2



b-2) flow diagram P2 to B2



c-1) intercept diagram B2 to CLLK



c-2) flow diagram B2 to CLLK

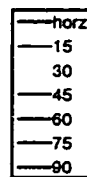


Figure 3-15: Well 3 flow and intercept diagrams by divided units.

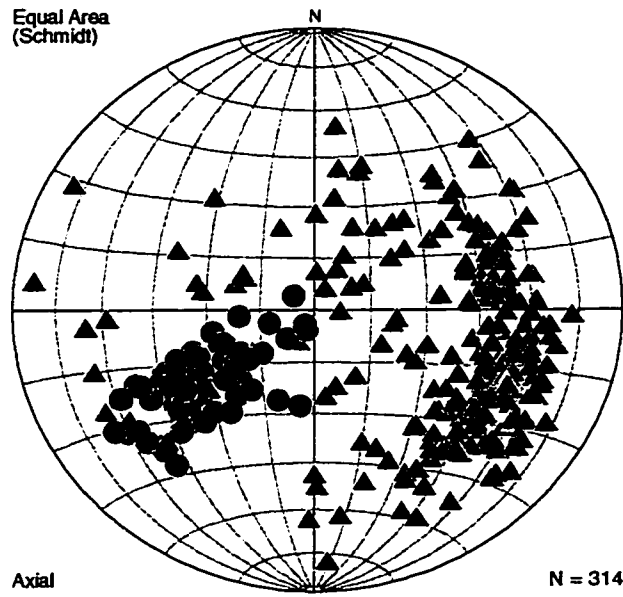
The Pardonet and Baldonnel are divided into 3 intervals: a-1 and a-2 show the intercept and flow diagrams for units P4 to P2; b-1 and b-2 show the intercept and flow diagrams for units P2 to B2 and; c-1 and c-2 show the intercept and flow diagrams for the B2 to Charlie Lake Formation units.

Well 4

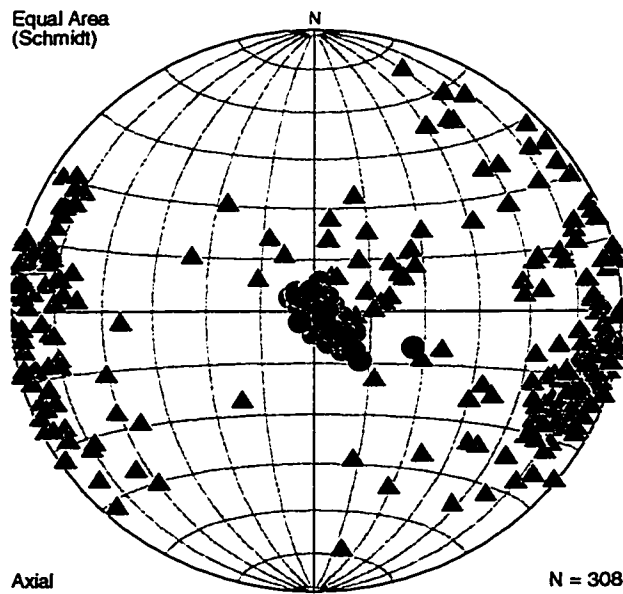
Well 4 was drilled into a forelimb with beds dipping down towards the northeast. The bedding dips increase from 45 degrees at the top to about 55 degrees in the middle interval and decrease toward the bottom to approximately 10 degrees just above the Charlie Lake Formation. The structural analysis using the upper Triassic bedding poles gives an eigenvector fold axis with a plunge of 03 degrees towards an azimuth of 146. The fractures are rotated using this fold axis as outlined in Chapter 2 by first removing the fold plunge followed by a rotation of the dip domains. The resulting rotations are shown in Figure 3-16.

The well path in dip and strike views are shown in Figure 3-17. The well was drilled at approximately 15 degrees from vertical towards the SE. Relative to bedding, the well entered at a approximately 30 degrees in the eastern direction. As the bedding dip increases in the middle interval, the relative well path is at a lower angle relative to bedding. In the bottom interval the bedding dips decrease and the relative well path increases in angle relative to bedding.

The rotated fracture poles and planes are shown in Figures 3-18, a & b. Most of the fractures are at high angles relative to bedding with the majority of the fracture poles in the SE and NW quadrant, having a strike orientation between 005 and 035 degrees. This fracture group is divided into two, a large group with a strike between 005 and 015 degrees and a second smaller group with a strike near 030 degrees. These two sets fall between the orientations of Type 1 and 2 fractures. There is another minor set striking between 160 and 170 degrees that has the orientation of a Type 2 shear fracture.



a) bedding (circles) and fractures (triangles) before rotation



b) bedding (circles) and fractures (triangles) after rotation

Figure 3-16: Well 4 bedding and fracture data.

Stereonet projection of fracture and bedding poles before and after rotation.

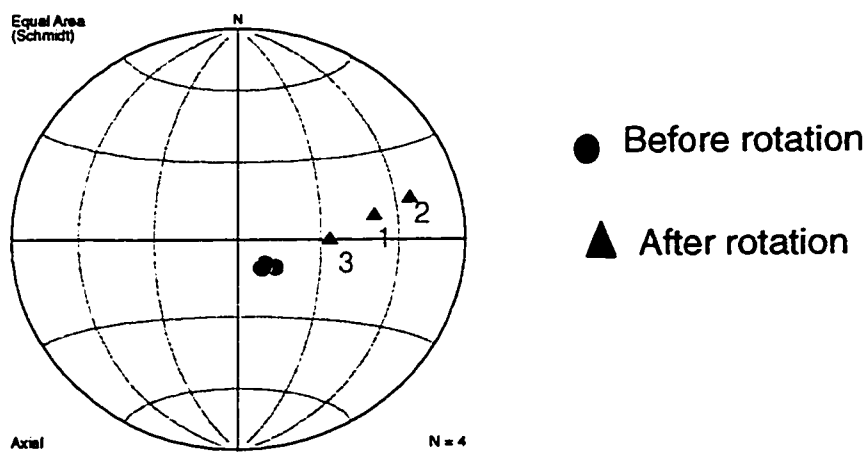
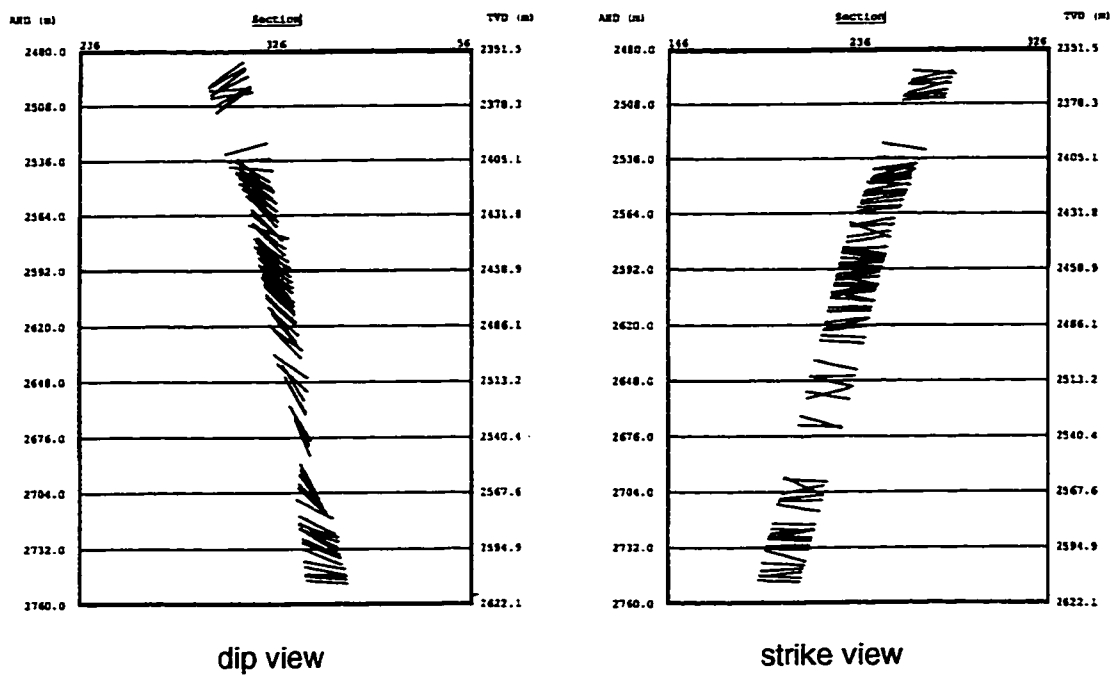
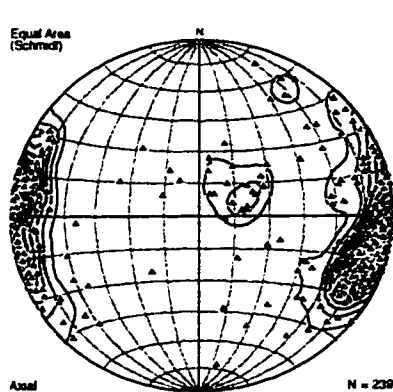


Figure 3-17: Well 4 well path.

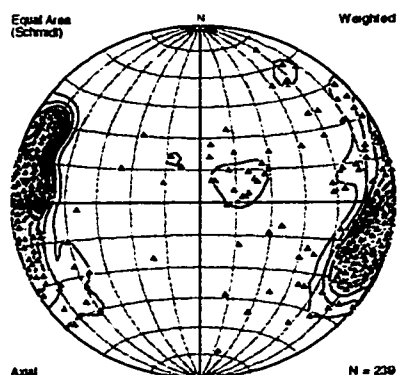
Well path is shown in dip and strike sections and in a stereonet projection of the well path before and after bedding rotation.



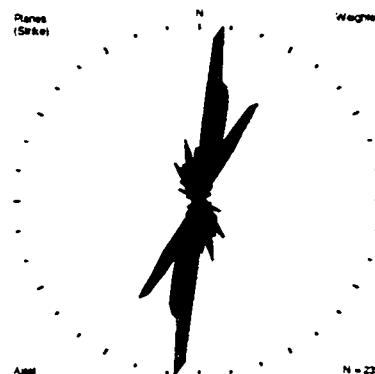
a) raw fracture poles



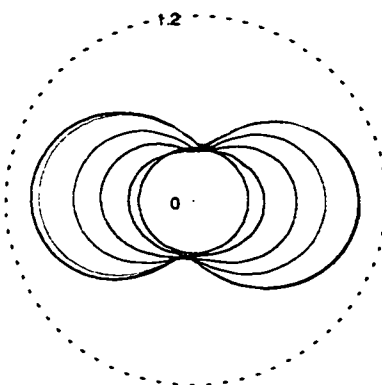
b) raw fracture planes



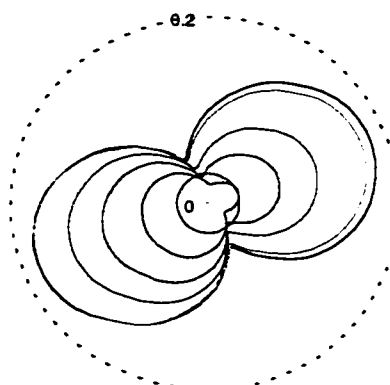
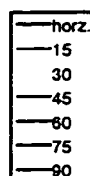
c) occurrence weighted contouring



d) occurrence weighted planes



e) fracture intercept diagram



f) fracture flow diagram

Figure 3-18: Well 4 occurrence correction, flow and intercept diagrams.

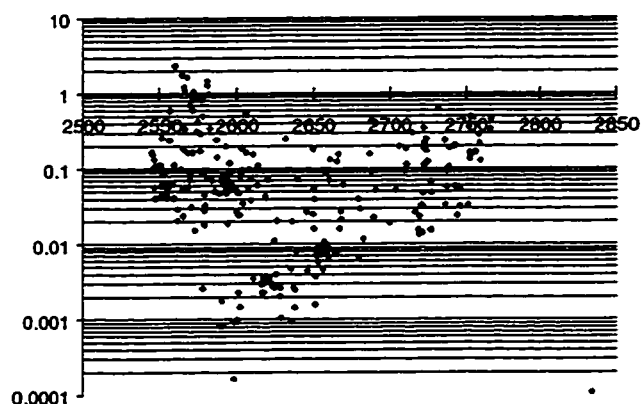
Rotated fracture poles and strikes before and after occurrence correction are shown in figures a through d. Fracture intercept and flow rate diagrams for upper Triassic interval are shown in figures e and f.

The occurrence weighted contoured stereonet and rose diagram (Figures 3-18 c & d) are similar to the raw data. However the two more common sets become more distinguishable.

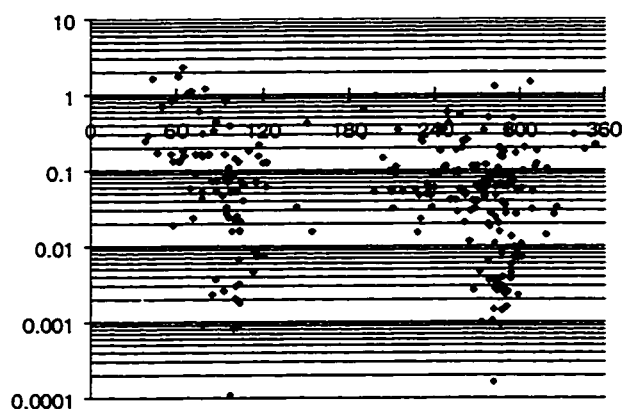
The fracture intercept and flow diagrams for the entire interval are shown in Figures 3-18, e&f. The fracture intercept diagram predicts the maximum fracture sampling in a SE or NW direction. The intercept diagram is very symmetric with only a slightly greater fracture density intercepted in the eastern direction. The fracture intercept rate increases as the sample direction changes inclination from vertical (90 degrees) to horizontal (0 degrees), relative to bedding.

The flow intercept diagram has predicted maxima in the NE and SW directions. There is an asymmetry with the SW direction being better particularly at the higher drilling angles (Figure 3-19c). This is due to a concentration of larger aperture fracture poles in the SW quadrant with strikes consistent with Type 2 fractures (Figure 3-19, c&d).

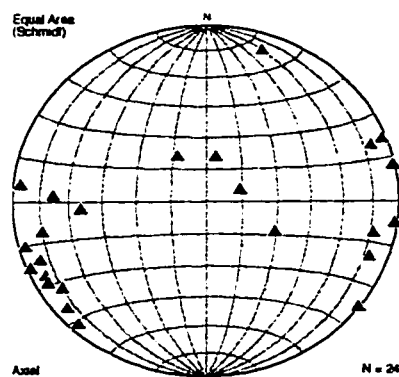
The upper unit has the greatest fracture density with a maximum of nearly 2.5 fractures per meter (Figure 3-20). The middle unit has a maximum of nearly 1.6 fractures per meter and the lower unit is the least densely fractured unit with a maximum density less than 0.8 fractures per meter. The upper unit also has the greatest fracture volume per meter with the maximum greater than two orders of magnitude higher than the maxima in the other two units.



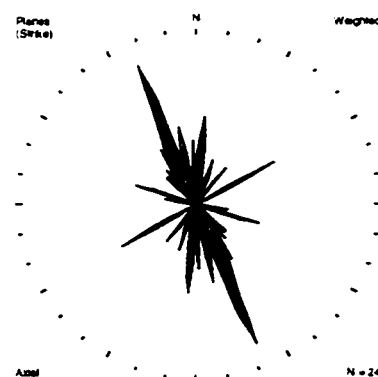
a) fracture aperture versus measured drilling depth (m)



b) fracture aperture versus fracture dip direction azimuth



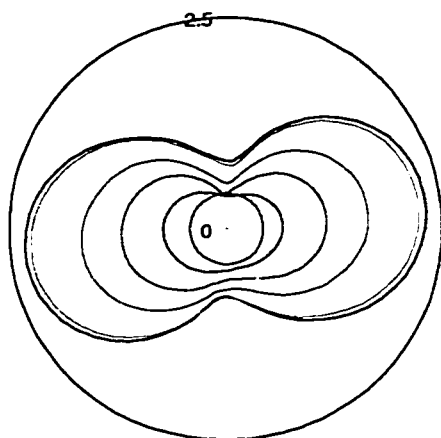
c) large aperture fracture poles on stereonet



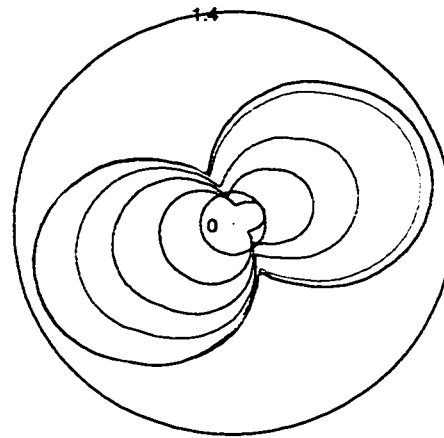
d) large aperture fracture strike direction on weighted rose diagram

Figure 3-19: Well 4 fracture aperture relationships.

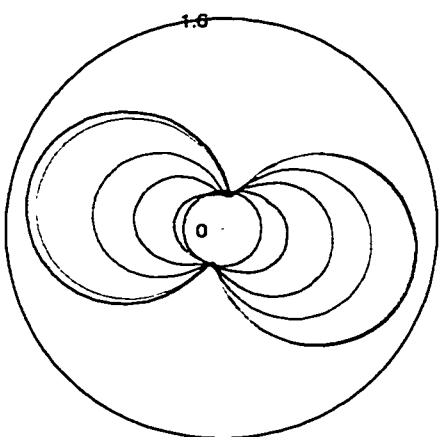
Fracture aperture relationships as a function of depth and azimuth (a and b). The 10% of fractures with the largest apertures are shown on stereonet and rose diagram (c and d).



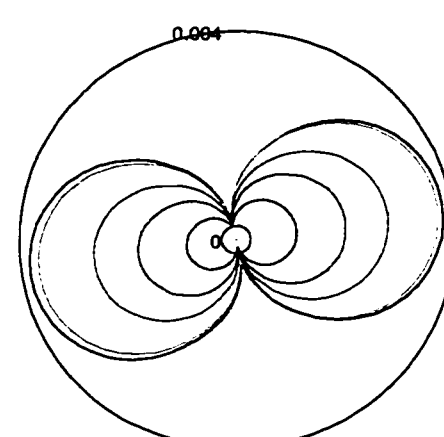
a-1) intercept diagram P4 to P2



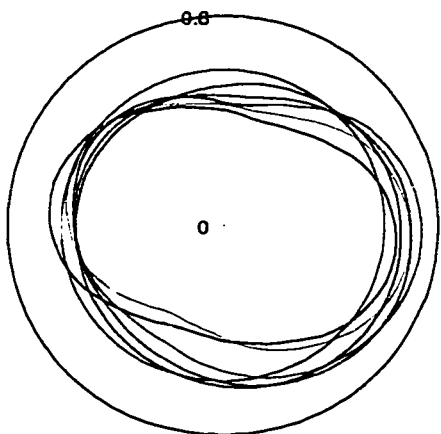
a-2) flow diagram P4 to P2



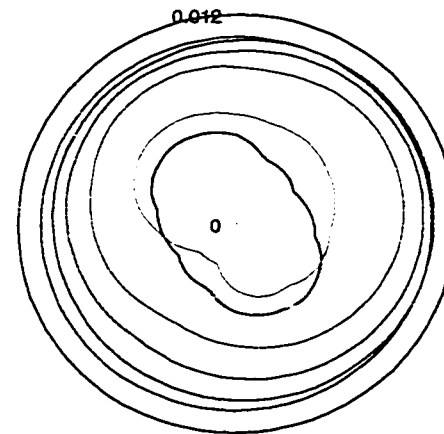
b-1) intercept diagram P2 to B2



b-2) flow diagram P2 to B2



c-1) intercept diagram B2 to CLLK



c-2) flow diagram B2 to CLLK

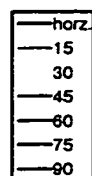


Figure 3-20: Well 4 flow and intercept diagrams by divided units.

The Pardonet and Baldonnel are divided into 3 intervals: a-1 and a-2 show the intercept and flow diagrams for units P4 to P2; b-1 and b-2 show the intercept and flow diagrams for units P2 to B2 and; c-1 and c-2 show the intercept and flow diagrams for the B2 to the Charlie Lake Formation units.

In the upper two units, the orientation of the predicted maximum intercept direction is nearly east and west. Both flow diagrams have a maximum oriented slightly north of east. These directions are biased by larger aperture fractures with a Type 2 orientation.

The lower B2 to Charlie Lake Formation interval has an unusual intercept and flow diagram (Figure 3-20, c-1 & c-2). The intercept diagram shows only a slight improvement in maxima at lower angles compared to the vertical sampling direction. The flow diagram shows a decrease in intercepted fracture volume as the sampling direction becomes more horizontal. This unusual pattern is due to the fractures being at low angles relative to bedding in the lower interval.

Well 5

Well 5 was drilled into a gently dipping backlimb with beds dipping down towards the southwest. The bedding dips increase from 15 degrees at the top to about 30 in the lower unit. The structural analysis using the upper Triassic bedding poles gives an eigenvector fold axis with a plunge of 0 degrees toward an azimuth of 124. The fractures are rotated using this fold axis as outlined in Chapter 2 by rotation of the dip domains. The resulting rotations are shown in Figure 3-21.

The well path in dip and strike views is shown in Figure 3-22. The well was drilled nearly vertically with a steep inclination towards the NE. Relative to horizontal bedding, the well entered at a approximately 75 degrees from horizontal in the southwestern direction and became more vertical near the base of the lower formation.

The rotated fracture poles and planes are shown in Figures 3-23, a & b. Most of the fractures are at high angles relative to bedding with the majority of the fracture poles in two groups. One group, with poles on the east and west sides of the stereonet, has strike orientations between 350 and 025 degrees. This group has the most orientations between 005 and 015 degrees. The first group are oriented as Type 1 shear fractures. The second group, with poles on the south side of the stereonet, have strike orientations between 100 and 150 degrees. This group has the most orientations between 100 and 110 degrees. These fractures are oriented as Type 2 extensional and shear sets.

The occurrence weighted contoured stereonet and rose diagram (Figures 3-23 c & d) are significantly different compared to the raw data. The fracture frequency is transformed from several groups to a single dominant set. The set has a pole peak

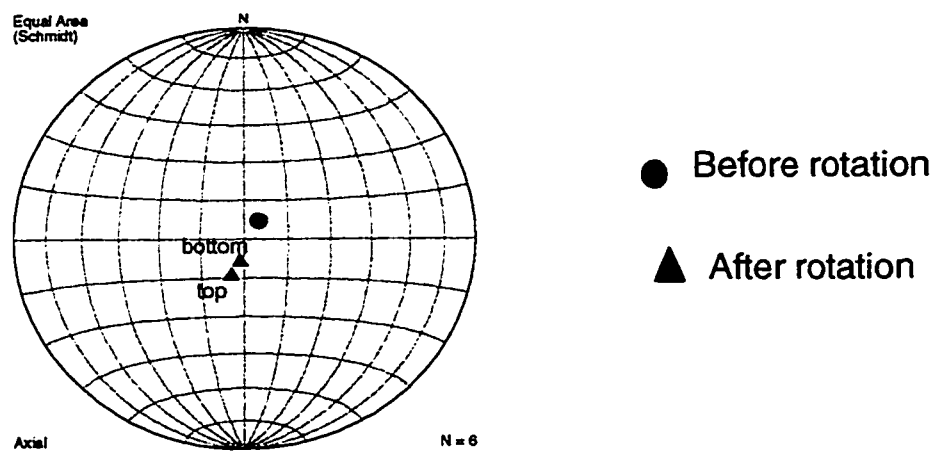
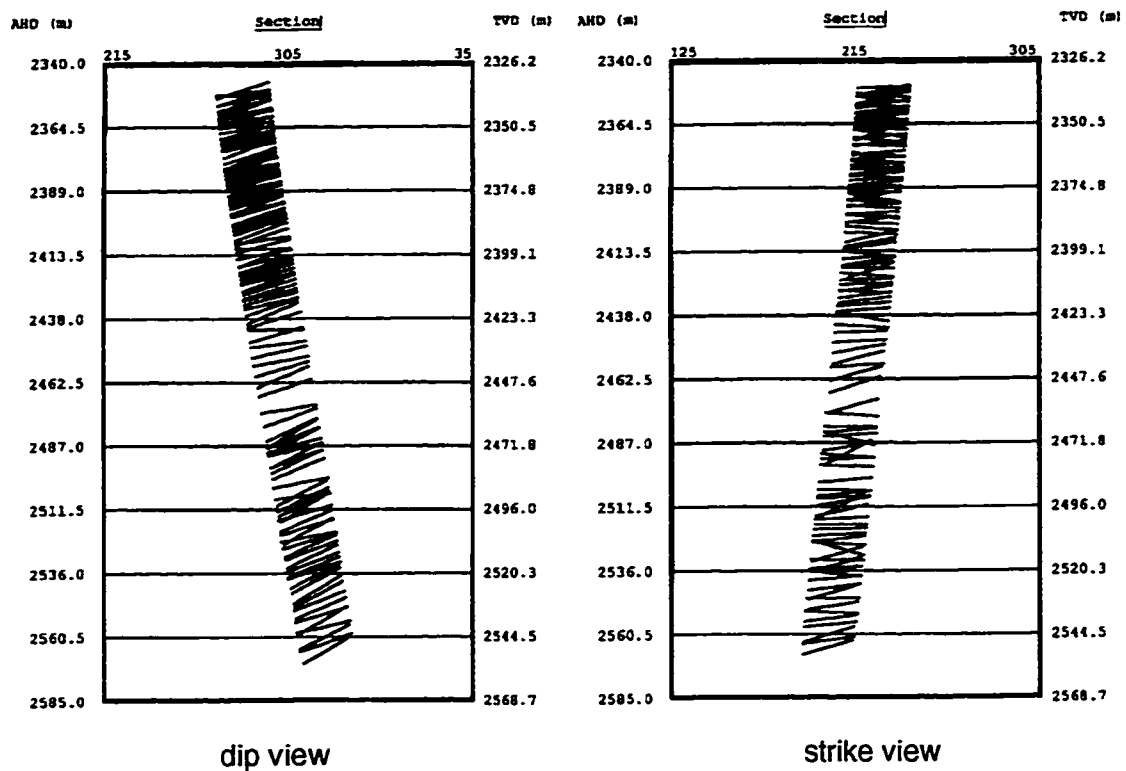
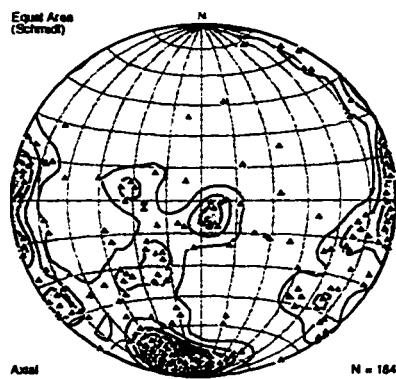


Figure 3-22: Well 5 well path.

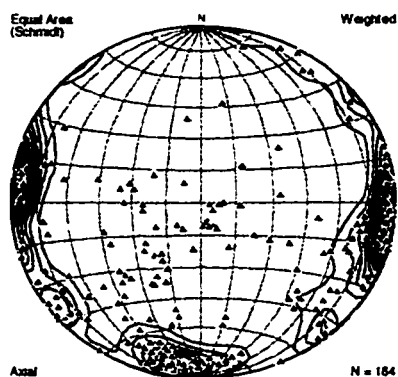
Well path is shown in dip and strike sections and in a stereonet projection of the well path before and after bedding rotation.



a) raw fracture poles



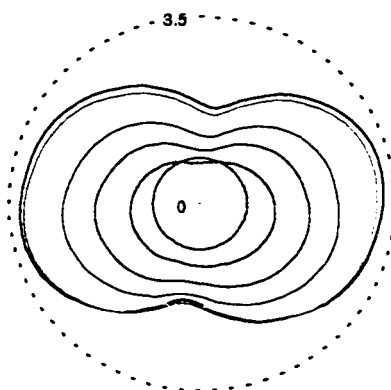
b) raw fracture planes



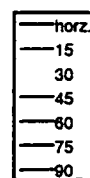
c) occurrence weighted contouring



d) occurrence weighted planes



e) fracture intercept diagram



f) fracture flow diagram

Figure 3-23: Well 5 occurrence correction, flow and intercept diagrams.

Rotated fracture poles and strikes before and after occurrence correction are shown in figures a through d. Fracture intercept and flow rate diagrams for upper Triassic interval are shown in figures e and f.

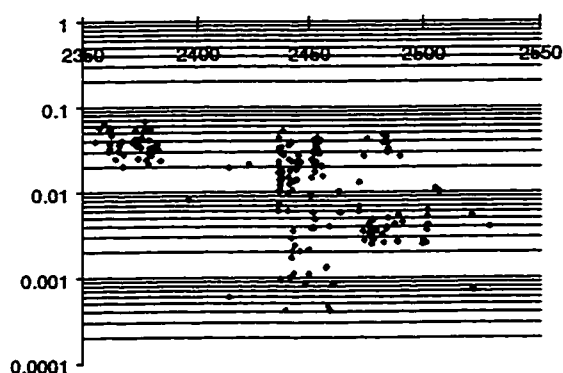
contour on the ESE and WNW sides of the stereonet and strikes approximately 010 degrees.

The fracture intercept and flow diagrams for the interval are shown in Figures 3-23, e&f. The fracture intercept diagram shows the predicted maximum fracture sampling in an east or west direction. The intercept diagram is very symmetric. The fracture intercept rate increases as the sample direction changes inclination from vertical (90 degrees) to horizontal (0 degrees), relative to bedding.

The flow intercept diagram has maxima in the NE and SW directions. This is due to many large aperture fractures oriented in the Type 2 orientation (Figure 3-24c).

The upper unit has the greatest fracture density with a maximum of 12 fractures per meter (Figure 3-25). The middle unit has a maximum of nearly 0.8 fractures per meter and the lower has a maximum density of 4 fractures per meter. The upper unit also has the greatest fracture volume per meter with the maximum approximately one order of magnitude greater than the middle interval and two orders of magnitude greater than the lower unit.

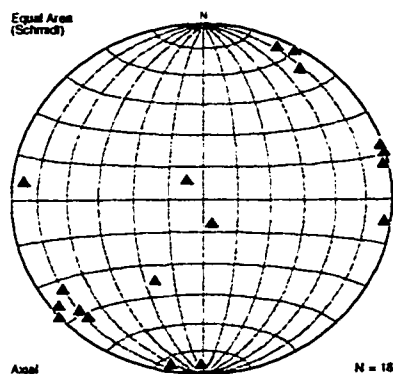
In the upper unit the orientations of the maxima in the intercept diagram and flow diagram are east/west and ENE/WSW respectively (Figures 3-25, a-1 & a-2). Both of these diagrams are nearly symmetric. The orientations for the lower two units (3-25, b1 through c-2) are variable. The intercept patterns in Figures b1, b2 and c2 are more circular than usual. This is due to a more equal weighting of the two perpendicular fracture sets. The intercept patterns in Figure c2 are more oval due to large aperture fractures with poles in the SW orientation (Type 2).



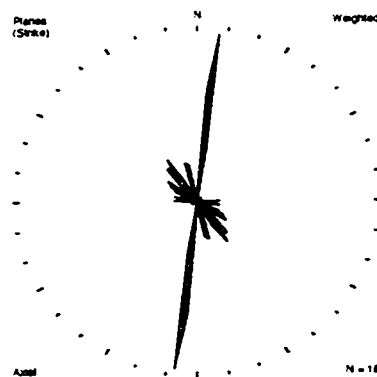
a) fracture aperture versus measured drilling depth (m)



b) fracture aperture versus fracture dip direction azimuth



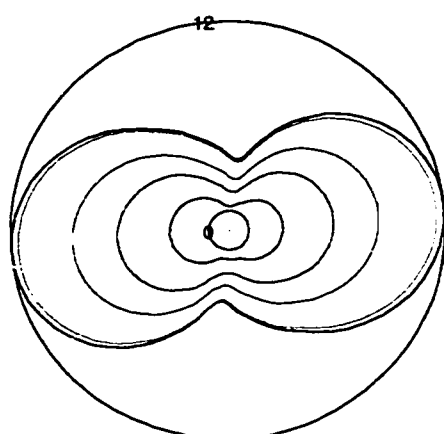
c) large aperture fracture poles on stereonet



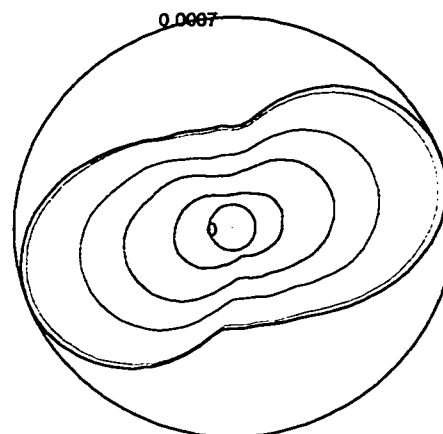
d) large aperture fracture strike direction on weighted rose diagram

Figure 3-24: Well 5 fracture aperture relationships.

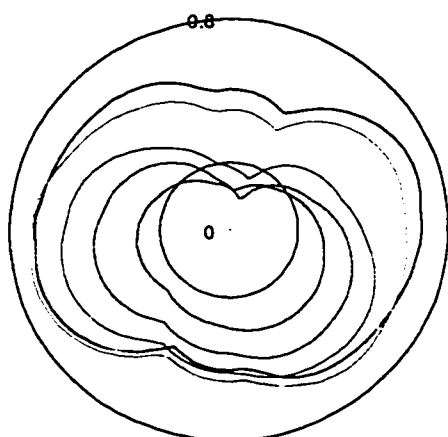
Fracture aperture relationships as a function of depth and azimuth (a and b). The 10% of fractures with the largest apertures are shown on stereonet and rose diagram (c and d).



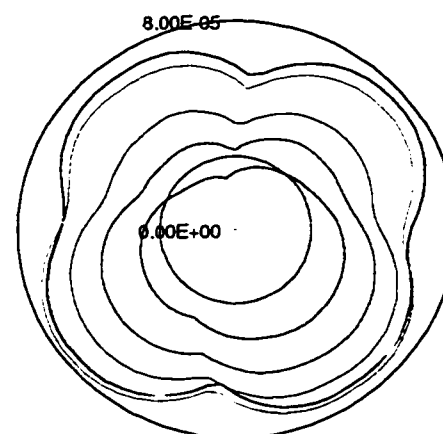
a-1) intercept diagram P4 to P2



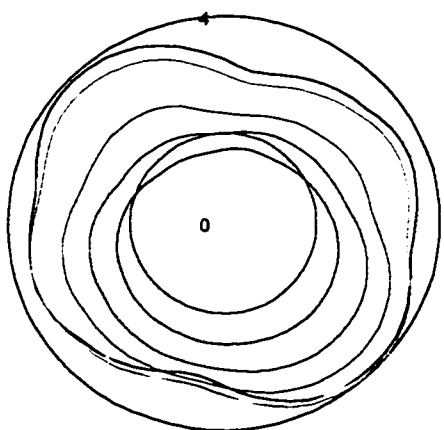
a-2) flow diagram P4 to P2



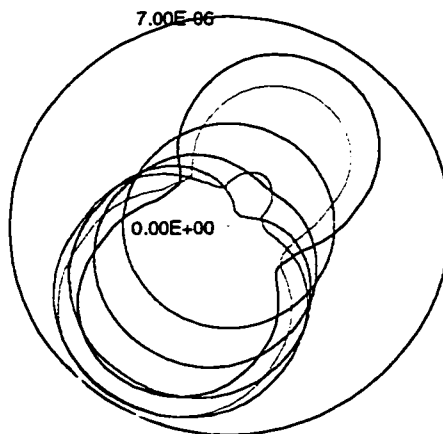
b-1) intercept diagram P2 to B2



b-2) flow diagram P2 to B2



c-1) intercept diagram B2 to CLLK



c-2) flow diagram B2 to CLLK

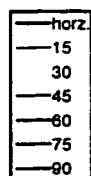


Figure 3-25: Well 5 flow and intercept diagrams by divided units.

The Pardonet and Baldonnel are divided into 3 intervals: a-1 and a-2 show the intercept and flow diagrams for units P4 to P2; b-1 and b-2 show the intercept and flow diagrams for units P2 to B2 and; c-1 and c-2 show the intercept and flow diagrams for unit B2 to the Charlie Lake Formation.

Well 6

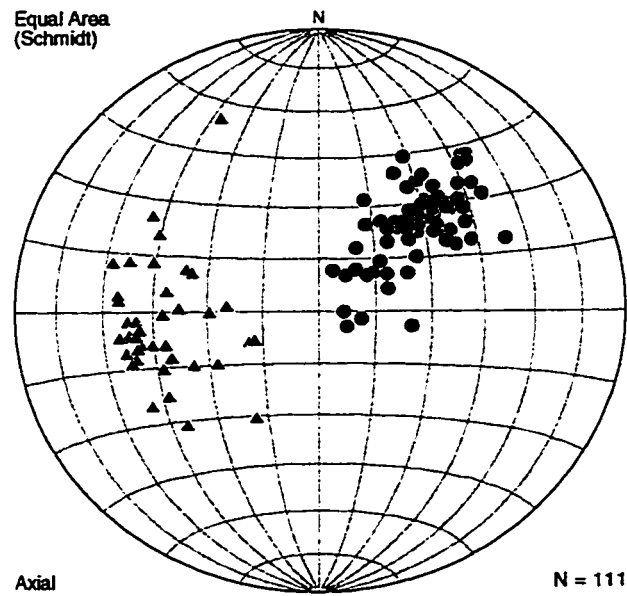
Well 6 was drilled into a backlimb with beds dipping down towards the southwest. The beds dip at approximately 40 degrees in the upper portion of the well. The well passes through a hinge and the dips increase to 60 degrees for a short interval. Then the well passes through another hinge and the bedding dips return to approximately 40 degrees.

The structural analysis using the upper Triassic bedding poles gives an eigenvector fold axis with a plunge of 04 degrees toward an azimuth of 311. The fractures are rotated using this fold axis as outlined in Chapter 2 by first removing the fold plunge followed by a rotation of the dip domains. The resulting rotations are shown in Figure 3-26.

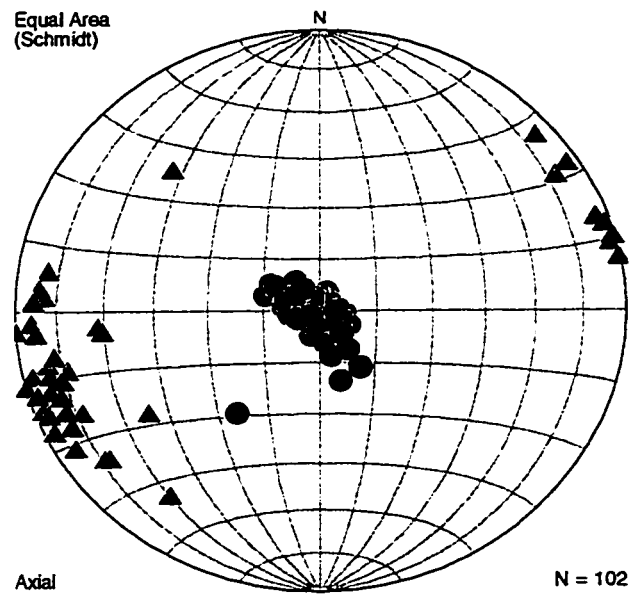
The well path in dip and strike views is shown in Figure 3-27. The well was directed approximately 75 degrees from horizontal towards the NE. Relative to bedding, the well entered at a approximately 75 degrees to the SW and became shallower at 60 degrees to the SW across the hinge. The well returns to 75 degrees to the SW when it crosses the second hinge and remains relatively constant to the base of the B1 unit.

The rotated fracture poles and planes are shown in Figures 3-28, a & b. Most of the fractures are at high angles relative to bedding with the majority of the fracture poles in the SW quadrant. These fractures have a strike direction between 140 and 180 degrees. The occurrence weighted contoured stereonet and rose diagram (Figures 3-28 c & d) show little change in the relative fracture frequency.

The fracture intercept and flow diagrams for the interval are shown in Figures 3-28, e&f. Both diagrams predicted maximum orientations in the ENE and WSW directions.



a) bedding (circles) and fractures (triangles) before rotation



b) bedding (circles) and fractures (triangles) after rotation

Figure 3-26: Well 6 bedding and fracture data.

Stereonet projection of fracture and bedding poles before and after rotation.

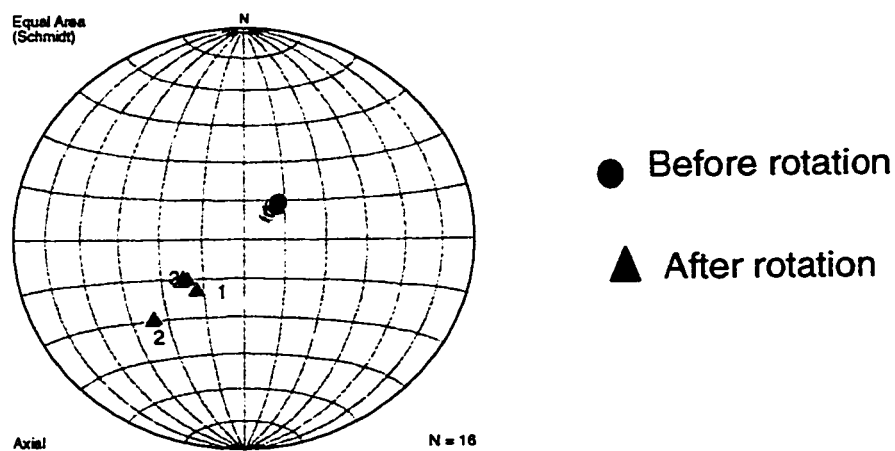
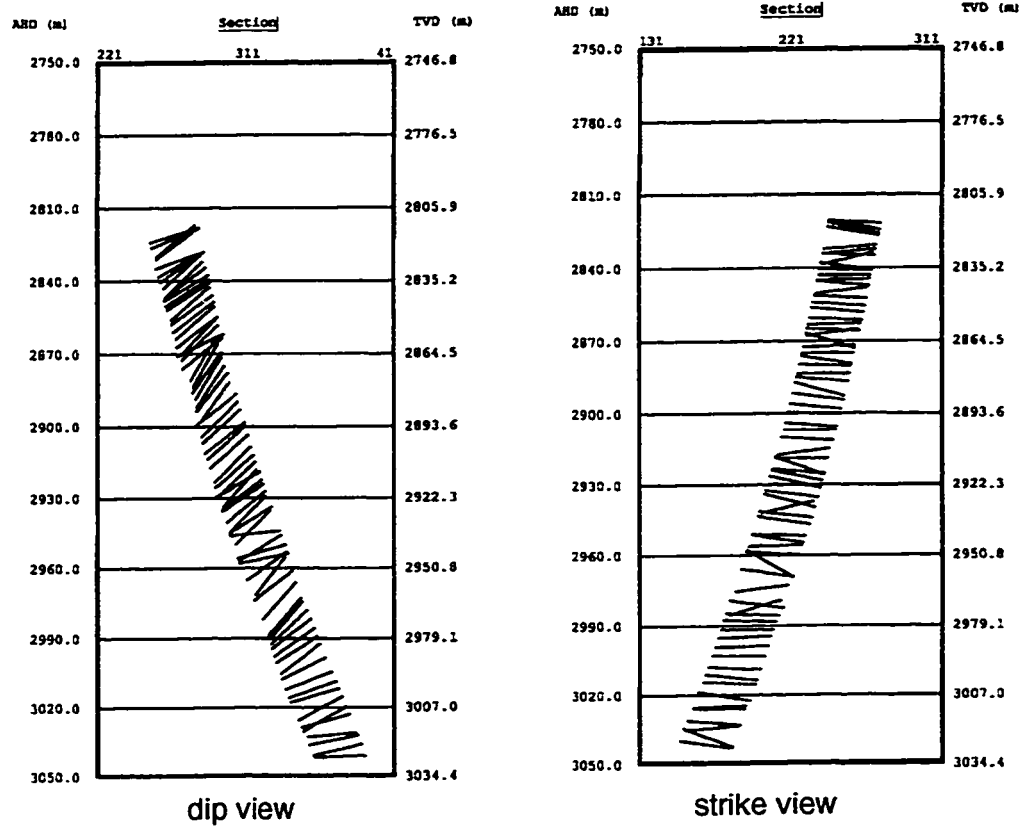
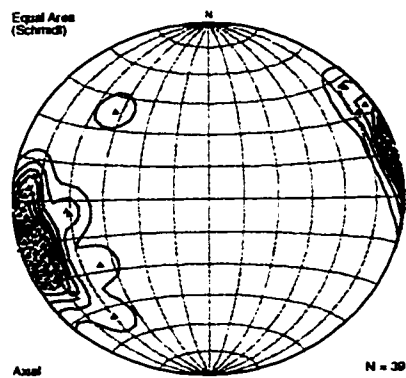
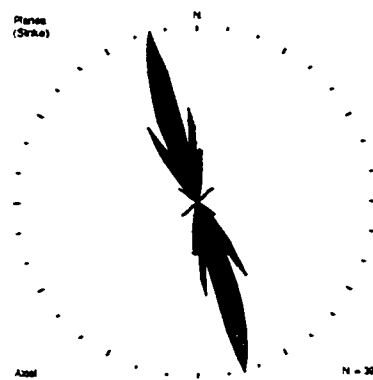


Figure 3-27: Well 6 well path.

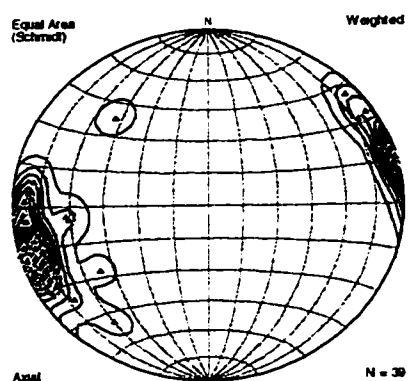
Well path is shown in dip and strike sections and in a stereonet projection of the well path before and after bedding rotation.



a) raw fracture poles



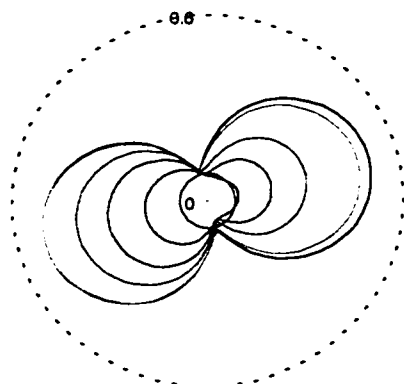
b) raw fracture planes



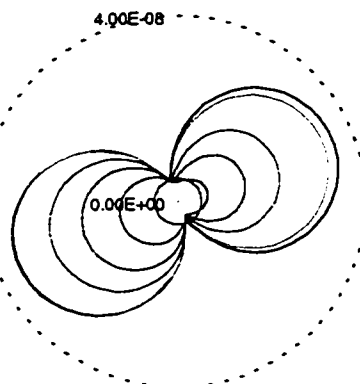
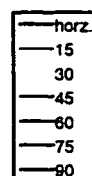
c) occurrence weighted contouring



d) occurrence weighted planes



e) fracture intercept diagram



f) fracture flow diagram

Figure 3-28: Well 6 occurrence correction, flow and intercept diagrams.

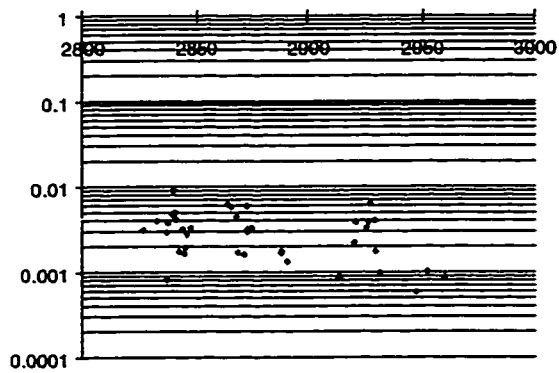
Rotated fracture poles and strikes before and after occurrence correction are shown in figures a through d. Fracture intercept and flow rate diagrams for upper Triassic interval are shown in figures e and f.

Both diagrams are slightly asymmetric, with increased values on the west side. The fracture and flow intercept rate increases as the sample direction changes inclination from vertical (90 degrees) to horizontal (0 degrees).

The fracture aperture relationships are shown in Figure 3-29. Well 6 has the fewest fractures and the smallest variance in the range of fracture apertures when compared to the other wells. (The reason Well 6 and Well 4 have fewer fractures as compared to the other wells is discussed in Chapter 4). Three of the largest four fractures are at high angles to bedding and strike to the north and NNW/SSE (Figure 3-29, c&d). The fourth fracture has a unique orientation relative to all the fractures in the well, being at a lower angle relative to bedding (60 degrees) and striking NE/SW.

The upper unit has the greatest predicted fracture density with a maximum of 1.4 fractures per meter (Figure 3-30). The middle unit has a maximum of nearly 0.8 fractures per meter and the lower unit has a maximum density of 0.5 fractures per meter. The upper unit also has the greatest fracture volume per meter with the maximum approximately one order of magnitude greater than that in the middle interval and lower intervals

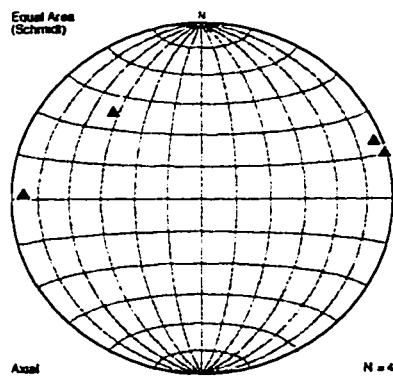
All intervals have similar orientations of maxima in both intercept and flow diagrams (Figure 3-30). The orientations of the maxima are toward the ENE and WSW. Five of the six diagrams are asymmetric with greater maxima on the west side. The exception is the flow diagram for the lower unit that has a slightly greater maximum on the east side.



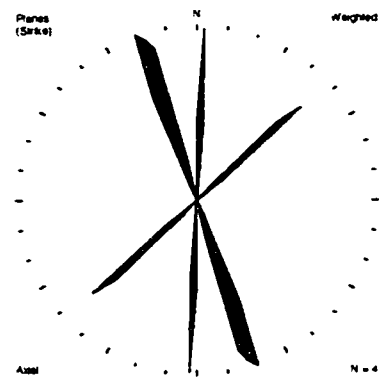
a) fracture aperture versus measured drilling depth (m)



b) fracture aperture versus fracture dip direction azimuth



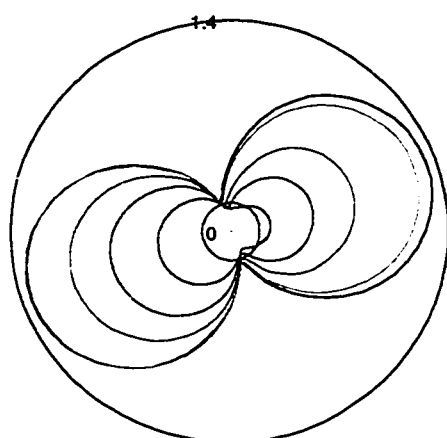
c) large aperture fracture poles on stereonet



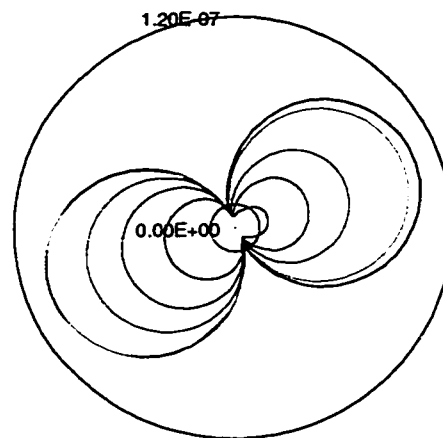
d) large aperture fracture strike direction on weighted rose diagram

Figure 3-29: Well 6 fracture aperture relationships.

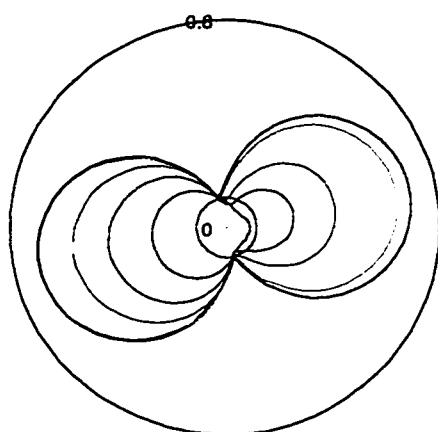
Fracture aperture relationships as a function of depth and azimuth (a and b). The 10% of fractures with the largest apertures are shown on stereonet and rose diagram (c and d).



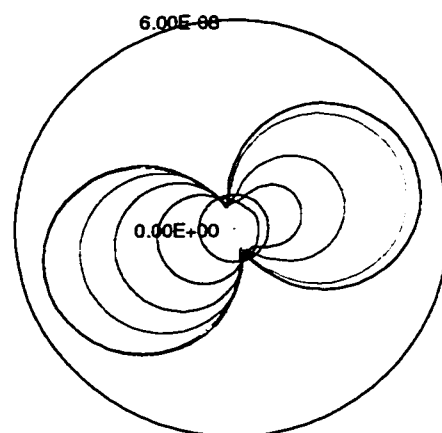
a-1) intercept diagram P4 to P2



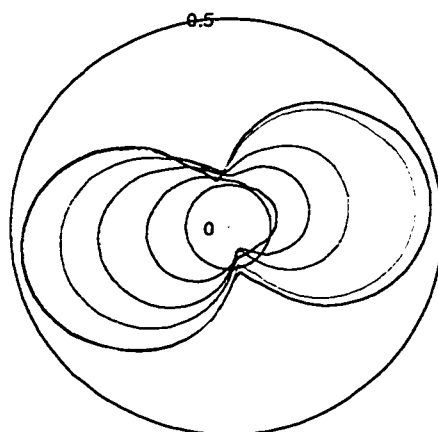
a-2) flow diagram P4 to P2



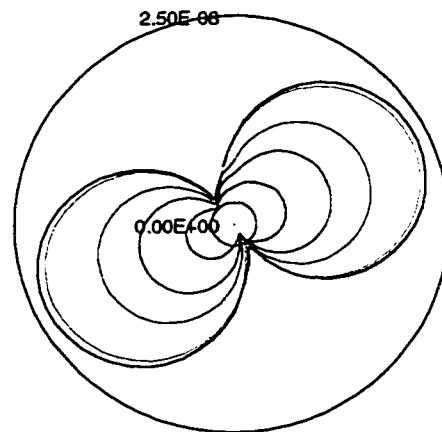
b-1) intercept diagram P2 to B2



b-2) flow diagram P2 to B2



c-1) intercept diagram B2 to CLLK



c-2) flow diagram B2 to CLLK

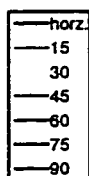


Figure 3-30: Well 6 flow and intercept diagrams by divided units.

The Pardonet and Baldonnel are divided into 3 intervals: a-1 and a-2 show the intercept and flow diagrams for units P4 to P2; b-1 and b-2 show the intercept and flow diagrams for units P2 to B2 and; c-1 and c-2 show the intercept and flow diagrams for unit B2 to the Charlie Lake Formation.

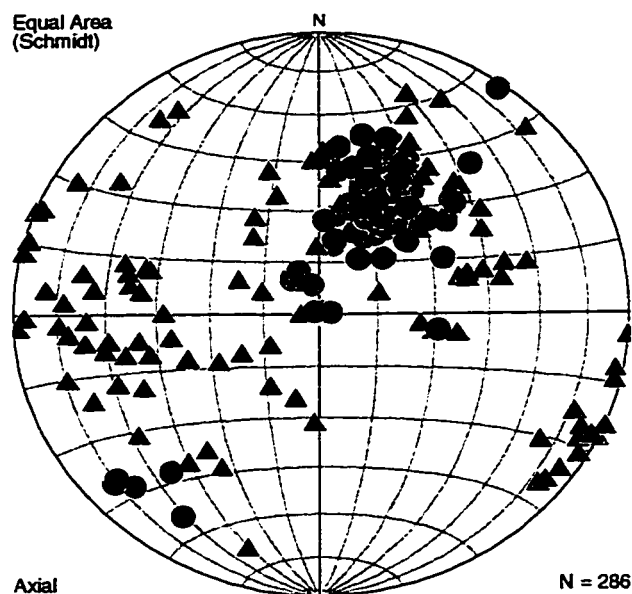
Well 7

Well 7 was drilled into a backlimb with beds dipping down towards the southwest. Bed dips increase from 30 degrees at the top of the Triassic to 45 degrees at a fault in the middle interval. Bed dips remain relatively constant below the fault at approximately 40 degrees.

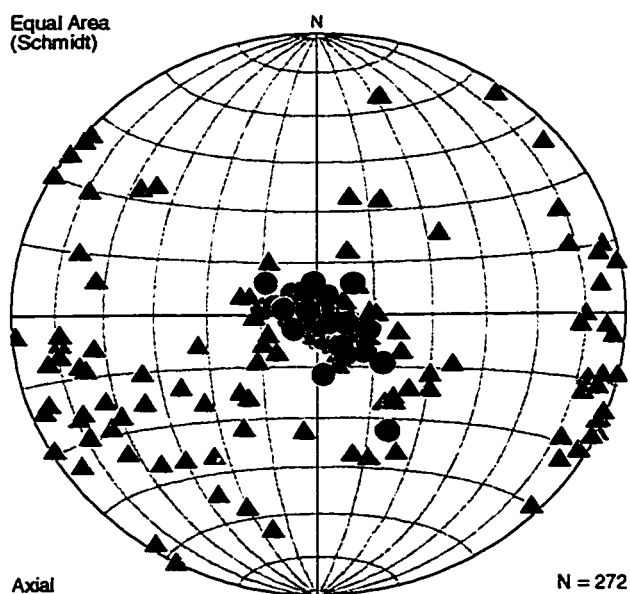
The structural analysis using the upper Triassic bedding poles gave an eigenvector fold axis with a plunge of 06 degrees at an azimuth of 123. The fractures are rotated using this fold axis as outlined in Chapter 2 by first removing the fold plunge followed by rotations of the dip domains. The resulting rotations are shown in Figure 3-31.

The well path in dip and strike views is shown in Figure 3-32. The well was drilled nearly vertically as it entered the Triassic, then decreased angle to approximately 45 degrees towards the NE. Relative to horizontal bedding, the well entered at a approximately 35 degrees to the SW and became nearly vertical through the middle and lower parts of the section.

The rotated fracture poles and planes are shown in Figures 3-33, a & b. Many of the fractures are at low angles, approximately 15 to 30 degrees, relative to the bedding planes. There are two clusters of more vertical fractures. The first cluster has poles in the SW quadrant and strike directions between 145 and 175. These are oriented like Type 2 shear fractures. The second cluster has poles in the SE and NW quadrant, giving a strike between 010 and 030 degrees. These fractures are oriented like Type 1 fractures.



a) bedding (circles) and fractures (triangles) before rotation



b) bedding (circles) and fractures (triangles) after rotation

Figure 3-31: Well 7 bedding and fracture data.

Stereonet projection of fracture and bedding poles before and after rotation.

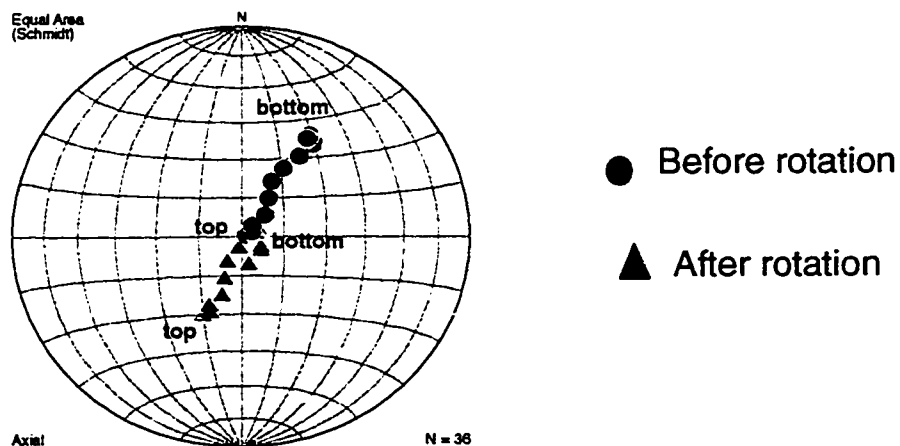
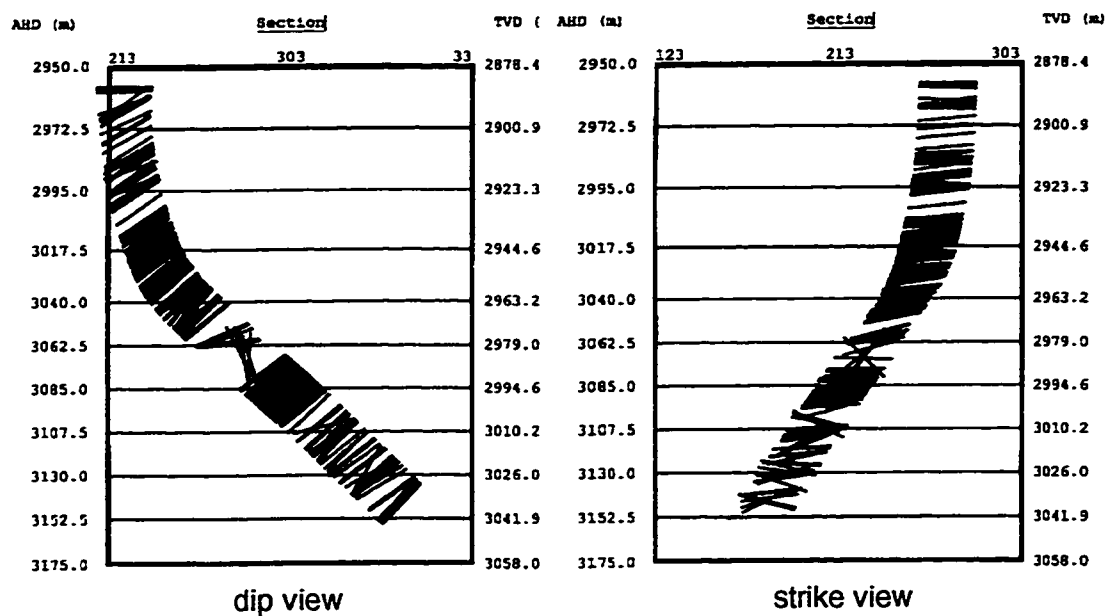
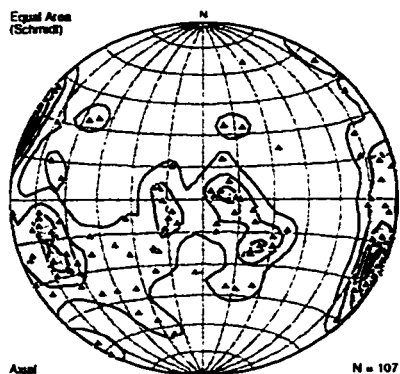
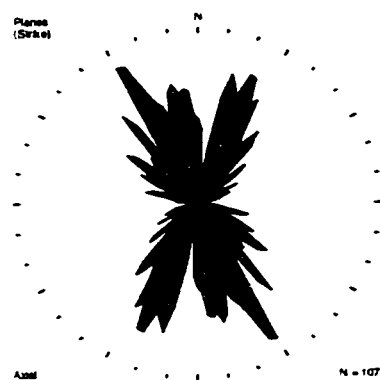


Figure 3-32: Well 7 well path.

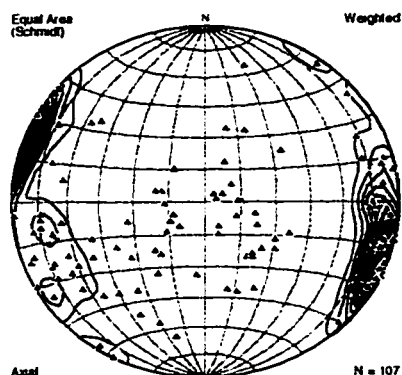
Well path is shown in dip and strike sections and in a stereonet projection of the well path before and after bedding rotation.



a) raw fracture poles



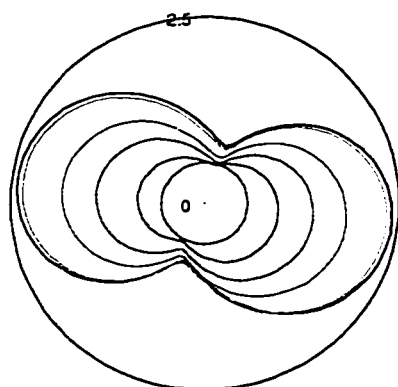
b) raw fracture planes



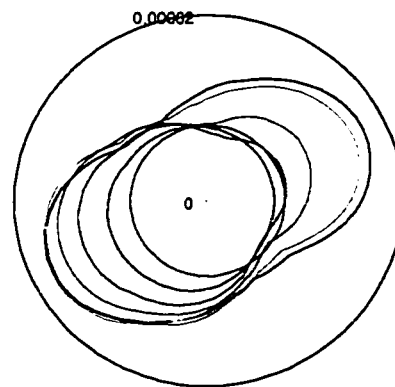
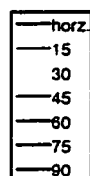
c) occurrence weighted contouring



d) occurrence weighted planes



e) fracture intercept diagram



f) fracture flow diagram

Figure 3-33: Well 6 occurrence correction, flow and intercept diagrams.

Rotated fracture poles and strike before and after occurrence correction are shown in figures a through d. Fracture intercept and flow rate diagrams for upper Triassic interval are shown in figures e and f.

The occurrence weighted contoured stereonet and rose diagram (Figures 3-33 c & d) heavily weights the Type 1 fractures. The frequency of the other fracture orientations is greatly reduced and relatively insignificant.

The fracture intercept and flow diagrams for the interval are shown in Figures 3-33, e&f. The predicted maximum intercept rates are in the ESE and WNW directions, with the east side maximum being slightly larger. The intercept rate is controlled by the heavily weighted Type 1 fractures. The predicted maximum flow intercepts are NE and SW, with the SW maximum being significantly larger than the NE maximum. The large aperture fractures, with poles in the SW quadrant (Figure 3-34, c&d), are controlling the predicted maximum flow direction.

The upper unit has the greatest fracture density with a maximum of nearly 5 fractures per meter (Figure 3-35). The middle unit has a maximum of nearly 2 fractures per meter and the lower has a maximum density of 2.5 fractures per meter. The lowest unit has the maximum fracture volume followed by the middle and upper unit. Unlike many of the other wells, the difference in fracture volume between units is not as large, with the fracture volume of the lower unit twice as large as the middle unit and 5 times as large as the upper unit.

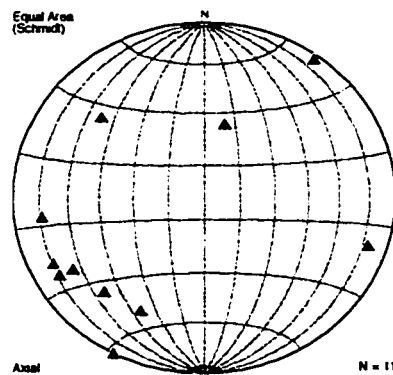
The orientation of the maximum intercept rate and flow rate changes between units and diagrams. In addition, many of the diagrams are asymmetric. This is most obvious in the lower unit intercept diagram and the upper and lower unit flow diagrams. Larger maxima are observed towards the SW direction.



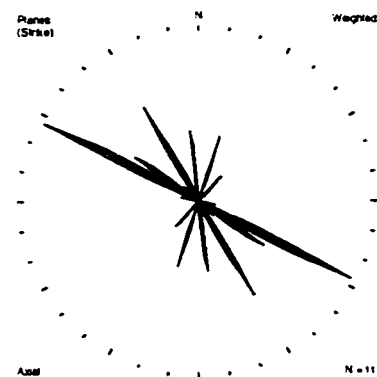
a) fracture aperture versus measured drilling depth (m)



b) fracture aperture versus fracture dip direction azimuth



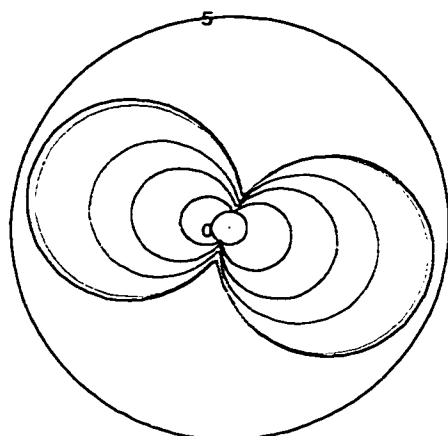
c) large aperture fracture poles on stereonet



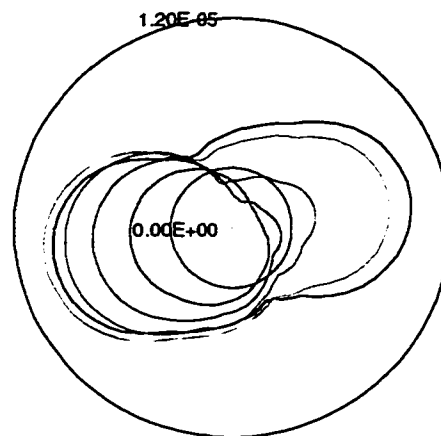
d) large aperture fracture strike direction on weighted rose diagram

Figure 3-34: Well 7 fracture aperture relationships.

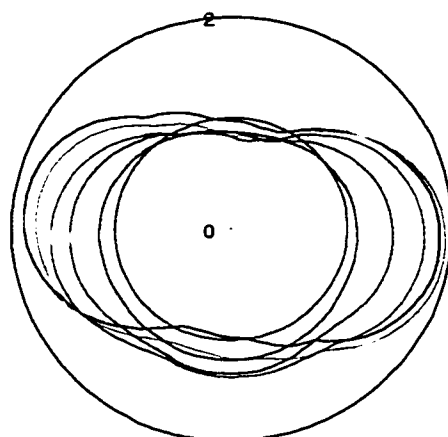
Fracture aperture relationships as a function of depth and azimuth (a and b). The 10% of fractures with the largest apertures are shown on stereonet and rose diagram (c and d).



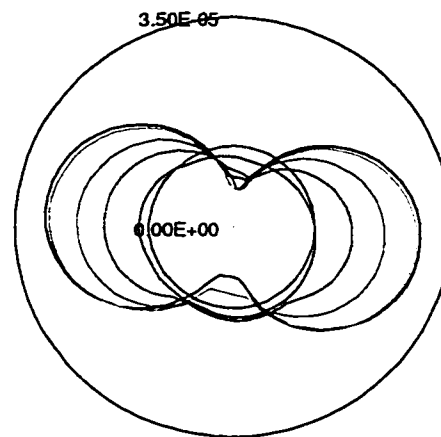
a-1) intercept diagram P4 to P2



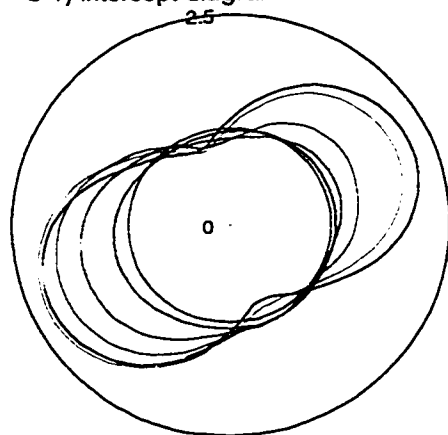
a-2) flow diagram P4 to P2



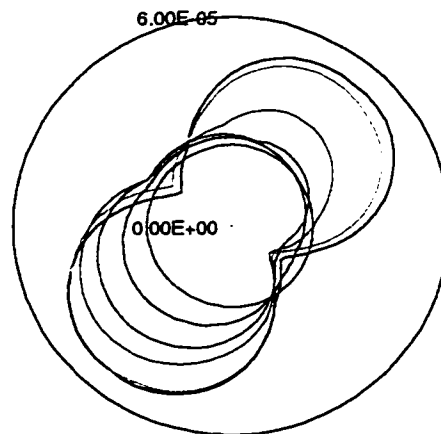
b-1) intercept diagram P2 to B2



b-2) flow diagram P2 to B2



c-1) intercept diagram B2 to lower B1



c-2) flow diagram B2 to lower B1

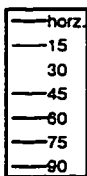


Figure 3-35: Well 7 flow and intercept diagrams by divided units.

The Pardonet and Baldonnel are divided into 3 intervals: a-1 and a-2 show the intercept and flow diagrams for units P4 to P2; b-1 and b-2 show the intercept and flow diagrams for units P2 to B2 and; c-1 and c-2 show the intercept and flow diagrams for unit B2 to the lower B1 unit.

Well 8

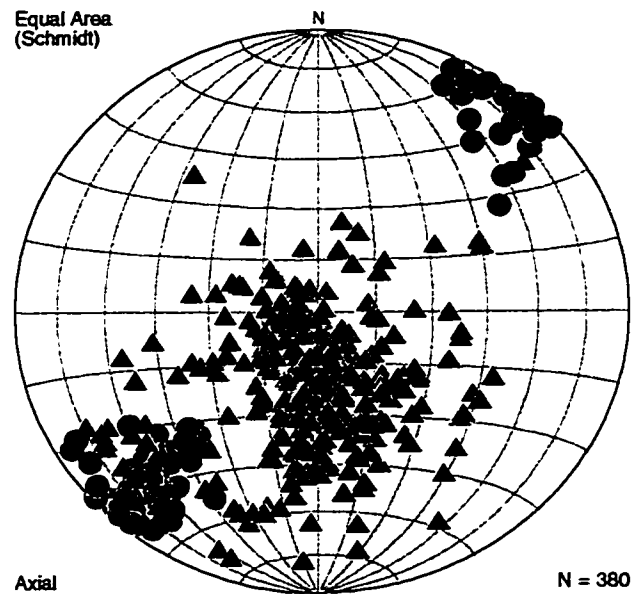
Well 8 was drilled into a steeply dipping forelimb. The beds are dipping at 50 degrees at the top of the unit and increase in dip towards the base. In the lower unit, the bedding is overturned. There are no large faults interpreted in the well.

The structural analysis using the upper Triassic bedding poles gives an eigenvector fold axis with a plunge of 01 degree at an azimuth of 133. The fractures are rotated using this fold axis as outlined in Chapter 2 by first removing the fold plunge followed by a rotation of the dip domains. The results of the rotations to the bedding and fracture poles are shown in Figure 3-36.

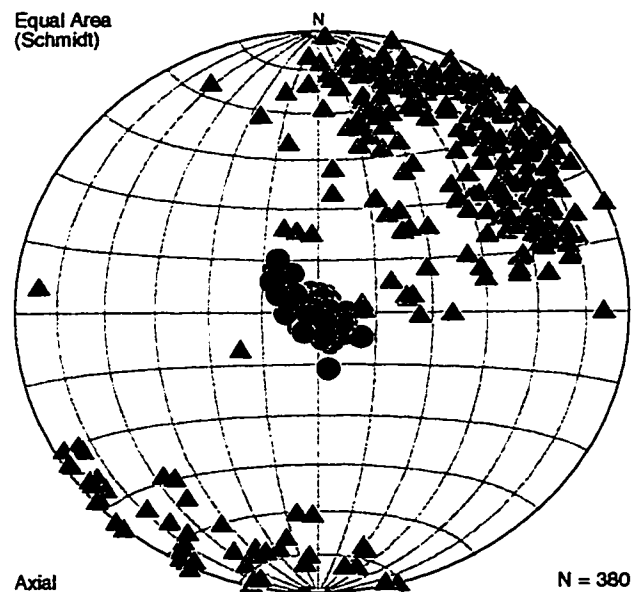
The well path in dip and strike views is shown in Figure 3-37. The well entered the Triassic close to vertical at 75 degrees west, then decreased in angle, to approximately 45 degrees towards the SW. The well was drilled to the NE at approximately 30 to bedding.

The rotated fracture poles and planes are shown in Figures 3-38, a & b. The fractures are at high angles to bedding with most of the fracture poles in the NE and SW quadrants of the stereonet. The strike of the fractures is between 100 and 150 degrees. The fractures fall into three groups. The three fracture groups are oriented as Type 2 fractures, with the extensional orientation in the middle (strike of 125) and both shear sets, approximately at 20 degrees on either side of the extensional set. The occurrence weighting (Figures 3-38, c & d) has little effect on the relative frequency and orientation of the fractures.

The fracture intercept and flow diagrams for the interval are shown in Figures 3-38, e&f. The predicted maxima for the intercept and flow rate are in the NE and SW



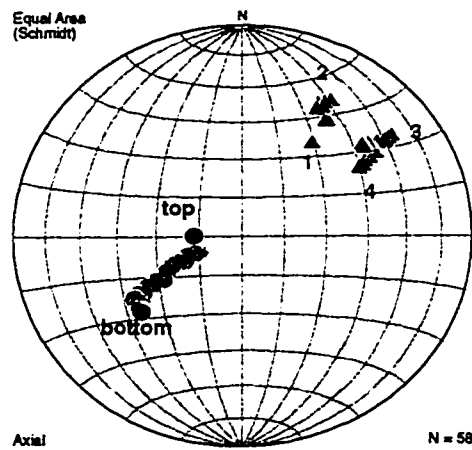
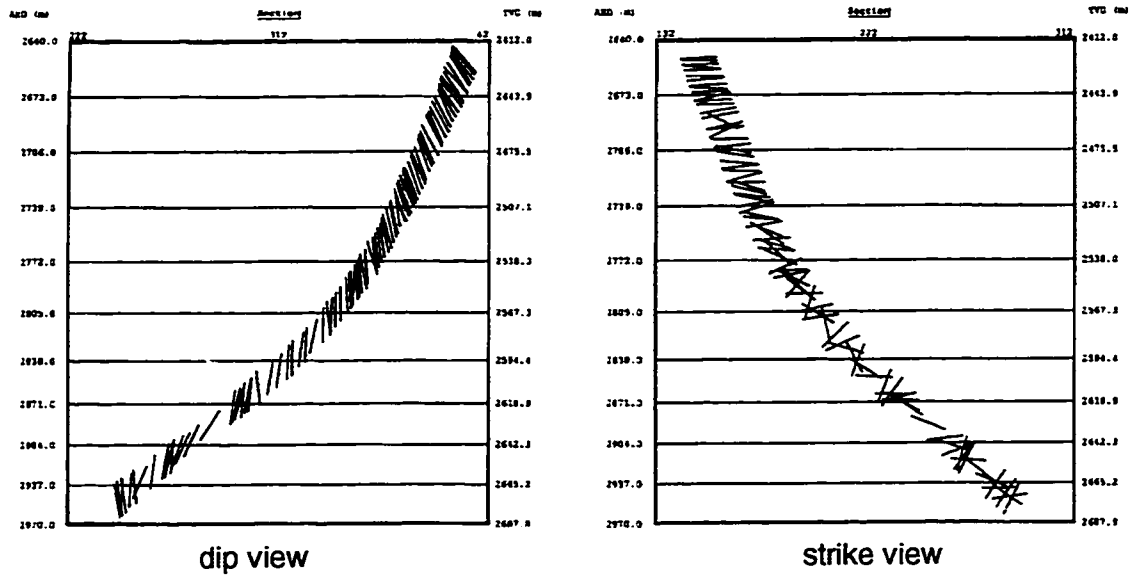
a) bedding (circles) and fractures (triangles) before rotation



b) bedding (circles) and fractures (triangles) after rotation

Figure 3-36: Well 8 bedding and fracture data.

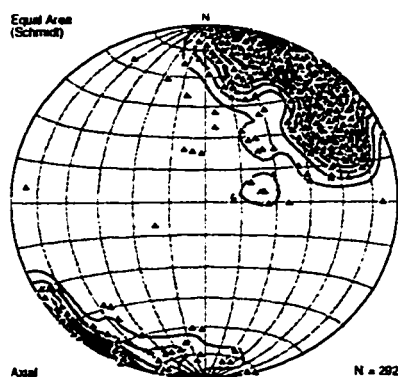
Stereonet projection of fracture and bedding poles before and after rotation.



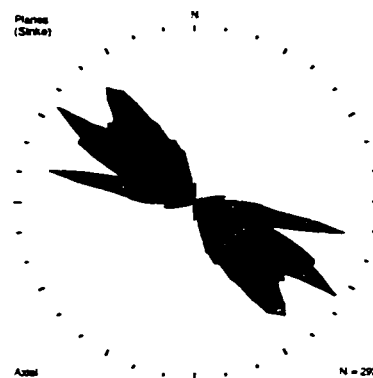
- Before rotation
- ▲ After rotation

Figure 3-37: Well 8 well path.

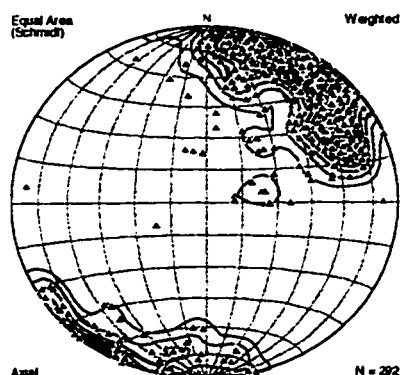
Well path is shown in dip and strike sections and in a stereonet projection of the well path before and after bedding rotation.



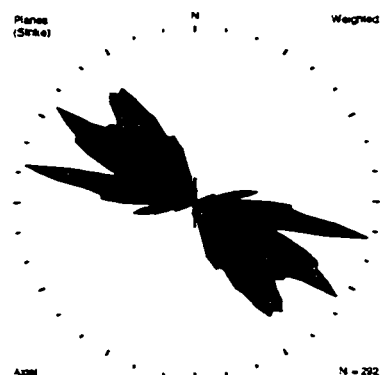
a) raw fracture poles



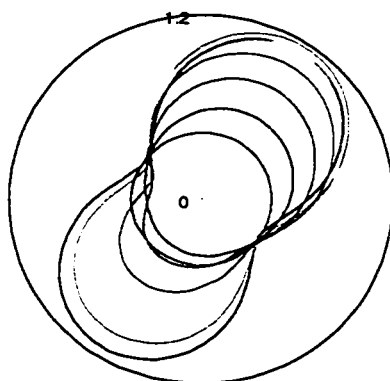
b) raw fracture planes



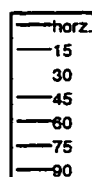
c) occurrence weighted contouring



d) occurrence weighted planes



e) fracture intercept diagram



f) fracture flow diagram

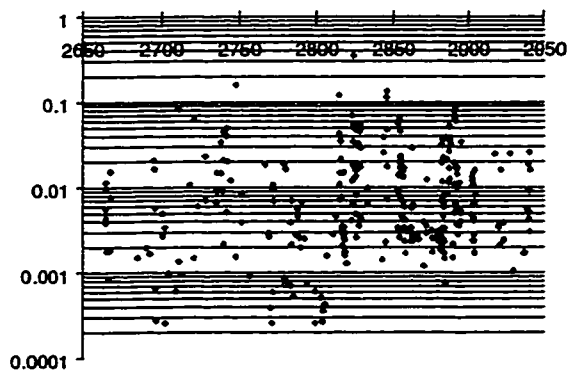
Figure 3-38: Well 8 occurrence correction, flow and intercept diagrams.

Rotated fracture poles and strikes before and after occurrence correction are shown in figures a through d. Fracture intercept and flow rate diagrams for upper Triassic interval are shown in figures e and f.

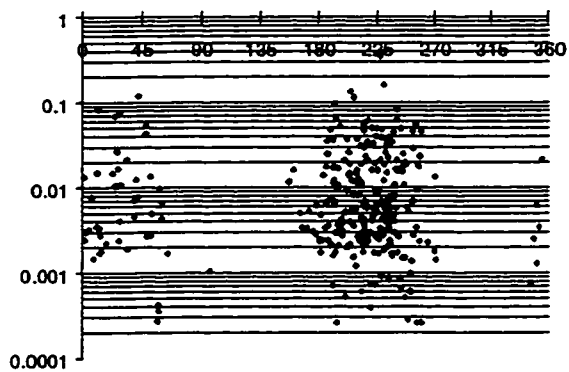
directions, with the east side maximum being significantly larger. The asymmetry towards the east side is due to the largest aperture fractures having poles in the NE quadrant (Figure 3-38 and 3-39).

The lower unit has the greatest fracture density with a maximum of 1.8 fractures per meter (Figure 3-40). The upper and the middle units have a maximum density of 0.3 fractures per meter. The lowest unit has the maximum fracture volume approximately one order of magnitude greater than the upper and middle units.

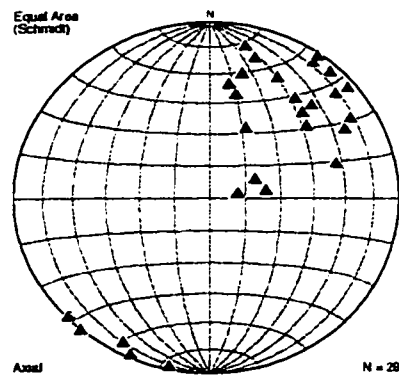
The orientation of the maximum intercept rate and flow rate is relatively constant between units (Figure 3-40). The asymmetry observed for the total unit is also apparent in the three units with greater maxima at all levels towards the NE.



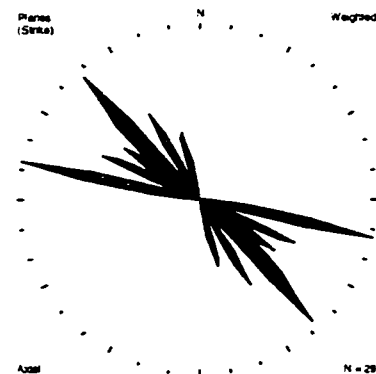
a) fracture aperture versus measured drilling depth (m)



b) fracture aperture versus fracture dip direction azimuth



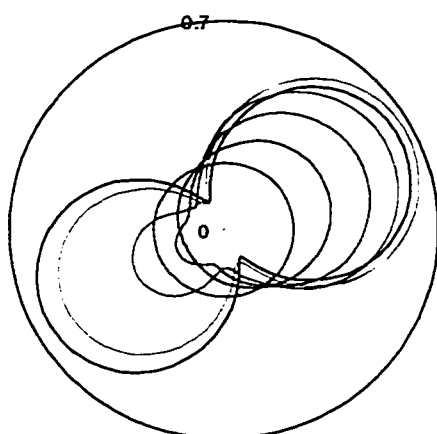
c) large aperture fracture poles on stereonet



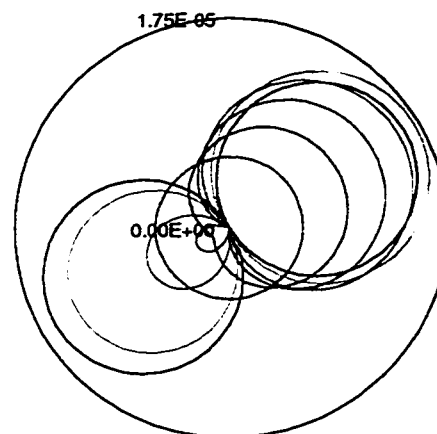
d) large aperture fracture strike direction on weighted rose diagram

Figure 3-39: Well 8 fracture aperture relationships.

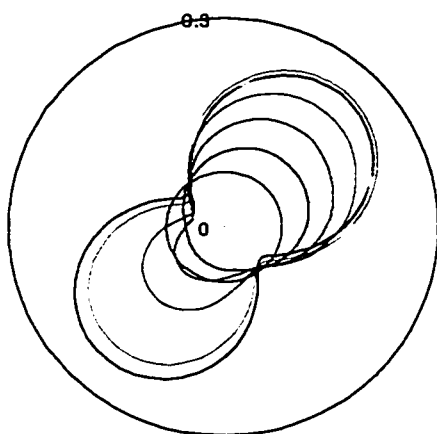
Fracture aperture relationships as a function of depth and azimuth (a and b). The 10% of fractures with the largest apertures are shown on stereonet and rose diagram (c and d).



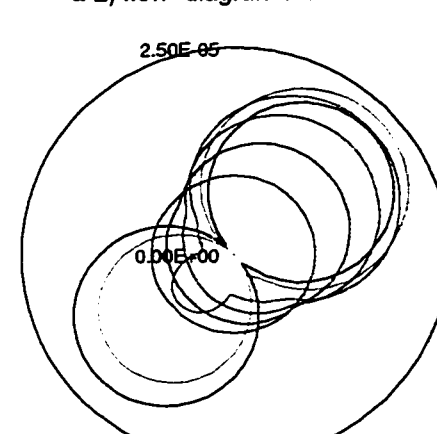
a-1) intercept diagram P4 to P2



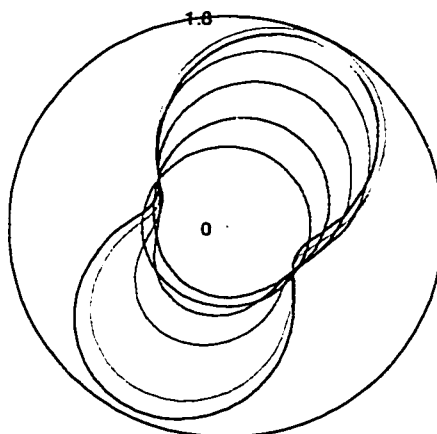
a-2) flow diagram P4 to P2



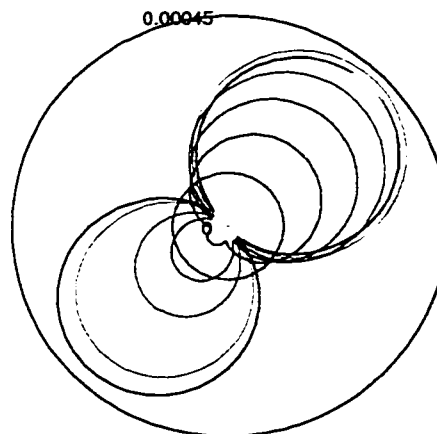
b-1) intercept diagram P2 to B2



b-2) flow diagram P2 to B2



c-1) intercept diagram B2 to CLLK



c-2) flow diagram B2 to CLLK

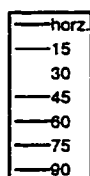


Figure 3-40: Well 8 flow and intercept diagrams by divided units.

The Pardonet and Baldonnel are divided into 3 intervals: a-1 and a-2 show the intercept and flow diagrams for units P4 to P2; b-1 and b-2 show the intercept and flow diagrams for units P2 to B2 and; c-1 and c-2 show the intercept and flow diagrams for unit B2 to the Charlie Lake Formation.

Well 9

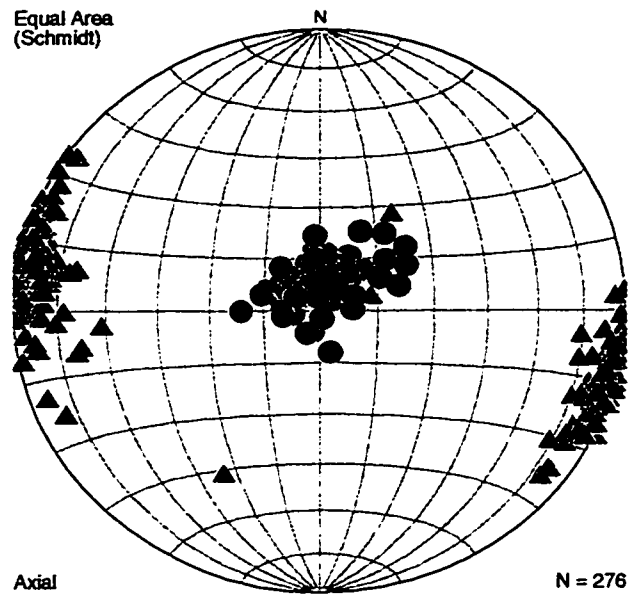
Well 9 was drilled just off the crest on the western flank of a fold. The beds dip gently to the SW at approximately 12 degrees. However, most of the bedding dip is due to the plunge of the fold. There are small areas of increased dip through the section that are likely due to small faults or folds. There are no major faults within the section.

The structural analysis using the upper Triassic bedding poles gives an eigenvector fold axis with a plunge of 08 degrees towards an azimuth of 153. The fractures are rotated using this fold axis as outlined in Chapter 2 by first removing the fold plunge followed by a rotation of the dip domains. The resulting rotations are shown in Figure 3-41.

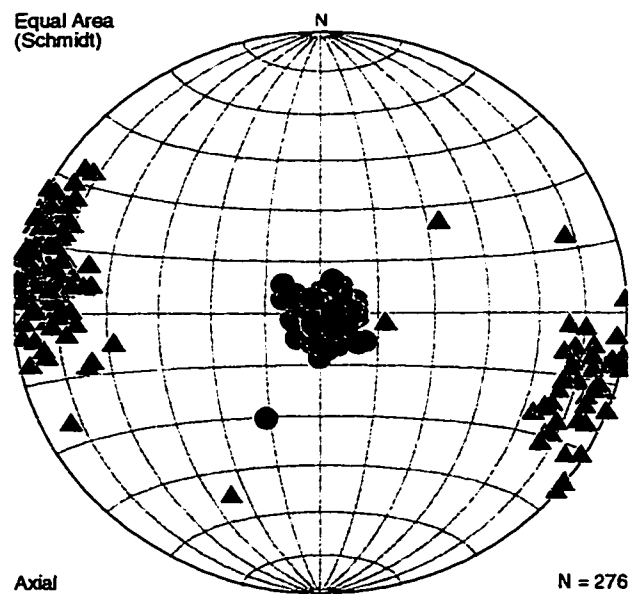
The well path in dip and strike views is shown in Figure 3-42. The well enters the Triassic inclined at 70 degrees and decreases angle toward horizontal through the section. The well ended in the lower B1 unit at approximately 15 degrees from horizontal. The well was drilled in the NW direction, nearly parallel to the trend of the fold axis.

The rotated fracture poles and planes are shown in Figures 3-43, a & b. Most of the fractures are at high angles relative to bedding with the majority of the fracture poles in the SE and NW quadrants. These fractures have a strike direction between 005 and 025 degrees. The applied occurrence weighting has little effect on the contoured stereonet and rose diagram (Figures 3-43 c & d).

The fracture intercept and flow diagrams for the interval are shown in Figures 3-43, e&f. Both diagrams have predicted maxima with orientations in the ESE and WNW directions. Both diagrams are asymmetric, with increased values on the west side. The



a) bedding (circles) and fractures (triangles) before rotation



b) bedding (circles) and fractures (triangles) after rotation

Figure 3-41: Well 9 bedding and fracture data.

Stereonet projection of fracture and bedding poles before and after rotation.

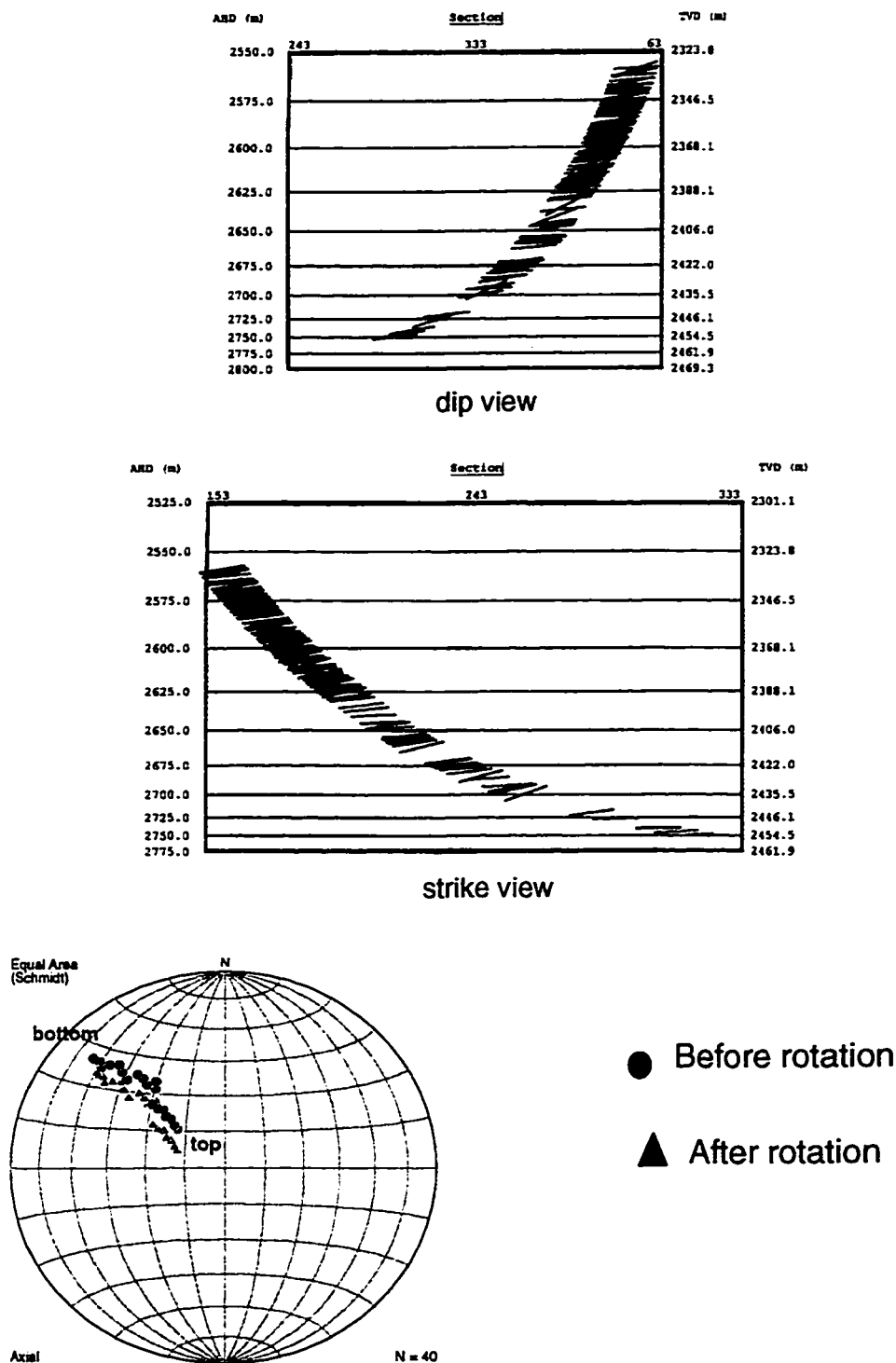
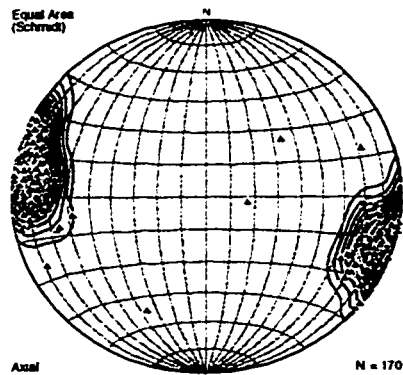


Figure 3-42: Well 9 well path.

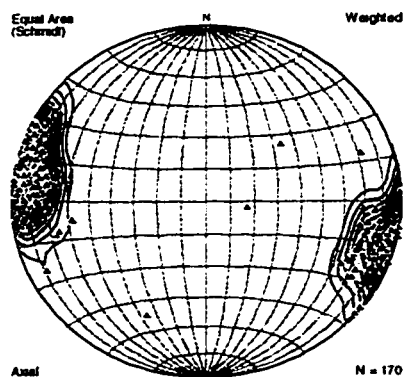
Well path is shown in dip and strike sections and in a stereonet projection of the well path before and after bedding rotation.



a) raw fracture poles



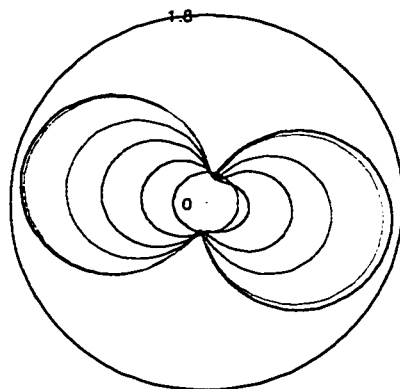
b) raw fracture planes



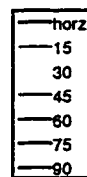
c) occurrence weighted contouring



d) occurrence weighted planes



e) fracture intercept diagram



f) fracture flow diagram

Figure 3-43: Well 9 occurrence correction, flow and intercept diagrams.

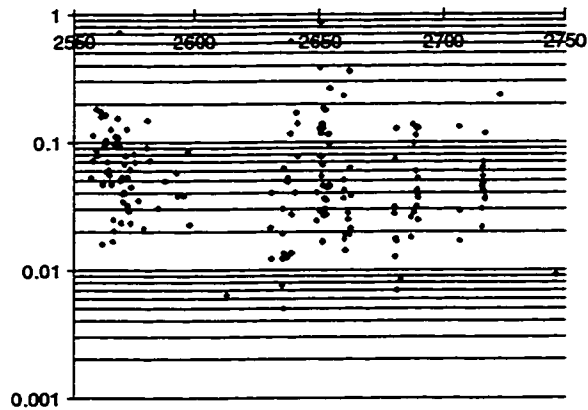
Rotated fracture poles and strikes before and after occurrence correction are shown in figures a through d. Fracture intercept and flow rate diagrams for upper Triassic interval are shown in figures e and f.

fracture and flow intercept rate increases as the sample direction changes inclination from vertical (90 degrees) to horizontal (0 degrees).

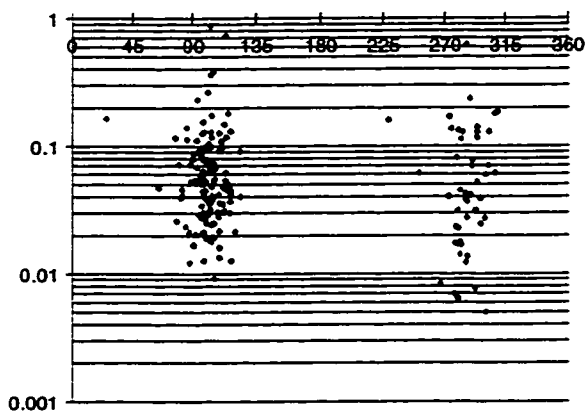
Figure 3-44 shows the fracture aperture relationships for the well. There is little to distinguish in these relationships because most of fractures have a similar orientation. However, two of the large aperture fractures (Figure 3-44, c&d) are uniquely oriented, striking SE/NW at lower angles to bedding (approximately 60 degrees).

The upper unit has the greatest fracture density with a maximum of 7 fractures per meter (Figure 3-45). The middle unit has a maximum of nearly 0.8 fractures per meter and the lower has a maximum density of 1.6 fractures per meter. The upper unit also has the greatest fracture volume per meter with the maximum approximately 3 times greater than in the lower interval and over two orders of magnitude greater than in the middle unit.

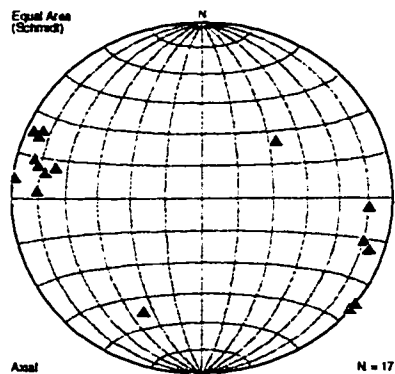
All intervals have a similar orientation for both predicted intercept and flow maxima towards the ESE/WNW. All the diagrams have an asymmetry with greater maxima on the west side.



a) fracture aperture versus measured drilling depth (m)



b) fracture aperture versus fracture dip direction azimuth



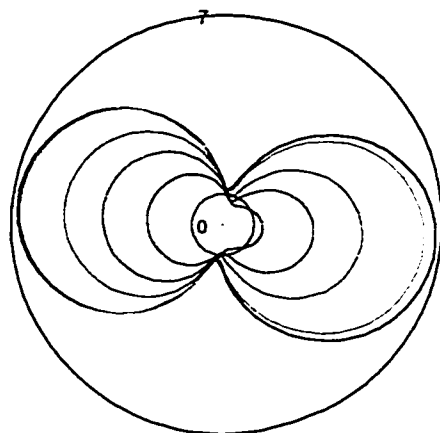
c) large aperture fracture poles on stereonet



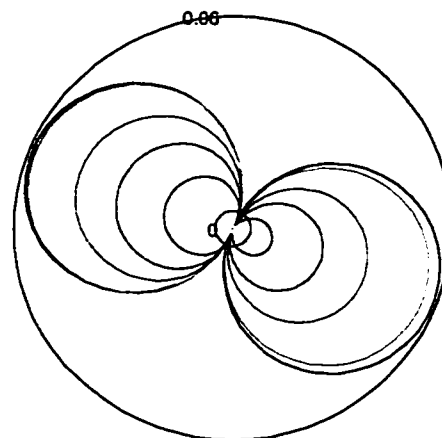
d) large aperture fracture strike direction on weighted rose diagram

Figure 3-44: Well 9 fracture aperture relationships.

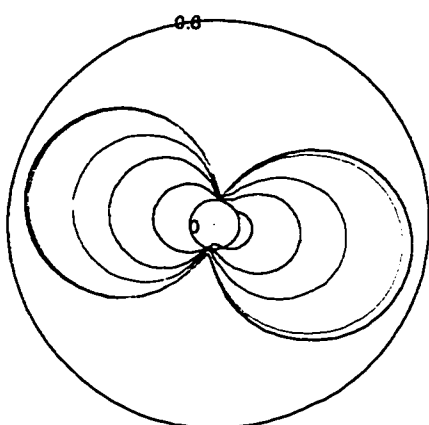
Fracture aperture relationships as a function of depth and azimuth (a and b). The 10% of fractures with the largest apertures are shown on stereonet and rose diagram (c and d).



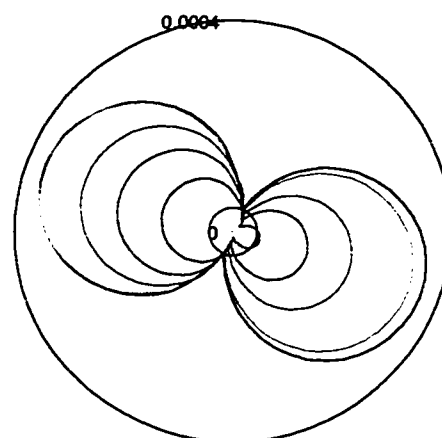
a-1) intercept diagram P4 to P2



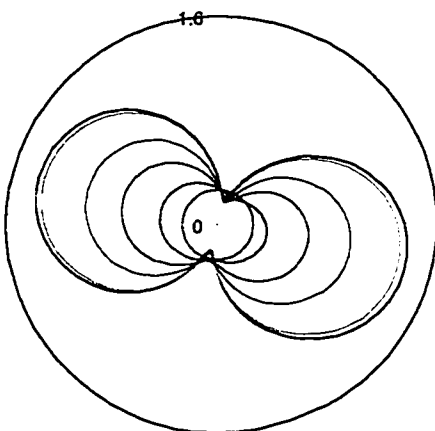
a-2) flow diagram P4 to P2



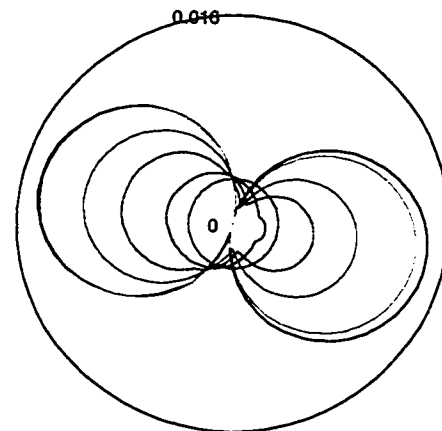
b-1) intercept diagram P2 to B2



b-2) flow diagram P2 to B2



c-1) intercept diagram B2 to lower B1



c-2) flow diagram B2 to lower B1

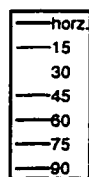


Figure 3-45: Well 9 flow and intercept diagrams by divided units.

The Pardonet and Baldonnel are divided into 3 intervals: a-1 and a-2 show the intercept and flow diagrams for units P4 to P2; b-1 and b-2 show the intercept and flow diagrams for units P2 to B2 and; c-1 and c-2 show the intercept and flow diagrams for unit B2 to the lower B1 unit.

Chapter 4

Discussion

Fracture Orientations

As shown in Chapter 3, most of the fractures are oriented at high angles to bedding and group into discrete sets after bedding is rotated to horizontal. This agrees with the many previous studies including Mueke and Charlesworth (1966), Burger and Thompson (1970), Norris (1971), Cooper (1991) and Jamison (1997). Hence, after rotation of the bedding to horizontal, the fractures are well represented by rose diagrams.

The rotated fracture orientations are represented by rose diagrams in Figure 4-1. The rose diagrams are occurrence corrected, attempting to remove the well sampling bias to better represent the true fracture orientations. The fracture orientations, after applying the occurrence correction, are more consistent when compared between wells. As Figure 4-1 shows, six of the nine wells (Wells, 2, 3, 4, 5, 7, and 9) have a common most frequent fracture orientation of NNE/SSW. The most frequent fracture orientation is also observed on the Well 1 rose diagram, however it is not the dominant orientation. For Wells 6 and 9, the most frequent fracture orientation is different from the other wells, and several fracture orientations are well developed.

The strike of the frequent set is between 000 and 030 degrees. For Wells 1, 2, 3, 5, and 7, the fracture orientations match a Stearns' Type 1 shear orientation. For Well 4 the orientation better matches a Type 2 shear orientation. The different fracture

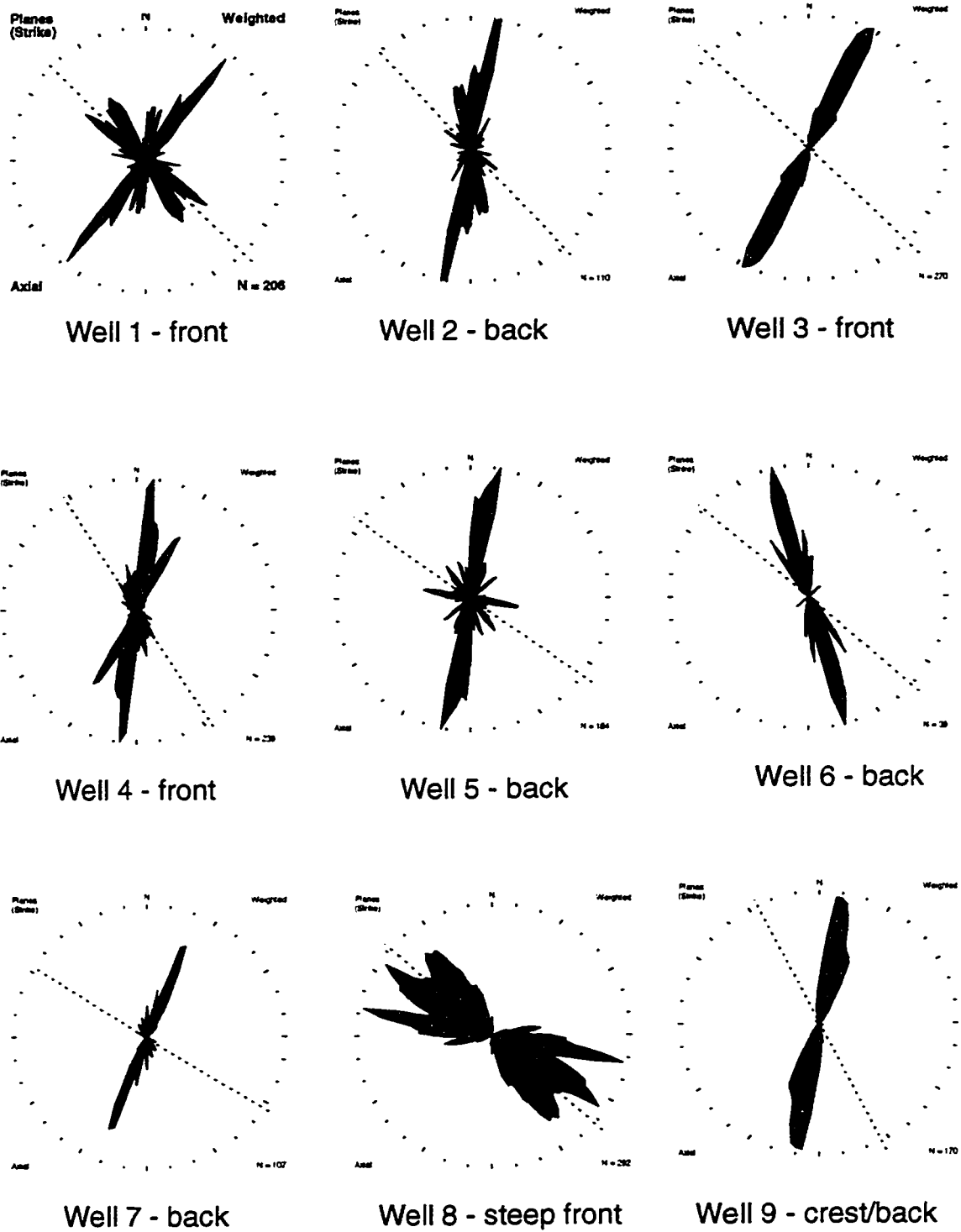


Figure 4-1: Occurrence weighted rose diagrams for all wells.

Rose diagrams show all occurrence weighted fracture strikes for the nine wells. Trends of rotated fold axes (structural strikes) are indicated by the dashed lines.

orientations in Wells 6, 8 and 9 may represent Type 2 shear and extensional fractures for different, local stress regimes.

Although the most frequent fracture orientation (NNE/SSW) can be made to fit Stearns' model, there are observations that question the applicability of the model to this set of fractures. Firstly, one would expect to see the other components of the Type 1 fracture set, namely the extensional and conjugate shear fractures. For Wells 1, 2 and 5 Type 1 extensional orientations are present, however they are much less frequent than the most frequent group. Secondly, the orientation of the most frequent set does not seem to systematically change orientation with changes in structural strike. For instance, Wells 2, 4 and 5 have structural strike directions of 135, 146 and 124 degrees, however, the frequent fracture set has virtually the same orientation in each well. Thirdly, in Wells 2 and 4, the most frequent fracture orientations appear to be parts of differently oriented conjugate sets. In Well 2, there are two additional peaks at 0 degrees and 345 degrees that combine with the most frequent set to form a set of conjugate shears and extensional fractures. For Well 4, the two peaks are oriented at 350 and 030 degrees. The change of regional strike by 10 degrees between the two wells would match a rotation of the conjugate set orientation.

Different models can be used to explain the formation of the frequent fracture set. First, these fractures could have formed prior to folding. For instance, they could have been pre-existing regional fractures or fractures related to basement structures. Then, through the folding process, deformation may have taken advantage of the pre-existing fracture fabric. This is the model McQuillan (1973) used to explain the fracture orientations in the Zagros Mountains in Iran. This is consistent with the observation

between Wells 2 and 4 that the conjugate set has rotated with changes in regional strike. Another model is that the fracture set formed during folding, however, pre-existing basement structures or some other factor could have caused transpressional deformation resulting in unusual fracture orientations or in the preferential development of one half of a conjugate set of shear fractures. Lastly, the fractures could post-date folding, with the fracture orientations resulting from some post folding extension or change in the stress orientation. This is consistent with the fracture orientations remaining constant even when the structural strike changes. However, if the fractures are formed post folding, then they should not divide into distinct sets, as they have, after rotation.

Well 6 also has a single dominant fracture orientation but it is to the NW instead of to the NE. Well 6 is the only well with the fold axis plunging to the NW instead of to the SE. The direction of the plunging fold axis could correlate to the dominant fracture orientation. However, without examining more wells in NW plunging folds, it is difficult to say if a correlation between plunge direction and fracture orientation is likely.

The dominant fracture orientations observed in Well 8 are unique. The orientations in this well are most like Type 2 fractures. However, if the three peaks represent a complete set of Type 2 conjugate shears and extension fractures, then their orientation is slightly oblique compared to Stearns' Type 2 fractures (the extensional set is approximately 7 degrees off the strike orientation). The angle between the extensional and shear orientations are approximately 20 degrees apart, which matches the Stearns' fracture model.

Well 8, of all the wells, is the best oriented to intersect Type 2 fractures. This direction also minimizes the chance of intersecting Type 1 fractures. This could explain why, even with the occurrence weighting applied, Well 8 did not intersect the frequent fracture orientation observed in the other wells. The occurrence weighting will only correct the fracture frequency distribution if it at least some of all the fracture orientations are sampled.

Fracture Aperture

Figure 4-2 shows the fracture aperture distribution for each well. The y axis is the fracture aperture measured in millimeters on a logarithmic scale. The x axis is the rank order, from largest to smallest fracture aperture, of each fracture in that well. The median ranked value is placed at 147 so that all the fracture sets have a common median point on the graph.

The variation in apertures displayed on the graph is very large within and between wells. Well 4 shows the greatest aperture variation with the smallest apertures around 0.0001 mm and large apertures over 2 mm. The variation between wells, for the same rank number, can also be several orders of magnitude.

The graphs are linear over the middle range of the rank order. Hence, the aperture distribution in the middle range fits a log/normal distribution. The slope of the line for all wells is also very similar except for Well 6. Hence the shape of the distributions is similar between wells. However, the median aperture value is different for the wells. Wells 2, 3, 4 and 9 have a similar median value and Wells 1, 5, 7 and 8 have different values. Wells 3, 4, 2 and 8 have graphs that extend over the largest range of middle ranked apertures. These wells also have the largest fracture apertures.

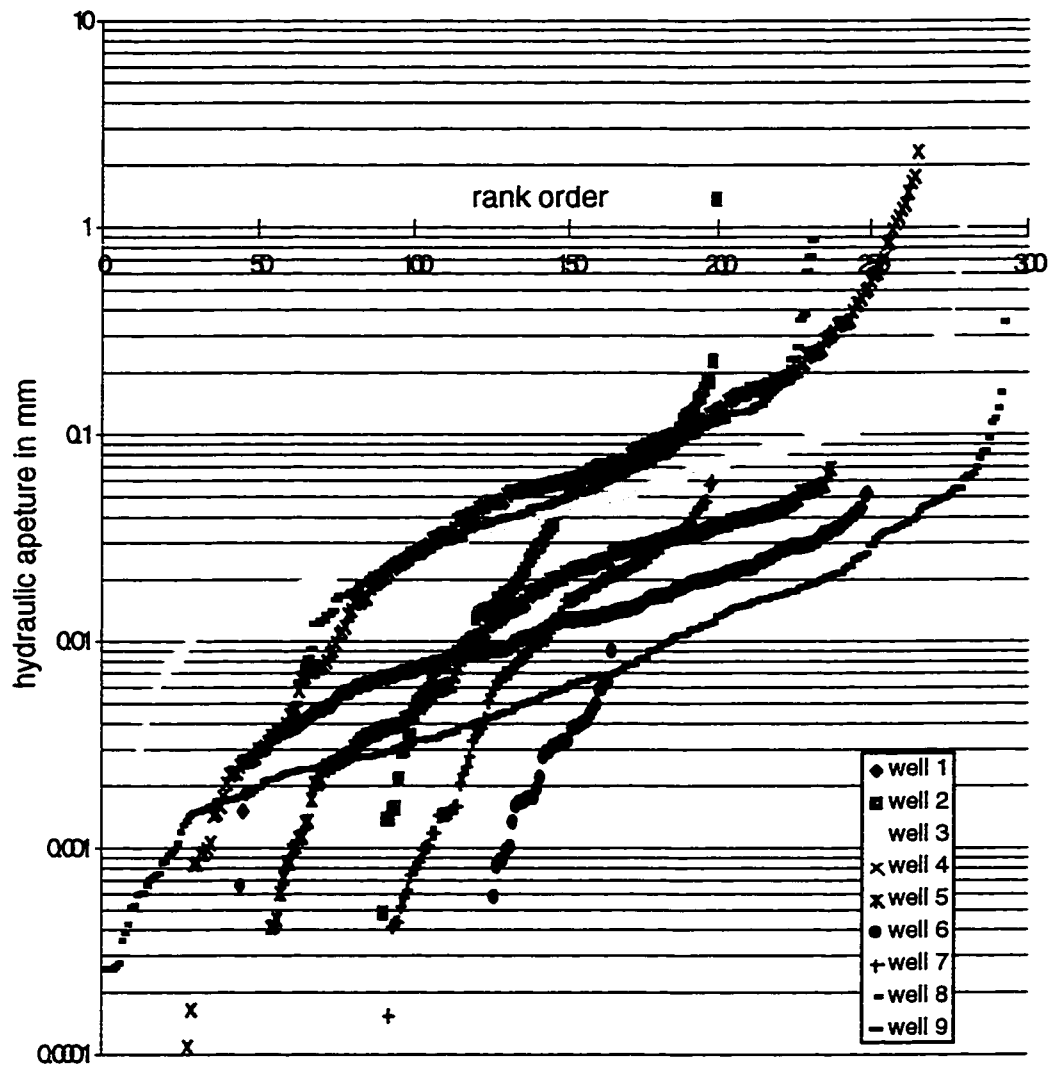


Figure 4-2: Fracture aperture distribution for each well.

The graph shows the aperture distribution for the nine wells. The x axis is the rank order, from smallest to largest fracture aperture, of each fracture in that well. The middle ranked fracture, for each well, is centered on rank number 147.

At either end of the linear portions of graphs in the middle range, there is a break in the slope for many of the wells. For both large and small aperture fractures the slope increases, meaning that there is greater aperture change between rank ordered fractures. However, the slope is similar between wells at the end ranges. Wells 1 and 5 do not exhibit this break for larger aperture values, however they do for smaller aperture values. The slope of Well 6 for all aperture values fits the end range slopes observed in the other wells.

The difference between median values in Figure 4-2 can be interpreted two ways. The first interpretation is that the shift between the curves is a true measurement of differences in aperture volume between the wells and should not be adjusted. A second interpretation is that the shift is due to a systematic error in the aperture measurement. The prime candidate for the error would be the mud resistivity value that is used to calculate the aperture. This is a constant value within the well but differs between wells. If an error in the mud resistivity is causing the aperture shift between the wells, a correction can be applied to better align the aperture values. One way to apply the correction is to shift the median value of each distribution to a common aperture value. For instance, the curve for Well 8 could be shifted up approximately one order of magnitude and would closely match the distribution of apertures for Well 3.

The bulk shift technique described above will not be examined in this study. However, if applied, it would result in a very different view of the fracture volume relationships that will be discussed in the next section. Instead we will assume the fracture aperture volume differences between wells is real, since bulk shifting cannot superimpose all nine data sets on top of each other.

The 10% largest aperture fractures for all wells are shown in Figure 4-3. The large fractures group into two sets. The most frequent set has a Type 2 fracture orientation (330-340 degrees). The second frequent set has a strike of 010-030 degrees and would match the frequent set for all apertures discussed earlier.

There are also some low angle fractures that have a large aperture (Figure 4-3). Well 3 has a group of low angle fractures at approximately 30 degrees to bedding with poles in the SW quadrant. These fractures have orientations similar to the thrust faulting orientations in this area (strikes of 120 to 170 degrees) and could be related to the faulting observed in Well 3.

The large aperture fractures striking 010-030 degrees are primarily from Wells 3 and 9. However, in both of these wells, there were no Type 2 fracture orientations. In wells with both the Type 2 and the most frequent NE/SW set, (Wells 1, 2, 4, 5 and 7), the large aperture fractures are far more commonly Type 2 fractures. Therefore, the frequency of large fracture apertures oriented in the NE/SW orientation is likely overestimated. If Wells 3 and 9 were removed from the data set, the large aperture fractures are almost entirely Type 2 fractures striking 120-170 degrees.

Extensional strain in Type 2 fractures is predicted by kinematic finite-element modeling as discussed in Chapter 1 (Erickson and Jamison, 1995). Open fractures are expected in areas of curvature like the crest and outer arc of a hinge zone. The aperture data collected from these wells supports this prediction that most open, extensional fractures have Type 2 orientations. In the next section we will examine the fracture relationships to structural position to see if the areas of largest curvature have the greatest fracture intensity and volume.

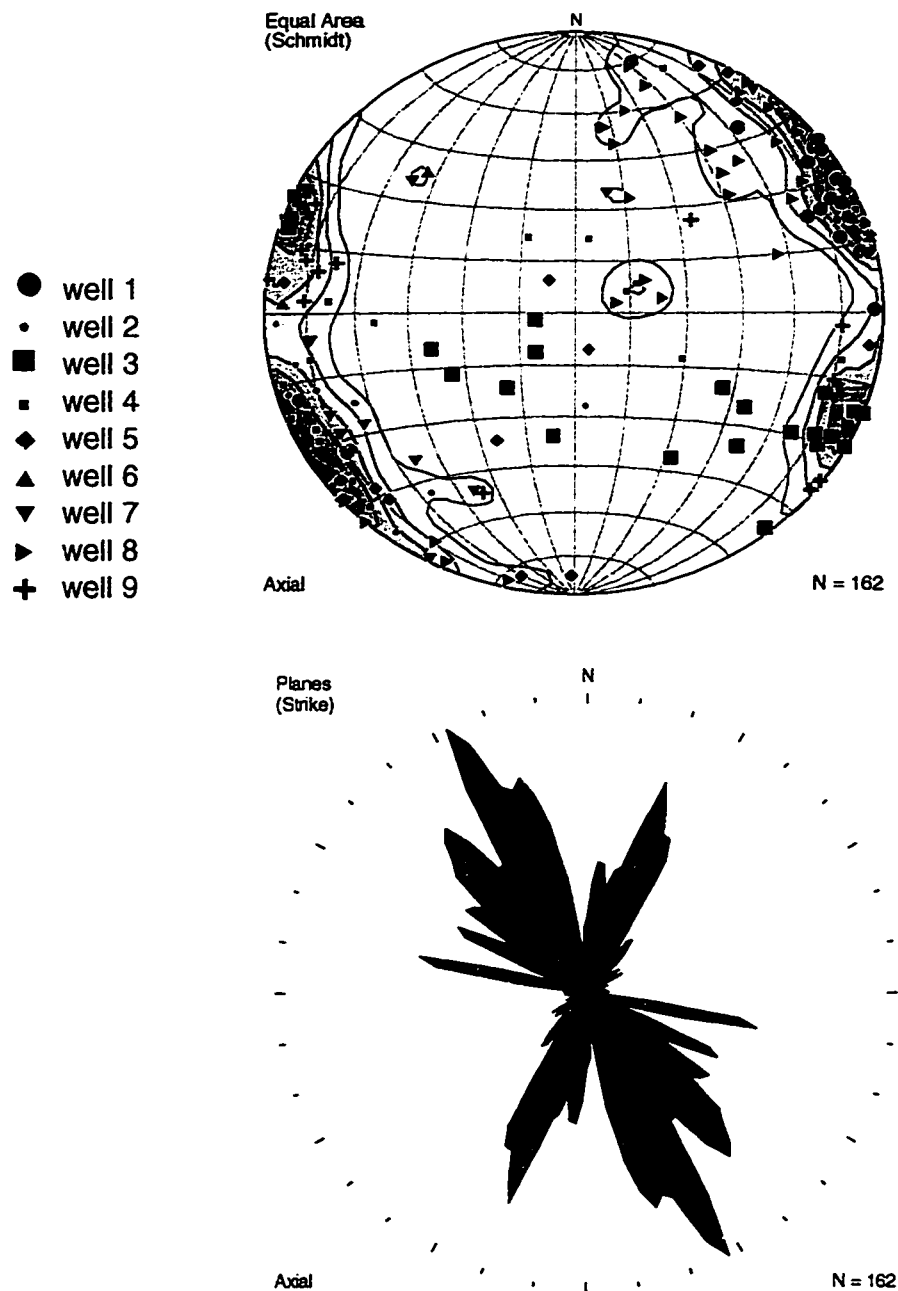


Figure 4-3: Orientations of large aperture fractures.

The stereonet and rose diagram show the poles and strikes for the largest 10% aperture fractures from each well.

Structural Position versus Fracture Density and Volume

Fracture Density

Figure 4-4 shows a conceptual composite fold model with vertical profiles in the dip direction for each well. The wells are placed in their relative structural positions on the forelimb, crest or backlimb of the composite fold. For example, Wells 8 and 1 are both on a forelimb, but Well 8 is positioned further forward because the bedding in Well 8 is more steeply dipping than in Well 1. The model is conceptual because the wells were drilled into different structures separated by many kilometers. The model does not attempt to represent the true structure away from the well. For example, Well 8 may actually be closer to the crest than Well 1.

Above each well is the fracture intercept diagram for the entire Pardonet and Baldonnel sequence. The diagrams are scaled to represent the relative fracture densities in each well. For example, the diagram above Well 3 has a maximum fracture density of 4.6 fractures/meter and is nine times larger than the maximum for Well 6 of 0.5 fractures/meter.

The orientation for the predicted maximum fracture intercept rate is similar for Wells 1, 2, 4, 5, and 7 with the maxima in the east and west directions. For these wells, the direction is determined by the large number of fractures striking NNE/SSW and the few fractures striking NW/SE. The remaining wells, 3, 6, and 8, have a single fracture orientation, resulting in a different orientation of the intercept diagram.

The two smallest diagrams are for Wells 6 and 4. These were the only two wells that were interpreted using FMS instead of FMI data. The FMS tool has less well bore coverage, making it more difficult to interpret subtle fractures. It is likely that the FMS

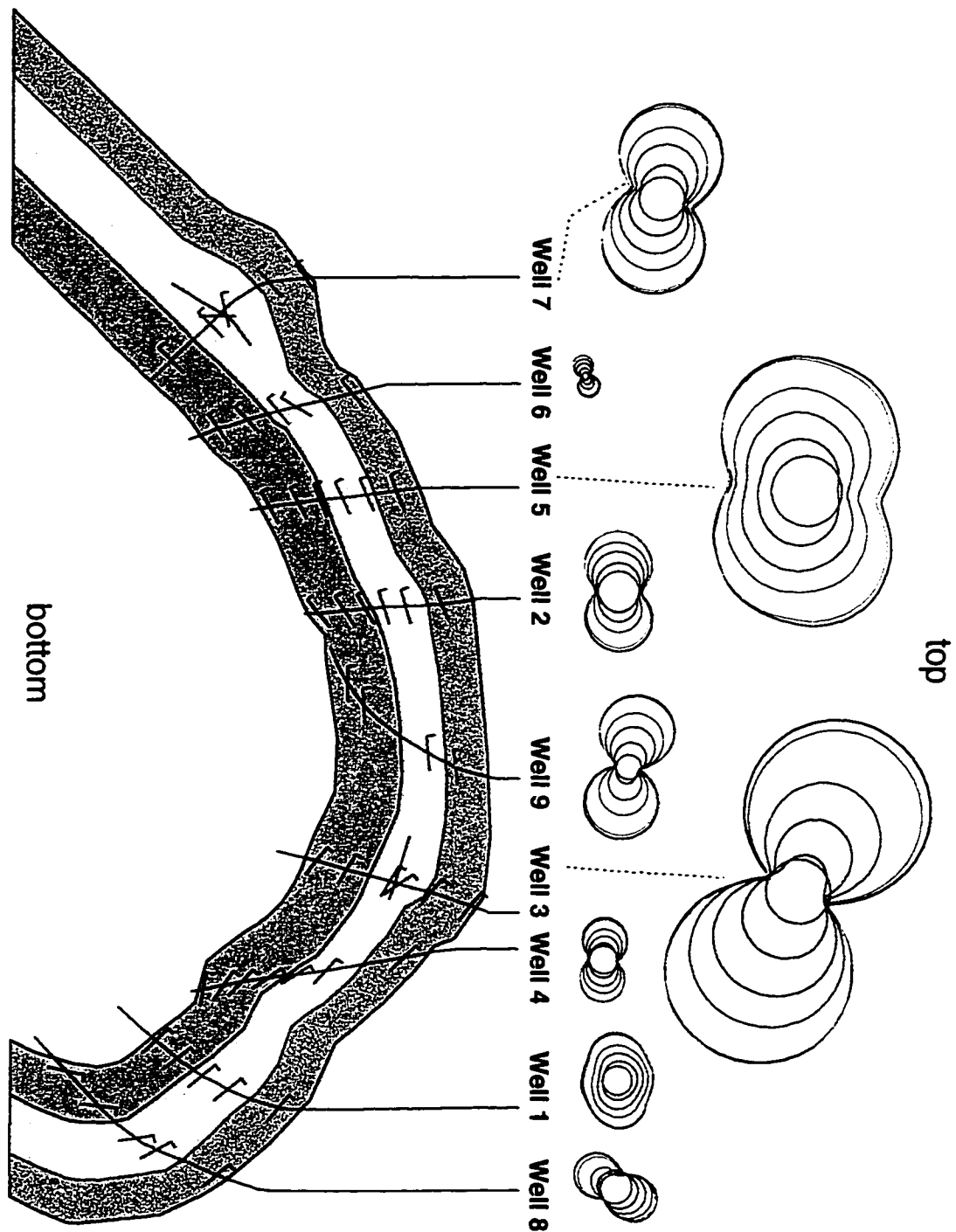


Figure 4-4: Structural position versus fracture density.

The figure shows a conceptual fold placing the nine wells in their relative structural positions. The size of fracture intercept diagram for each well is scaled to show the relative differences in fracture density.

tool will underestimate fractures relative to the FMI tool. As a result, the low fracture density in these wells may be due to the tool used rather than a measure of true differences in fracture density.

The two largest diagrams correspond to Well 3 and Well 5. Well 3 was drilled into a 30 degree dipping forelimb with a fault in the middle zone. Well 5 was drilled into a gently dipping backlimb, with dips increasing from 15 degrees to 30 degrees. It is unexpected that these wells, especially Well 5, that are in moderately dipping positions, with little bedding curvature, represent the most fractured zones.

The dense fracturing in Well 3 could be due to the faulting in the middle interval. Well 7, with the third largest fracture density, is also faulted, but has approximately half the fracture density of Well 3. Well 5, however, is not interpreted to be significantly faulted.

Greater fracture intensity has been associated with areas of steep plunge (McQuillian 1974 and Narr 1991). Well 3 has the steepest plunge of the wells at 13 degrees. Well 5, on the other hand, has zero plunge and defies the idea that the fracture density is easily correlated to fold plunge.

Other correlations to fracture density cited in Chapter 1 are not supported by the data in this study. Norris (1971) related fracture intensity to bedding rotation. Wells 8, 4 and 1 are the most rotated but they do not have unusually high fracture densities. McQuillan (1974) observed greater fracture densities in the crestal zone. Well 9 is on the crest but has only an average fracture density. Wells in the hinge zone or in areas of curvature are commonly thought of as being areas of the most intense fracturing (Narr 1991; Nelson and Serra 1995). In this study wells in hinge zones or areas of maximum

curvature are Wells 8, 4, 2 and 6. All of these wells have average to below average fracture densities.

The differences in fracture density in this study compare to Jamison's (1997) observations on the Monkshood Anticline in three ways. Firstly, the two densely fractured zones are on nearly planar dipping limbs in both the backlimb and forelimb positions. Secondly, fracture density does not correlate with bedding curvature or faulting. Lastly, in general, there is no obvious difference in fracture density between the front or back limbs.

The differences in fracture densities observed in this thesis as compared to other studies (Norris 1971; McQuillan 1974; Narr 1991 and; Nelson and Serra 1995) are not surprising considering that these observations are empirical and do not necessarily relate to the fundamentals of folding. Empirical observations from other studies could work as a predictive tool in precisely their respective settings but fold mechanics involve many variables and such simple models are not likely to be good predictive tools.

Fracture Volume

Figure 4-5 shows the conceptual structural fold model with the fracture flow diagrams for each well. The relative size of the flow diagrams has a logarithmic scale. Hence, the variation in size is a relative measure of the difference in order of magnitude of the maximum value of fracture volume for each well.

The orientations of the predicted maximum fracture volume are similar for Wells 1, 4, 5, 6, 7 and 8. For many of these wells the orientation has rotated away from the maximum fracture density to intercept fractures with greater aperture. Because these fractures tend to be Type 2 fractures, the flow diagrams are skewed towards the normal

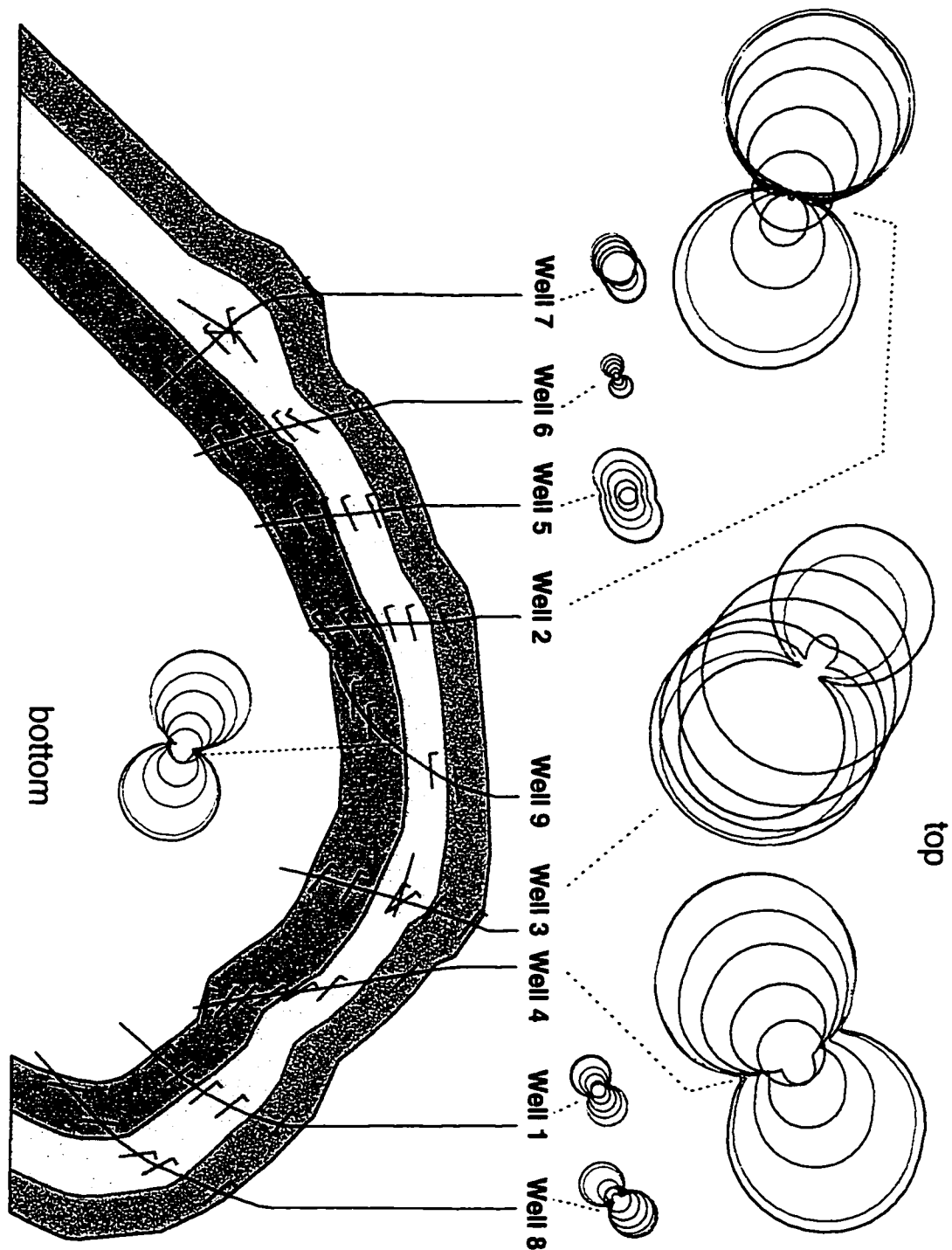


Figure 4-5: Structural position versus open fracture volume.

The figure shows a conceptual fold placing the nine wells in their relative structural positions. The size of the fracture flow diagram for each well is logarithmically scaled to show the relative differences in fracture volume.

of the Type 2 orientation. Wells 3 and 9 have a single set of fractures, not in the Type 2 direction, resulting with predicted maximum volumes in a similar orientation to their maximums densities. Well 2, having large aperture Type 2 fractures, has a predicted maximum volume to the SE/NW. The direction in Well 2 is determined more by the occurrence weighting and by the number of fractures than by the few large aperture Type 2 fractures.

Wells 3 and 5 have the largest associated fracture densities, but Wells 2, 3, 4 and 9 have the largest fracture volumes. Hence, fracture density does not necessarily correlate to fracture volume. As fracture volume is more important for gas flow, it could be wrong to drill for areas of high fracture densities.

On first appearance, the maximum fracture volume seems to correlate with areas near the structural crest. Wells 2, 3, and 9 are all in moderately dipping zones that should be near a crestal region. However, there are three other considerations. Firstly, Well 4, in the upper region, has dips similar to parts of Wells 1 and 8. However, these wells have considerably lower fracture volumes. Secondly, as stated earlier, the conceptual fold model does not represent the structure away from the well. So, for example, Wells 1 and 8 may be nearer to a structural crest than Well 3. Lastly, there is some doubt that fracture volumes should even be compared between wells. Aguilera (1995) states that aperture measurements between wells did not correlate to production differences in the wells. Error in aperture determination is compounded when calculating fracture volume because the fracture aperture is cubed in the volume calculation.

With the data discussed above, a single optimal structural position for high fracture intensity and volume cannot be strongly recommended. However, the data do suggest

that faulted zones, crestal areas and steep plunges, may all contribute to greater fracture density and volume.

Vertical Changes in Fracture Volumes and Densities

Figure 4-6 shows the relationship between fracture density and volume for the three units, P4 to P2, P2 to B2 and B2 to the Charlie Lake Formation, or the total depth of the well if the well was not drilled deeply enough to penetrate the Charlie Lake Formation. The upper graph, Figure 4-6a, shows the fracture density, by well, as measured from the predicted maxima on the intercept diagrams for each unit. The lower graph, Figure 4-6b, shows predicted maximum volume, by well, as measured from the maxima on the flow intercept diagrams for each unit. The y axis (Figure 4-6b) is a logarithmic scale, measured in units of millimeters cubed per meter drilled.

The most densely fracture zone, in seven of the wells, is the upper unit. In Wells 3, 5 and 9, the upper unit is significantly more fractured than the lower units. The greatest difference is in Well 5, where the upper unit has a fracture density of 12 fractures/m and the lower unit has a density of 4 fractures/m. In Wells 1, 4, 6 and 7 the upper unit is more fractured but the differences are much smaller.

In Wells 2 and 8 the lower unit is most densely fractured. The greatest difference is in Well 2 where the lower unit has a fracture density of 13.4 fractures/m and the upper unit has a density of 3.0 fractures/m. This is the greatest fracture difference of any of the units measured within the wells.

In six of the wells, the middle unit is the least densely fractured unit. In the other three wells, the middle unit is the second most densely fractured interval. The middle unit is never the most densely fractured interval.

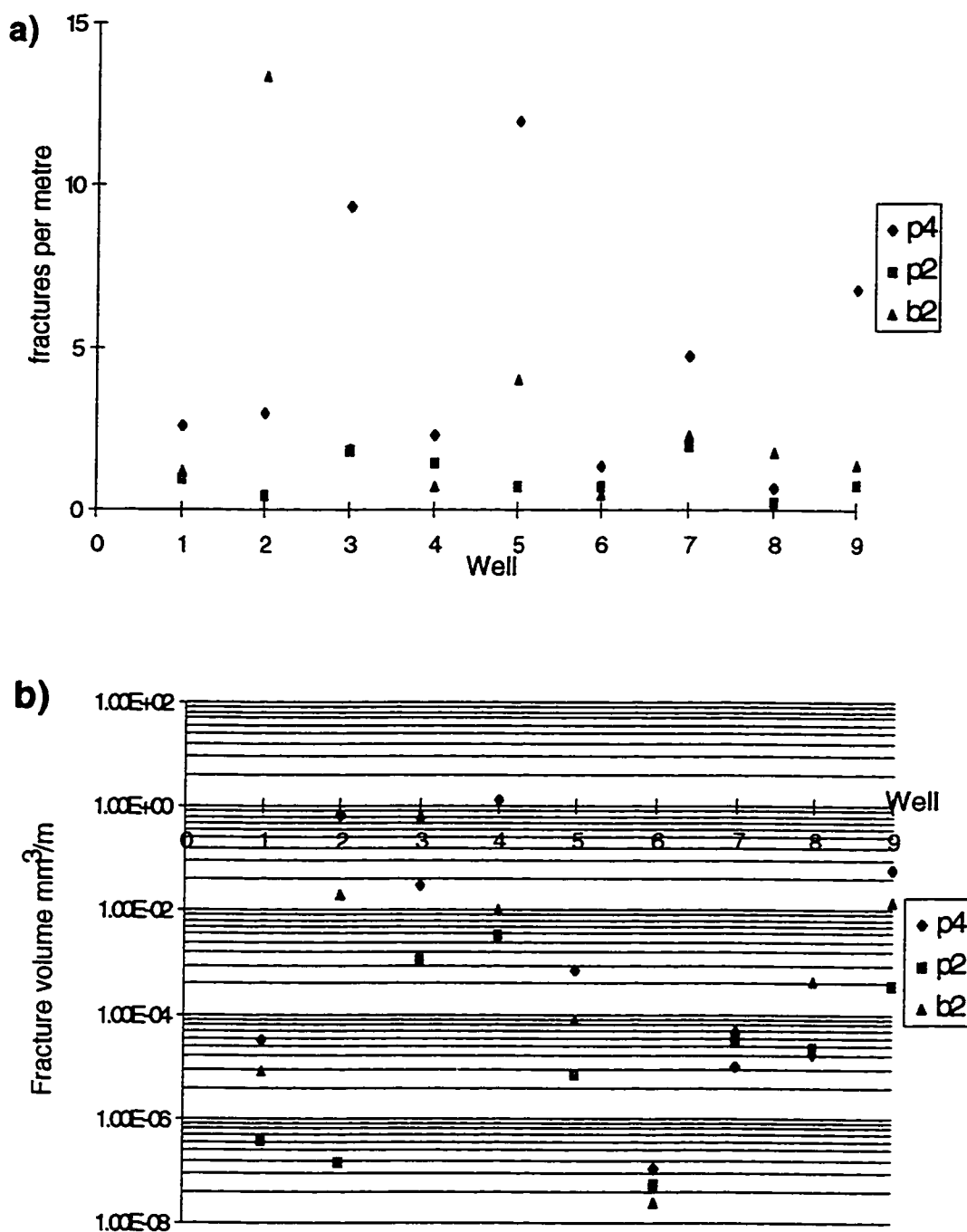


Figure 4-6: Fracture density and volume versus lithology.

Figure (a) shows the maximum fracture density, measured off the intercept diagram, for each of the three intervals in each well. Figure (b) shows the maximum fracture volume, measured off the flow diagram, on a log scale, for the three intervals in each well.

In six of the wells (Wells 1, 2, 4, 5, 6 and 9), the greatest fracture volume is in the upper unit. Well 2, which has a significantly greater fracture density in the lower unit, still has a higher fracture volume in the upper unit. Conversely, Wells 3 and 7 which had greater fracture density in the upper zone, have greater fracture volumes in the lower zone. Well 8 had maximum fracture densities and volumes in the lower unit.

Cooper's (1991) FMS interpretation of fracture density in a single well in NEBC is consistent with the observations made here. In Cooper's (1991) study, he found the upper unit to be the most fractured and fracturing decreased in the lower units. Cooper concluded that the changes in fracture density could be due to either changes in lithology or due to structural position.

The data presented in this thesis also lead to two possible conclusions for the observed fracture patterns at different positions in the well. One possibility is that the fracture density and volume, commonly greatest in the upper interval, are related to lithology. The upper unit is largely dolomitized, with only small intervals that have reservoir quality porosity. Dolomitized rocks with low porosity are observed to be intensely fractured rocks, (Nelson, 1985). The middle unit is less dolomitized, with more sandstone, silt and limestone. These rocks are observed to be less fractured than tight dolomites (Stearns and Friedman, 1972; Nelson, 1985). The lower unit is the most dolomitized and porous interval. The dolomitic lithology of the lower unit should result in more fracturing than the middle unit. But, because the lower unit is more porous than the upper unit, it should be less fractured than the upper unit.

The second possibility for the variations in fracture patterns with well depth is explained by structural relationships. In the crestal area, in the upper units, above the

neutral surface (Ramsay, 1967), the tensile strain will result in higher open fracture densities. Deeper in the fold, at the neutral surface, less fracturing will occur. Below the neutral surface, in the zone of compressive strain, there could be a high density of fractures associated with faulting, but the fractures will be less open.

The fold and strain concepts defined above are consistent with the patterns observed in the Wells 1, 4, 5, 6 and 9. Additionally, structural relationships could be used to explain some of the anomalous well data. Well 2 has the greatest fracture density in the lowest unit, which could be due to the lower unit hinge zone. In the hinge zone, the dips and curvature are increasing, like the extensional area at the top of a fold, and extensional strain would be expected. Additionally, Well 8, with both increased fracture density and volume in lower unit, has greater curvature in the lower zone. Well 7, with greater fracture volume in the lower unit, could be explained because it is on the flank of a syncline, where compressive strain is above the neutral surface and extension is below the surface.

The vertical changes in fracture volumes and densities could be due to either lithology, structural position or, most likely, some combination of the two effects. Nelson and Serra (1995) found both lithology and structural position do influence fracturing. On the fold limbs, lithology was the main control on fracture density. In areas of high curvature the fracture densities became more homogeneous in all lithologies. Nelson and Serra's (1995) observations are consistent with the data presented in this thesis.

The lithologic and structural influences on fracturing from in this thesis are inconclusive. In general, however, the upper unit is the most densely fractured zone with the greatest fracture volume. The lower unit is usually the second most fractured

interval with the second greatest fractured volume. The middle unit is the most poorly fractured zone, with the least fracture volume.

The vertical changes in fracture volume would suggest that drilling the upper unit will provide the optimum fracture volume and best production results. However, the best reservoir rocks are in the lower unit. Therefore, the fractures in the upper unit must be well connected with the lower unit to act as a gas flow conduit. This conduit relationship is complicated by the fact that the middle interval is the most poorly fractured zone. Limited spinner data, not shown in this study, in some of these wells do show large volumes of gas flowing from the upper unit even in non-reservoir rocks. The spinners were run during production tests. Hence it is inconclusive that these upper zones will flow gas over the production life of the pool.

Optimal Drilling Direction

As defined earlier, optimal drilling direction for this thesis is defined as the drilling direction that will encounter the greatest fracture volume per meter drilled (Nolen-Hoeksema and Howard, 1987). The optimal direction is defined in terms of drilling inclination and azimuth. The directions are given relative to bedding and not absolute drilling orientations.

Figure 4-7 shows the optimal direction from the analysis of the nine wells. The upper Figure, 4-7a, is the maximum flow value in each well as a function of drilling inclination angle relative to horizontal bedding. The x-axis is inclination angle measured from horizontal (0 degrees) to vertical (90 degrees). The y-axis gives the percent of the maximum fracture volume encountered in each well.

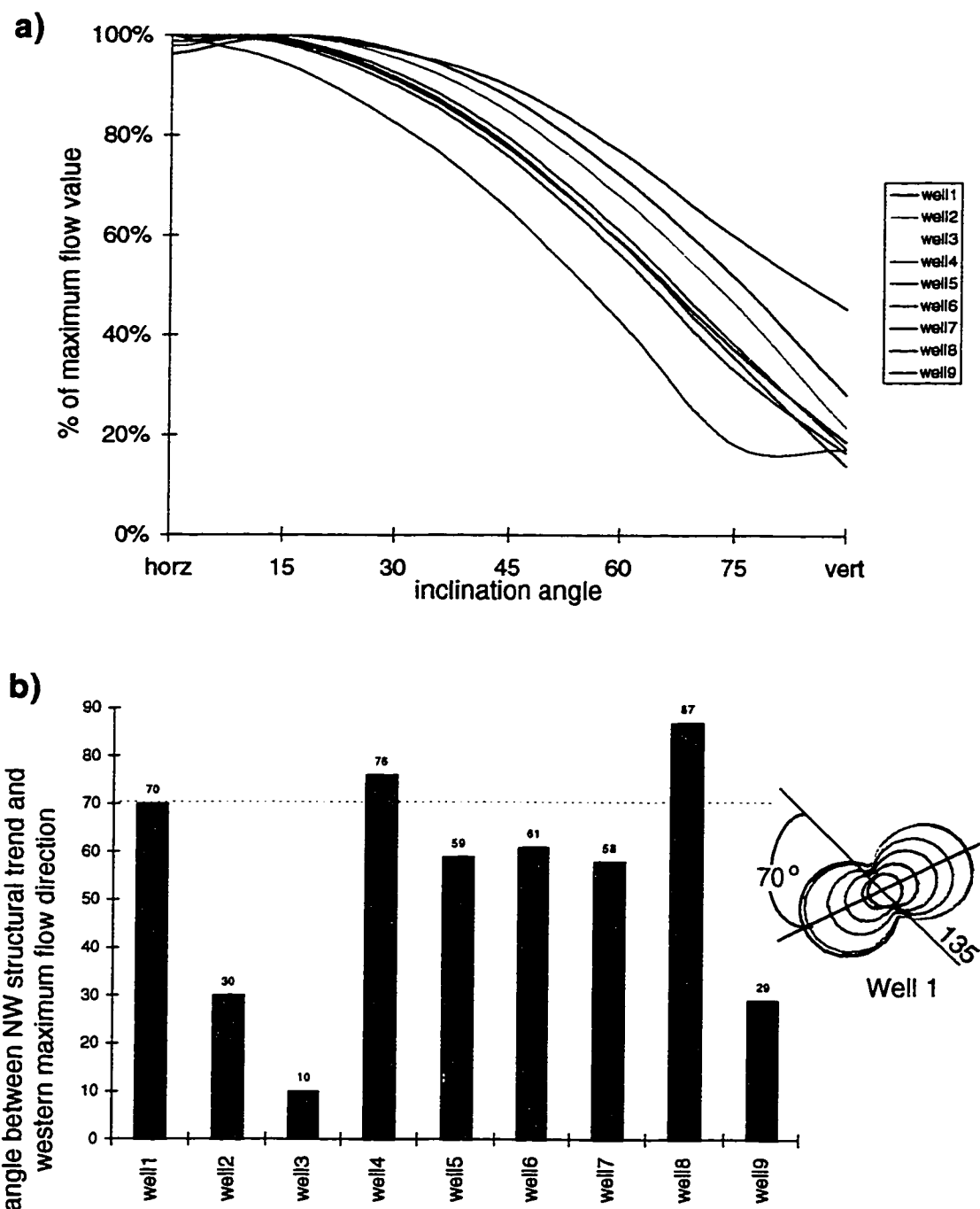


Figure 4-7: Optimum drilling inclination and azimuth.

Figure (a) shows the % of the maximum flow value for each inclination relative to the maximum flow value in the well. Figure (b) shows the horizontal angle between the NW structural trend direction and the western azimuth of the predicted maximum flow value (as shown in the inset for Well 1).

Drilling horizontally (parallel to bedding) is optimal or near optimal for all wells except Well 3. Drilling vertically will reduce the fracture volume per meter drilled by as much as 80%, down to 20%. The curves are not linear, having increasing slope above 30 degrees. As a result, there is little advantage to drilling horizontally compared to drilling at a 30 degree inclination. However, there are major changes in flow volume for inclinations ranging from 30 degrees to 60 degrees and from 60 degrees to vertical.

Well 3 has an optimal drilling inclination closer to 30 degrees from horizontal. The unusual optimal inclination observed in Well 3 is due to the large aperture fractures that are at lower angles to bedding (Figure 3-14). As previously discussed, these fractures are likely associated with the faulting observed in Well 3.

Figure 4-7b shows the optimal drilling azimuth for each well. The graph measures the angle between the NW structural trend direction and a “western azimuth” of the predicted maximum flow value (as shown in the inset diagram in 4-7b). If the absolute predicted maximum value has an eastern azimuth, 180 degrees are added to the eastern azimuth to get the “western azimuth”. Typically maxima in the eastern directions, especially at near horizontal drilling inclinations, are closely matched to the maxima in the western direction.

Wells 1, 4, 5, 6, 7 and 8 have similar optimal azimuths, all within 17 degrees of the 70 degrees average of these wells. For these wells, the optimal azimuth is determined by two factors. First, and most importantly, the large fractures have Type 2 orientations and the optimal drilling direction is nearly perpendicular to strike to intersect these fractures. The second factor is the large number of fractures in the NNW/SSE orientation. Although these fractures typically have smaller apertures, they are more

abundant. The NNW/SSE fractures skew the optimal azimuth clockwise from being perpendicular to strike.

In Wells 3 and 9, Type 2 fractures are not present. The optimal azimuth in these wells is determined by the single set of NNE/SSW fractures. In Well 2, both fracture sets are present. However, the optimal azimuth is more influenced by the larger aperture NNE/SSW fractures.

Optimal Drilling Direction Recommendation

Using the two criteria discussed above, and ignoring the anomalous wells, there is enough consistency between wells that an optimal direction can be recommended. Maximum fracture volume per meter will be encountered with a well inclined 0 to 30 degrees relative to bedding, at a bearing measured 70 degrees counterclockwise from the regional structural strike. With this drilling bearing and inclination, the upper unit, on average, will have the greatest fracture volume, the middle unit the least and the lower unit an intermediate fracture volume. Fracture volume may increase in the crestal area or areas of structural complications, such as faulting or steep plunge.

A Comparison of the Nine Wells to the Optimal Drilling Direction

Figure 4-8 is an equal area lower hemisphere stereonet projection of the well survey points. The red lines highlight the optimal drilling direction as defined in the previous section. The two curved red lines represent small circles 30 degrees from horizontal. The optimal azimuth, measured 70 degrees counterclockwise from the regional structural trend in the wells is shown by the straight red line, oriented NE/SW (43/223). The curved red lines are centered at the average optimal azimuth. The curved blue lines

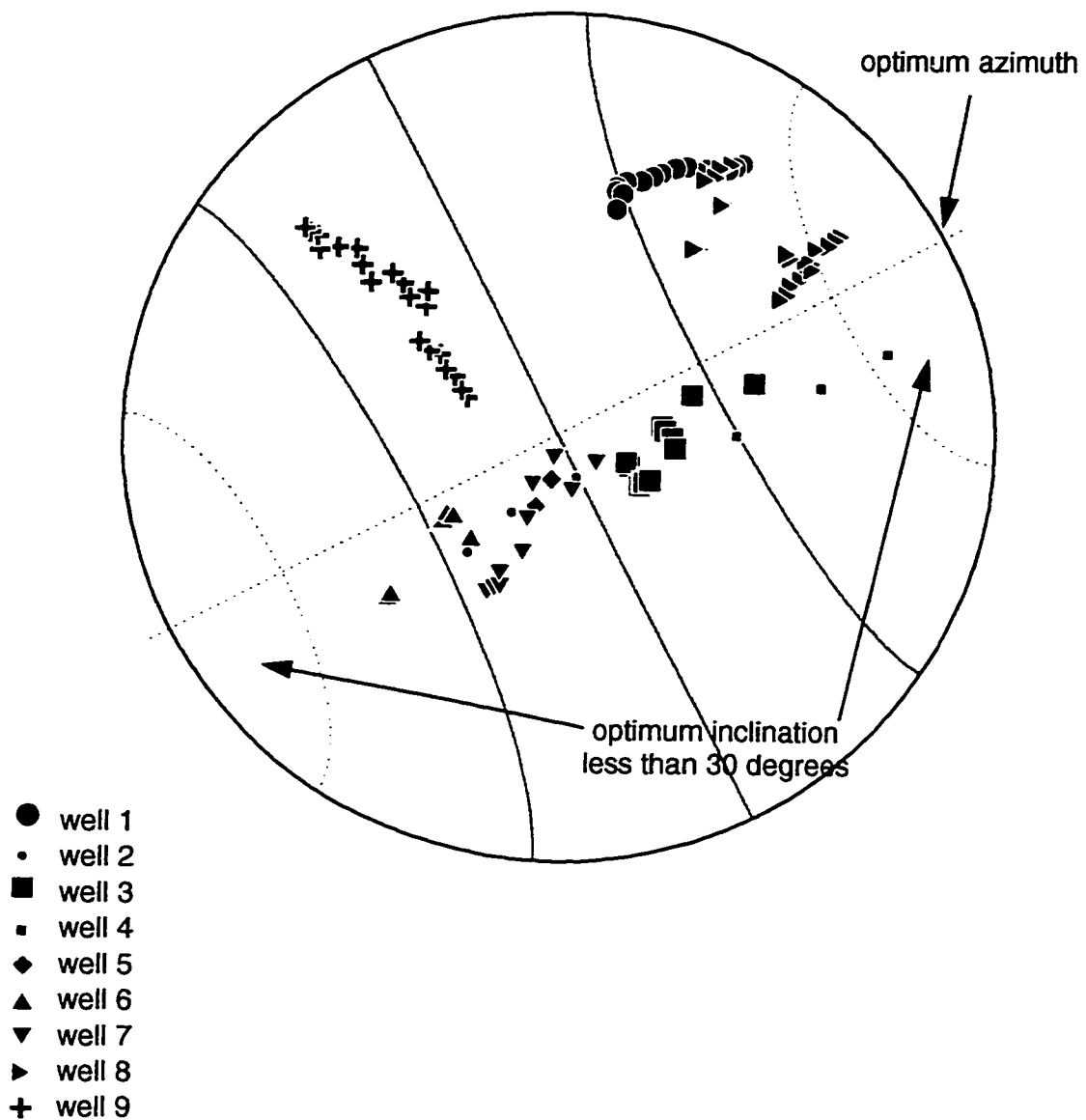


Figure 4-8: Well drill directions compared to optimal direction.

The stereonet projection shows the well survey points relative to the “optimal” drilling direction.

show 30 degree increments from vertical in the middle to 30 degrees off vertical on either side of the middle line.

The optimal direction, as defined above, is in the area of low inclination, above the red curved line. The greater the deviation of the well path from the optimal area, the poorer the direction. Two wells, Wells 4 and 8 have points within the optimal area, however, most of their points are within the next band. Wells 1, 3 and 6 have drilling points in the next band, with Well 1 being the best placed of these wells. The remaining survey points are in the poor drilling zone, bounded between the two curved blue lines.

Well 9 has points that approach horizontal drilling, but is no better placed than many of the wells drilled nearly vertically because of its drilling azimuth. Well 9 was directed nearly parallel to strike, resulting in a poorer chance of intersecting the more open Type 2 fractures. The one advantage to drilling parallel to strike, is that a well path can remain structurally high over longer distances. Hence, even though less fracture volume will be intersected per meter, more meters can be drilled. This is an important consideration when determining the optimum direction beyond the definition of “optimum drilling” given in this study.

It is difficult to compare the drilling direction to production in the wells. Other factors affecting production and production rates would include: matrix porosity and permeability; reservoir pressure and temperature; well height above free water; borehole radius; completion techniques; gas pipe line pressures; production practices and pool reserves. No attempt is made to back out these factors to compare well performance to the optimum drill criteria defined in this study (see Chapter 5, recommendation 2). However, some interesting correlations between production and the well positions do

exist. Wells 1, 8, 4 and 3, have been the best producers to date. These wells, excluding Well 3, are also the best placed wells according to my optimal drilling criteria. Well 3 is the newest well in the study and it will be interesting to see its ultimate gas recovery. Wells 2 and 6 were drilled into a gas column but very near to water. The well tested gas but the rates declined quickly and they were never tied to the gas processing system. Wells 5, and 7 have produced gas but were close to the gas/water contact surface. Flow rates in these wells quickly declined and will have low total gas recoveries.

Summary

The correlation between production and drilling direction is qualitative at best and complicated by many other factors. However, Cooper (1998) demonstrated that drill direction can improve gas flow rates in the upper Triassic in NEBC. Given Cooper's (1991) observations, then the idea of drilling in the direction that gives the greatest volume of fracture aperture makes sense.

The data in this study show that a consistent direction is observed in many of the wells. Drilling "horizontally", parallel to bedding or within 30 degrees of bedding is the best inclination. That observation is not a surprise as fractures have often been observed to be at high angles to bedding. In this study that relationship is quantified. However, drilling horizontally is not enough. The Type 2 fractures have greater apertures so it is important to direct the drill bit towards the regional dip direction. In this area, the most frequent fracture set also has an impact on drilling azimuth. This set strikes NNE/SSW and skews the optimum azimuth towards the normal of these fracture planes. On average, the azimuth is skewed 20 degrees.

Additionally, there are differences in fracture volumes with depth in the section. The greatest fracture volume is in the upper unit, followed by the lower unit and middle unit. These variations could be due to lithology changes, structural influence, or more likely both. Although drilling in the upper unit will give greater fracture volumes, the upper fracture network must be connected to the reservoir rocks to provide sustained flow.

The combination of the right drilling inclination, azimuth and vertically targeted section should give the greatest fracture volume. Hopefully, this will result in greater gas flows and ultimate recoveries from the gas pools.

Chapter 5

Conclusions and Recommendations

Conclusions

Fracture Occurrence

In previous published examples (Nolen-Hoeksema and Howard, 1987; Narr, 1996), fracture intercept and flow diagrams were constructed by dividing the data into sets prior to calculating fracture densities and volumes. This technique is difficult to apply when there are many fracture sets and bedding dip domains. Additionally, the fracture sets were divided before the correction for sampling direction bias was applied. In practice, infrequent fractures that are sub-parallel to the scan line could be eliminated before applying the correction, even though, after the correction these fractures could be significantly more abundant.

In this thesis, fracture occurrence is calculated before the bedding and fractures are unfolded. The correction for sampling bias is discretely applied to every fracture and does not require grouping of the fractures into sets before the weighting is applied. This simple and more elegant approach is easier to apply and more accurate. It is applied to fractures on structurally complex folds with different dip domains. In addition, the weighting is applied prior to stereonet contouring and construction of rose diagrams of relative fracture frequency. The occurrence weighted stereonet and rose diagrams result in more accurate and consistent representations of the actual 3D orientation, distribution and volume of fractures than the raw data, which is biased by the sampling direction.

Fracture Rotations

The vast majority of the fractures in this study are at high angles to bedding. Hence, the fractures are rotated to a common reference plane with bedding horizontal. The fractures are rotated by a two part rotation. The rotation attempts to unfold the fold by first rotating out the structural plunge followed by unfolding the fold, rotating each bedding dip domain around the fold axis to horizontal. The fracture rotations result in discrete fracture sets that are comparable between wells. This technique is an effective way to compare large quantities of fracture data from different wells in different structural positions.

Fracture Orientations

The most frequent fracture set has an orientation that strikes NNE/SSW between 000-030/180-210. Although this set can be classified as a Stearns' Type 1 shear fracture for some wells, in other wells, the frequent set falls between Stearns' modeled orientations. Three explanations for this unexpected fracture orientation are: the set formed before folding in the area; the set formed because of basement structural influences causing local transpression during folding or; the set formed after folding due to post folding extension or other change in the stress regime.

Fracture Apertures

Many of the fracture apertures fit a log-normal distribution. The apertures varied within wells by several orders of magnitude. The median aperture value, compared between wells, can also vary by several orders of magnitude. The observed differences between wells are either due to true differences or to imaging or calibration errors.

The large aperture fractures have significant influence on fracture volume measurements and control over the optimal drilling direction. Commonly, the large aperture fractures have Type 2 orientations. In wells without Type 2 fractures, the most frequent fracture set (NNE/SSW) has the largest aperture fractures. In Well 3, low angle fractures, assumed to be related to thrust faults in the well, have large apertures.

Structural Position and Fracture Densities and Volumes

The two wells with the greatest fracture densities are located in planar dipping limbs, one a forelimb, the other a backlimb. The well with the greatest fracture density is drilled into the area of steepest fold plunge measured in the nine wells. However, other wells with little plunge also had above average fracture densities. Comparisons between changes in bedding curvature, bedding dips and limb position gave no consistent correlation with fracture density.

The fold crestal areas appear to have the greatest fracture volume. However, comparing fracture volumes between wells is dependent on having error free aperture measurements. The median aperture measured at each well varies significantly between wells. Hydraulic fracture volume depends on the aperture cubed. Hence errors will be compounded in volume calculations. With this concern in mind, the observation that fracture volume appears greatest on the crest should be more closely examined (see Recommendations).

Fracture Changes Vertically in the Well

The upper Triassic is divided into three intervals. The upper interval is from the top of unit P4 to the base of unit P3. The middle interval is from the top of P2 to the base of B3. The lower interval is from the top of B2 to the Charlie Lake Formation or to the

bottom of the well if the Charlie Lake is not penetrated. Fracture densities and volumes are calculated for the three intervals. The upper interval is commonly the most densely fractured (in seven of the nine wells) and had the largest fracture volume (in six of the nine wells). The lower interval commonly has the second highest fracture density and volume. The middle interval is the most poorly fractured zone. The control on fracture densities and volumes is likely due to lithology differences, structural influences, or most likely a combination of both factors.

Optimal Drilling Direction

The greatest fracture densities are generally encountered in either the east or west direction. The large aperture fractures are usually Type 2 fractures striking NW/SE. These fractures skew the optimal drilling azimuth counterclockwise from the east/west greatest fracture density direction. The optimal drilling azimuth is averaged for six wells with similar optimal directions. The optimal average is 70 degrees, measured counterclockwise from the structural trend in the region of the well.

Most of the fractures are at high angles to bedding. Hence, the optimal drilling inclination is nearly parallel to bedding in most wells. The predicted fracture volume intersection remains high for drilling angles of 0 to 30 degrees to bedding, but declines quickly beyond 30 degrees. Wells perpendicular to bedding are predicted to intersect approximately 25% of the fracture aperture volume of a bedding-parallel well drilled in the optimal azimuth direction.

Recommendations

Aperture Measurements

To compare fracture volumes between wells, accurate aperture measurements must be derived. As previously discussed there is a wide variation in aperture values between wells that could be due to imaging and measurement error. Errors in calibration of mud resistivity will result in erroneous aperture values.

Two approaches can be used to help reduce the error between wells in aperture measurement. The first approach is to take more care in correctly measuring the mud resistivity. Mud samples should be collected and stored for further testing and calibration as a routine procedure when collecting FMS or FMI data.

The second approach is to adjust the aperture measurements to better correlate between wells. The adjustment does not need to correct apertures to absolute values, but to the same relative measurement between wells. A possible method described in Chapter 5 is to shift the median aperture value between wells to the same relative aperture measurement. The remaining aperture values would be bulk shifted on a logarithmic curve to match the shifted median value.

Production and Optimal Drilling Direction

Theoretically, aperture volumes effect gas flow out of a tight gas reservoir. However, this relationship has not been measured in producing fields in Triassic plays of NEBC. There are many obstacles to quantifying this relationship due to differences between wells and producing fields.

Cooper (1998) showed that horizontal drilling can improve production rates. The vertical well and the side track are drilled in close proximity into the same gas pool.

Hence, many of the differences usually observed between wells are reduced in this example. The image data were likely collected with the same tool in the same drilling mud. All the rock, reservoir conditions, and well conditions should also be similar. This unique drilling example could be used to attempt a comparison between aperture measurements and production rates.

In addition, an attempt could be made to normalize differences between wells in this study. This would require factoring out parameters that effect production rates, such as, pressure, temperature, pipe size, etc.. This is a complicated problem, but, it is the most important link between the work in this study and economic gas production.

REFERENCES

- Aguilera, R., 1995. Naturally Fractured Reservoirs, Second Edition. Penwell Publishing Company, Tulsa, Oklahoma, 521 p.
- Barclay, J. E., 1993. Triassic petroleum geology, Western Canada Basin and neighbouring Yukon Territory and American Regions: Bibliography and Summary (with contributions from D. Gibson). Bulletin of Canadian Petroleum Geology, v. 41, p. 437-452.
- Barss, D.L. and Montandon, F.A., 1981. Sukunka-Bullmoose gas fields: models for a developing trend in the southern Foothills of northeast British Columbia. Bulletin of Canadian Petroleum Geology, v. 29, p. 293-333.
- Beattie, E.T., 1984. Structural style affected by Devonian facies changes, Ram Range, Alberta. M.Sc. Thesis, University of Calgary, 144 p.
- Bird, T.D., Barclay, J.E., Campbell, R.I., Lee, P.J., Waghmare, R.R., Dallaire, S.M., and Conn, R.F., 1994. Triassic gas resources of the Western Canada Sedimentary Basin, Interior Plains, Part1: Geological Play Analysis and Resource Assessment. Geologic Survey of Canada Open File 2911, 91 p.

Bourke, L.T., 1989. Recognizing artifact images of the formation MicroScanner Tool. Transactions of SPWLA 30th Annual Logging Symposium, June 11-14, 1989. Symposium Pager G, 14 p.

Bourke, L.T., 1992. Sedimentological borehole image analysis in clastic rocks: a systematic approach to interpretation. In A. Hurst, C.M. Griffiths, and P.F. Worthington (eds), Geological Application of Wireline Logs II, Geological Society, London, Special Publication 65, p. 31-42.

Burger, H.R. and Thompson, M.D., 1970. Fracture analysis of the Carmicheal Peak Anticline, Madison County, Montana. Geological Society of America Bulletin, v. 81, p. 1813-1836.

Cooper, M., 1991. The analysis of fracture systems in subsurface thrust structures from the foothills of the Canadian Rockies. In McClay, K.R.(ed), Thrust Tectonics, Chapman and Hall, p. 391-405.

Cooper, M., Brearley, C., Fermor, P., and Bradish, D., 1998. From non-commercial to commercial; horizontal drilling in the fractured Triassic carbonates of the Boulder Field, B.C. Foothills. Geo-Triad '98 Abstracts, joint convention Canadian Society of Petroleum Geologists, Canadian Society of Exploration Geophysicist and the Canadian Well Logging Society, p. 284-285.

- Davies, G.D., 1992. The Upper Triassic Baldonnel project, northeastern British Columbia, phase 2. Graham Davies Geological Consultants Limited, Calgary, Alberta, Canada, Consultants Report, 105 p.
- Dixon, J.M., 1995. Centrifuge modelling in the Foothills Research Project, 1995: Thrust reactivation of normal faults and facies boundaries. Foothills Research Project, 1995 Research Report, p. 5-1 to 5-22.
- Erickson, S.G., and Jamison, W.R., 1995. Viscous-plastic finite-element models of fault-bend folds. *Journal of Structural Geology*, v. 17, no. 4, p. 561-573.
- Fitzgerald, E.L., 1968. Structure of British Columbia Foothills, Canada. *American Association of Petroleum Geologists Bulletin*, v. 52, p.641- 664.
- Gibson, D.W., 1972. Triassic Stratigraphy of the Pine Pass-Smokey River Area, Rocky Mountain Foothills and Front Ranges of British Columbia Columbia and Alberta. Geological Survey of Canada, Paper 71-30, 108 p.
- Gibson, D.W., 1975. Triassic rocks of the Rocky Mountain Foothills and Front Ranges of Northeastern British Columbia and West-Central Alberta. *Geologic Survey of Canada, Bulletin 247*, 61 p.

- Gibson, D.W., 1992. Triassic strata of the foreland belt; in Gabrielse, H. and C. J. Yorath, *Geology of the Cordilleran Orogen in Canada*, Geological Survey of Canada, *Geology of Canada*, no. 4, p. 265-276.
- Gibson, D.W. and Edwards, D.E., 1990. An overview of Triassic stratigraphy and depositional environments in the Rocky Mountain Foothills and Western Interior Plains, Peace River Arch Area; Northeastern British Columbia. *Bulletin of Canadian Petroleum Geology*, v. 38A; p. 146-158.
- Harker, S.D., McGann, G.J., Bourke, L.T., and Adams, J.T., 1990. Methodology of Formation Microscanner Tool image interpretation in Claymore and Scapa Fields (North Sea); in Hurst, A., Lovell, M.A., Morton, A.C., (eds) *Geological Applications of Wireline Logs*. Geological Society, London, Special Publication 48; p. 11-25.
- Homza, T.X., and Wallace, W.K., 1995. Geometric and kinematic models for detachment folds with fixed and variable detachment depths. *Journal of Structural Geology*, v. 17, no. 4, p. 575-588.
- Hudson, J. A., and Priest, S. D., 1979. Discontinuity frequency in rock masses. *International Journal of Rock Mechanics and Mining Sciences and Geomechanics Abstracts*, v. 20, p. 73-89.
- Jamison, W.R., 1995. Fractured reservoirs in fold and thrust belts. Course notes, October 2-4, 1995, Calgary, AB., 157 p.

- Jamison, W.R., 1997. Quantitative evaluation of fractures on Monkshood Anticline, a detachment fold in the foothills of western Canada. *American Association of Petroleum Geologist Bulletin*, v. 81, no. 7, p. 1110-1132.
- Joubert, T.G. and Spratt, D.A., 1995. Folding and fracturing of Triassic carbonates in NE British Columbia. *FRP Research Report*, v. 1, p. 10-1 to 10-8.
- Lacazette, A., 1991, A new stereographic technique for the reduction of scanline survey data of geologic fractures. *Computers and Geosciences*, v. 17, p. 445-463.
- La Pointe, P. H., and Hudson, J. A., 1985. Characterization and interpretation of rock mass joint patterns. *Geological Society of America Special Paper 199*, Pt 1, p. 1-25.
- Luthi, S.M. and Souhaite, P., 1990. Fracture apertures from electrical borehole scans. *Geophysics*, v. 55, p. 821-833.
- McMechan, M.E., 1985. Low-Taper Triangle Zone Geometry: An interpretation of the Rocky Mountain Foothills, Pine Pass - Peace River Area, British Columbia. *Bulletin of Canadian Petroleum Geology*, v. 33, p. 31-38.
- McMechan, M.E., 1987. Stratigraphy and structure, Mount Selwyn map area, Rocky Mountains, northeastern British Columbia. *Geological Survey of Canada, Paper 85-28*, 34 p.

McMechan, M.E., and Thompson, R.I. 1989. Structural style and history of the Rocky Mountain fold and thrust belt. In Ricketts, B.D. (ed), *Western Canadian Sedimentary Basin; A Case History*. Canadian Society of Petroleum Geologists, p. 47-72.

McMechan, M.E., and Thompson, R.I., 1993. The Canadian cordilleran fold and thrust belt south of 66 deg. N and its influence on the western interior basin. In Caldwell, W.G.E. and Kauffman, E.G., eds., *Evolution of the western interior basin*; Geological Association Canada, Special Paper 39, p. 73-90.

Montgomery, S., 1994. Foothills Triassic Structure Play, N.E. British Columbia, Canada, *Petroleum Frontiers*. Petroleum Information Corporation, Littleton, CO. 107 p.

Muecke, G.K. and Charlesworth, H.A.K., 1966. Jointing in folded Cardium sandstones along the Bow River, Alberta. *Canadian Journal of Earth Sciences*, v. 3, p. 579-596.

Narr, W., 1991. Fracture density in the deep subsurface: Techniques with applications to the Point Arguello Oil Field. *American Association of Petroleum Geologist Bulletin*, V. 75, No. 8, p. 1300-1323.

Narr, W., 1996, Estimating average fracture spacing in subsurface rock. *American Association of Petroleum Geologist Bulletin*, v. 80, p. 1565-1586.

Nelson, R.A., 1985. *Geologic Analysis of Naturally Fractured Reservoirs*. Gulf Publishing Company, Houston, TX., 320 p.

Nelson, R.A. and Serra, S., 1995. Vertical and lateral variations in fracture spacing in folded carbonate sections and its relation to locating horizontal wells. *Journal of Canadian Petroleum Technology*, v. 34, no. 5, p. 51-56.

Nolen-Hoeksema, R.C., and Howard, J. H., 1987, Estimating drilling direction for optimum production in fractured reservoir. *American Association of Petroleum Geologist Bulletin*, v. 71, p. 958-966.

Norris, D.K. 1971. Comparative study of the Castle River and other folds in the eastern cordillera of Canada. *Geological Survey of Canada, Bulletin* 205, 58 p.

McQuillan, H. 1973. Small-scale fracture density in the Asmari Formation of southwest Iran and its relation to bed thickness and structural setting. *American Association of Petroleum Geologist Bulletin*, v. 57, p. 2367-2385.

McQuillan, H., 1974. Fracture patterns on Kuh-e Asmari Anticline, southwest Iran. *American Association of Petroleum Geologist Bulletin*, v. 98, p. 236-246.

Ramsay, J.R. 1967. *Folding and Fracturing of Rocks*. McGraw-Hill, New York, NY., 568 p.

Rice, M.C., 1997. Petrophysical evaluation and well performance characterization of the upper Triassic Pardonet and Baldonnel Formation fractured carbonates, Brazion Area, N.E. British Columbia. Unpublished Amoco Production Company internal report, 197 p.

© Schlumberger, 1992. FMI* Fullbore Formation MicroImager. Schlumberger Educational Services, Houston, Texas, 42 p.

Stearns, D. W., 1968. Certain aspects of fracture in natural deformed rocks. In R. E. Rieker, ed., NSF advanced science seminar in rock mechanics: Bedford, Massachusetts, Air Force Cambridge Research Laboratory Special Report, p. 97-118.

Stearns, D. W., 1972. Structural interpretation of the fractures associated with the Bonita Fault. Guidebook 23rd Field Conference, New Mexico Geological Society, East Central Mexico, p. 161-164.

Stearns, D.W., and Friedman, M., 1972, Reservoirs in Fractured Rock, American Association of Petroleum Geologist, Memoir 16, p. 82-100.

Suppe, J. 1985. Principles of Structural Geology. Prentice Hall, NJ, 537 p.

Tearpock, D.J. and Bischke, R.E., 1991. Applied Subsurface Geological Mapping. Prentice-Hall, Englewood Cliffs, NJ., 648 p.

Terzaghi, R. D., 1965, Sources in errors in joint surveys. *Geotechnique*, v. 15, p. 287-304.

Thompson, R.I., 1979. A Structure Interpretation across part of the Northern Rocky Mountains of Canada. *Canadian Journal of Earth Sciences*, v. 16, p. 1228-1241.

Thompson, R.I., 1982, The nature and significance of large 'blind' thrusts within the Northern Rocky Mountains of Canada. In Powers, R.B., ed., *Geological Studies of the Cordilleran Thrust Belt*, Rocky Mountain Association of Geologist, v.1, p. 47-59.

Thompson, R.I., 1989. Stratigraphy, tectonic evolution and structural analysis of the Halfway River map area (94 B), Northern Rocky Mountains, British Columbia. Geological Survey of Canada, Memoir 425, 119 p.

Yose, L., Hamilton, D., Hefferman, P., and Vickerman, K., 1998. Calibration of fracture interpretation from image logs with core data: example from Norman Wells, N.W.T., Canada. *Geo-Triad '98 Abstracts*, joint convention Canadian Society of Petroleum Geologists, Canadian Society of Exploration Geophysicist and the Canadian Well Logging Society, p. 412.

Appendix 1

Occurrence - Visual Basic Program

Introduction

The following program calculates fracture “occurrence” from Microsoft® Excel spread sheets. The program is in a workbook called “occ” and executed as an Excel macro. Two Excel data sets (in separate spread sheets) are used as inputs. The first spread sheet is three columns wide with fracture measurements of depth (measured depth), dip (00-90 degrees) and dip azimuth (000-360 degrees). The second spread sheet is three columns wide with well survey measurements of depth (measured depth), well inclination (in degrees, with vertical = 00 and horizontal = 90) and survey azimuth (000-360 degrees). The occurrence program prompts the user for the name of the two spread sheets and the columns of the data given above. The prompted column input must be given as a number (e.g. column A is 1, column B is 2, etc.). The program will ask the user for the name of the output data sheet. No sheet is required as an output sheet before the program is executed. The output data sheet will have four columns containing fracture measured depth (column 1), fracture azimuth (column 2), fracture inclination (column 3) and fracture occurrence (column 4).

In addition to the program, three additional sheets are need as dialog boxes for the program. The dialog boxes are used to pass the columns of the data input into the occurrence program. The dialog boxes are shown at the end of the program.

In this thesis the occurrence values were calculated on the fractures before rotation.

If the occurrence is applied after the fracture rotation, than the well survey input must also be rotated.

Program

The program is as follows:

Sub occur()

```
'      this macro calculates the occurrence value for each fracture
'      within a group down the length of a well bore.
'      Occurrence is the relative weighting associated with
'      each fracture and depends on the scan line of the fracture
'      sampling. It is defined as:
'          1/length of scan line * dot product between scan
'          direction and fracture normal (unit vectors)
'      The input is a directional survey with survey points
'      (dip direction and azimuth) and fractures (azimuth and
'      inclination of the maximum dip direction)
Dim length As Single 'length is the distance between the first and _
                        last fracture
Dim inputwell, inputfrac As String 'name of the input directional survey _
                                    and fracture file
Dim colnwellmd, colnwellinc, colnwellazm As Integer 'columns for _
                                                    measured depth, inclination and azimuth of directional _
                                                    survey
Dim colnfracmd, colnfracinc, colnfracazm As Integer 'columns for _
                                                    measured depth, inclination and azimuth for the fracture _
                                                    data set

Workbooks("occ.xls").DialogSheets("intro").Show

'FRACTURE DATA SET - WHERE IS IT?
'ask the user for the fracture data sheet - select sheet
inputfrac = InputBox("enter the name of the fracture data sheet")
Sheets(inputfrac).Select

'clear dialog box
With Workbooks("occ.xls").DialogSheets("dia_column_fracture")
    .EditBoxes.Text = ""
```

End With

```

    'ask user for columns of fracture data
    Workbooks("occ.xls").DialogSheets("dia_column_fracture").Show
    'from dialog box define columns
    colnfracmd = CInt(Workbooks("occ.xls"). _
        DialogSheets("dia_column_fracture"). _
        EditBoxes("mdbox").Text)
    colnfracinc = CInt(Workbooks("occ.xls"). _
        DialogSheets("dia_column_fracture"). _
        EditBoxes("inbox").Text)
    colnfracazm = CInt(Workbooks("occ.xls"). _
        DialogSheets("dia_column_fracture"). _
        EditBoxes("azmbox").Text)

```

'DIRECTIONAL SURVEY

```

    'ask the user for the directional survey sheet - select sheet
    inputwell = InputBox("Enter the name of the directional survey sheet")
    Sheets(inputwell).Select
    'clear dialog box
    With Workbooks("occ.xls").DialogSheets("dia_column_well")
        .EditBoxes.Text = ""
    End With

```

```

    'ask user for columns of well data
    Workbooks("occ.xls").DialogSheets("dia_column_well").Show
    'from dialog box define columns
    colnwellmd = CInt(Workbooks("occ.xls"). _
        DialogSheets("dia_column_well"). _
        EditBoxes("mdbox").Text)
    colnwellinc = CInt(Workbooks("occ.xls"). _
        DialogSheets("dia_column_well"). _
        EditBoxes("inbox").Text)
    colnwellazm = CInt(Workbooks("occ.xls"). _
        DialogSheets("dia_column_well"). _
        EditBoxes("azmbox").Text)

```

'READ THE DATA INTO ARRAYS INTO MEMORY

```

wellmd = makearray(inputwell, colnwellmd)
wellinc = makearray(inputwell, colnwellinc)
wellazm = makearray(inputwell, colnwellazm)
fracmd = makearray(inputfrac, colnfracmd)
fracinc = makearray(inputfrac, colnfracinc)
fracazm = makearray(inputfrac, colnfracazm)

```

```

    'find the length of the of scan line
    'distance between first and last fracture
    length = findlength(inputfrac, colnfracmd)
    occarray = occ(wellmd, wellinc, wellazm, fracmd, fracinc, fracazm, length)
    Worksheets.Add
    sheetname = Application.ActiveSheet.Name
    Sheets(sheetname).Name = _
    InputBox("Enter a name for the output data sheet")
    Call writearray(fracmd, "MEASURED DEPTH", 1)
    Call writearray(fracazm, "AZIMUTH", 2)
    Call writearray(fracinc, "INCLINATION", 3)
    Call writearray(occarray, "OCCURRENCE", 4)

```

End Sub

```

Function findlength(sht, column)
    Dim j As Integer, length1 As Single, length2 As Single
    j = 1
    'select fracture data
    Sheets(sht).Select

    'do test to see if cells have text or are empty for first cells
    Do
        Select Case VarType(Cells(j, column))
            Case 5
                Exit Do
        End Select
        j = j + 1
    Loop
    length1 = Cells(j, column) 'the md for the first data point

    'find the last cell by looking for an empty cell
    Do
        Select Case VarType(Cells(j, column))
            Case 0
                Exit Do
            Case 8
                Exit Do
        End Select
        j = j + 1
    Loop
    length2 = Cells(j - 1, column) 'the md for the last data point
    findlength = length2 - length1
End Function

```

Function makearray(sht, colmn)

Dim j, k, n, p As Integer

' WRITE THE VARIABLES INTO AN ARRAY

j = 1

'select sheet

Sheets(sht).Select

'do test to see if cells have text or are empty for first cells

Do

Select Case VarType(Cells(j, colmn))

Case 5

Exit Do

End Select

j = j + 1

Loop

'find the last cell by looking for an empty cell

k = j

Do

Select Case VarType(Cells(k + 1, colmn))

Case 0

Exit Do

Case 8

Exit Do

End Select

k = k + 1

Loop

'p is the number of data cells

p = k - j + 1

ReDim outarray(1 To p) As Single

For n = 1 To p

outarray(n) = Cells(n + j - 1, colmn)

Next n

makearray = outarray

End Function

Function occ(wellmd, wellinc, wellazm, fracmd, fracinc, fracazm, length)

Dim j, k As Integer

```

ReDim OCCURRENCE(LBound(fracmd) To UBound(fracmd))
pirad = 3.141927 / 180
For k = LBound(fracmd) To UBound(fracmd)
  For j = LBound(wellmd) To UBound(wellmd)
    Do While wellmd(j) > fracmd(k)
      OCCURRENCE(k) = Cos(fracinc(k) * pirad) * _
        Cos(wellinc(j - 1) * pirad) - Sin(fracinc(k) * pirad) * _
        Sin(wellinc(j - 1) * pirad) * _
        Cos((wellazm(j - 1) - fracazm(k)) * pirad)
      OCCURRENCE(k) = 1 / (OCCURRENCE(k) * length)
      OCCURRENCE(k) = Sqr(OCCURRENCE(k) * OCCURRENCE(k))
      k = k + 1
    If k = UBound(fracmd) + 1 Then Exit Do
  Loop
  If k = UBound(fracmd) + 1 Then Exit For
Next j
If k = UBound(fracmd) + 1 Then Exit For
Next k
occ = OCCURRENCE
End Function

Sub writearray(inputarray, Title, Column)
  Cells(1, Column) = Title
  Dim k As Integer
  For k = LBound(inputarray) To UBound(inputarray)
    Cells(k + 2, Column) = inputarray(k)
  Next
End Sub

```

Dialog boxes.

1. Dialog box "intro "

This MACRO calculates "occurrence" measurements between a wellbore and a set of fracture planes. The format of the fracture planes must be in dip direction and dip. The format for the well must be in azimuth and inclination (where vertical is 0 degrees and horizontal is 90 degrees) and azimuth.



2. Spread sheet "dia_column_fracture".

Enter the columns of the
fracture data for:

columns	
measured depth	1
inclination	6
azimuth	5



3. Spread sheet "dia_column_well".

Enter the columns of the
directional survey for:

columns	
measured depth	1
inclination	3
azimuth	2



Appendix 2

Intercept and Flow Diagrams - Visual Basic Program

Introduction

The following program calculates two matrices that are used for flow and intercept diagrams. The program is executed as a Microsoft® Excel macro. An Excel data set (Excel spread sheet) is used as a data input. The input data sheet must be called "input" with the fracture data formatted as follows: occurrence in column 4; dip azimuth (000-360 degrees) in column 5; dip (00-90 degrees) in column 6; and aperture in column 7.

Two blank spread sheets must be in the data work book called "out_fract_flow" and "out_fract_int". The program writes the intercept and flow matrices to the output sheets. The matrix gives calculated intercept and flow values in azimuths of 5 degree increments from 000-355 degrees and in inclinations of 15 degree increments from 00-90 degrees.

In this thesis the intercept and flow matrices were calculated after the fractures are rotated.

Program

The program is as follows:

```
'
' Macro1 Macro
' Macro recorded 12/4/96 by Amoco Production Company
'
'
Sub intflow()
    'This routine calculates fracture intercept rate based on a _
```

group of fractures. The fractures have been sampled in a well _
 using FMI or FMS then these sampled fractures are used to build _
 an expected fracture density in a new well. The program calculates _
 the fracture intercept rate for a variety of drill azimuths _
 and inclinations. The program is currently set for a maximum of 500 fractures. _
 The input fracture data is given in dip azimuth and inclination _
 of the maximum dip vector. An occurrence measure is needed, calculated _
 from $1 / \text{LENGTH} * \text{COS} (\text{ANGLE BETWEEN SAMPLING WELL AND}$
 FRACTURE POLE) _
 (Lacazette 1991) _

'The input fracture data must have a theta, alpha and occ.
 'theta is fracture azimuth, alpha the inclination, occ the occurrence

Dim deltakappa, deltagamma As Single
 Dim colntheta, colnalpha, colnocc As Integer
 'deltakappa is the steps in azimuth of drill orientation
 ' deltagamma is the well inclination steps from horizontal
 ' coln... represents the column on the spread sheet for fracture information

deltakappa = 5
 deltagamma = 15
 colntheta = 5
 colnalpha = 6
 colnocc = 4
 colnapp = 7

deltakappa = rads(deltakappa)
 deltagamma = rads(deltagamma)
 Call writeangle(deltakappa)
 Call rotincl(deltagamma, deltakappa, colntheta, colnalpha, _
 colnocc, colnapp)

End Sub

Sub writeangle(deltakappa)
 'this routine writes the different azimuths into the _
 columns of row 1
 Dim kcount As Integer, kappaone As Single
 kcount = 1
 kappaone = 0

```

    kappaone = rads(kappaone)
Do While kappaone < 6.2831
'test to see if the azimuth is less than 360 degrees
    Sheets("out_fract_int").Select
    Cells(kcount, 1) = CInt(kappaone * 180 / 3.14159265)
    Sheets("out_fract_flow").Select
    Cells(kcount, 1) = CInt(kappaone * 180 / 3.14159265)
'write the azimuth out to output
    kappaone = kappaone + deltakappa
    kcount = kcount + 1
Loop
End Sub
',
',

Sub rotincl(deltagamma, deltakappa, colntheta, colnalpha, colnocc, colnapp)
'this routine loops through for different well inclinations _
that is - it starts with the first inclination then calculates _
each azimuth then gets the next gamma ...
',
    Dim gamma As Single, jcount As Integer
'tgamma is the inclination of the well bore measured from _
the horizontal. Gamma can range from 0 to 90 degrees. _
deltagamma is the steps that the program will calculate gamma for
    jcount = 2
    gamma = 0
Do While gamma <= 1.570797
    Call rotazm(gamma, deltakappa, colntheta, colnalpha, _
colnocc, colnapp, jcount)
    gamma = gamma + deltagamma
    jcount = jcount + 1
Loop
End Sub
',
',

Sub rotazm(gamma, deltakappa, colntheta, colnalpha, colnocc, colnapp, jcount)
Dim kappa As Single, icount As Integer, fcount As Integer
Dim pint As Single, pflow As Single
' kappa is the azimuth in the new sampling direction
' icount is the counter for the loop
    icount = 1
    kappa = 0
Do While kappa < 6.2831
'calculate fracture intercept rate
    pint = sumazmint(kappa, gamma, colntheta, colnalpha, colnocc)
'calculate flow intercept rate

```

```

    pflow = sumazmflow(kappa, gamma, colntheta, _
    colnalpha, colnocc, colnapp)
    'write out pint and pflow into output
    Sheets("out_fract_int").Select
    Cells(icount, jcount) = pint
    Sheets("out_fract_flow").Select
    Cells(icount, jcount) = pflow
    kappa = kappa + deltakappa
    icount = icount + 1
Loop
End Sub
',
Function sumazmint(kappa, gamma, colntheta, colnalpha, colnocc)
    Dim theta As Single, alpha As Single, occ As Single
    'theta is fracture maximum dip vector direction
    'gamma is the fracture azimuth for maximum dip vector
    'theta and gamma are later converted to fracture poles
    'occ is the occurrence (Lacazette, 1991) and has been _
    previously calculated from the directional survey
    Dim pintj As Single
    ' pint is the fracture intercept rate
    ' pintj is the intercept calculated for the jth fracture
    ,
    Dim j As Integer
    ' j is the row counter and represents the number of fractures
    ,
    Sheets("input").Select
    For j = 1 To 500
        If IsNumeric(Cells(j, colntheta)) Then
            If IsEmpty(Cells(j, colntheta)) Then Exit For
            theta = Cells(j, colntheta)
            alpha = Cells(j, colnalpha)
            occ = Cells(j, colnocc)
            'call pole functions to convert theta and alpha to poles
            theta = poleazm(theta)
            alpha = poleinc(alpha)
            'call radian to covert angles to radians
            theta = rads(theta)
            alpha = rads(alpha)
            pintj = ((Cos(gamma)) * (Cos(alpha)) * (Cos(theta - kappa)))
            pintj = pintj + (Sin(alpha)) * (Sin(gamma))
            pintj = (Sqr(pintj * pintj)) * occ
            pint = pint + pintj
        Else

```

```

End If
Next j

```

```

sumazmint = pint
End Function

```

```

Function sumazmflow(kappa, gamma, colntheta, _
colnalpha, colnocc, colnapp)
    Dim theta As Single, alpha As Single, occ As Single
    'theta is fracture maximum dip vector direction
    'gamma is the fracture azimuth for maximum dip vector
    'theta and gamma are later converted to fracture poles
    'occ is the occurrence (Lacazette, 1991) and has been _
    previously calculated from the directional survey
    Dim pflowj As Single
    ' pint is the fracture intercept rate
    ' pintj is the intercept calc for the jth fracture
    ,

    Dim j As Integer
    ' j is the row counter and represents the number of fractures
    ,

```

```

Sheets("input").Select
For j = 1 To 500
    If IsNumeric(Cells(j, colntheta)) Then
    If IsEmpty(Cells(j, colntheta)) Then Exit For
        theta = Cells(j, colntheta)
        alpha = Cells(j, colnalpha)
        occ = Cells(j, colnocc)
        app = Cells(j, colnapp)
        'call pole functions to convert theta and alpha to poles
        theta = poleazm(theta)
        alpha = poleinc(alpha)
        'call radian to covert angles to radians
        theta = rads(theta)
        alpha = rads(alpha)
        pflowj = ((Cos(gamma)) * (Cos(alpha)) * (Cos(theta - kappa)))
        pflowj = pflowj + (Sin(alpha)) * (Sin(gamma))
        pflowj = (Sqr(pflowj * pflowj)) * occ
        pflowj = pflowj * app * app * app
        pflow = pflow + pflowj

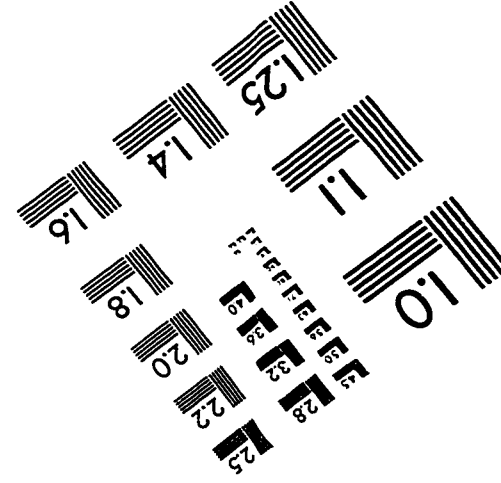
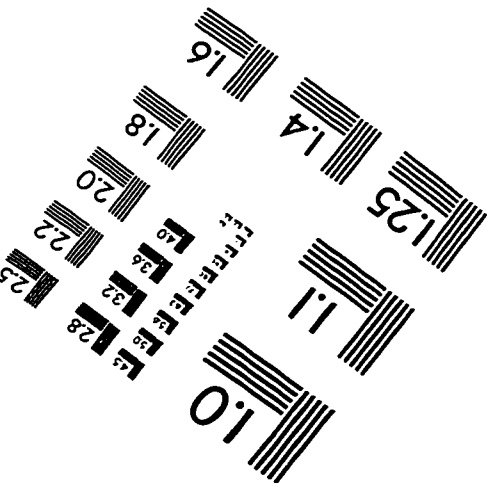
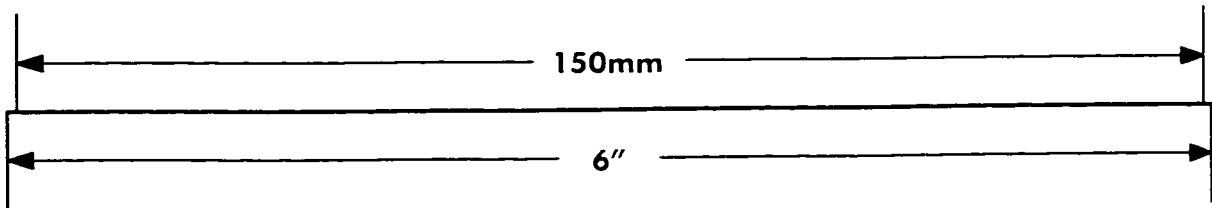
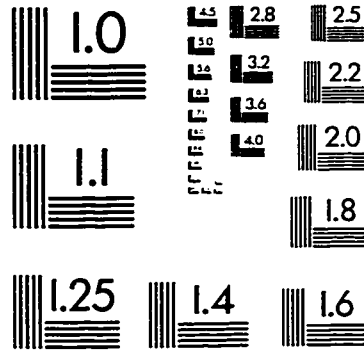
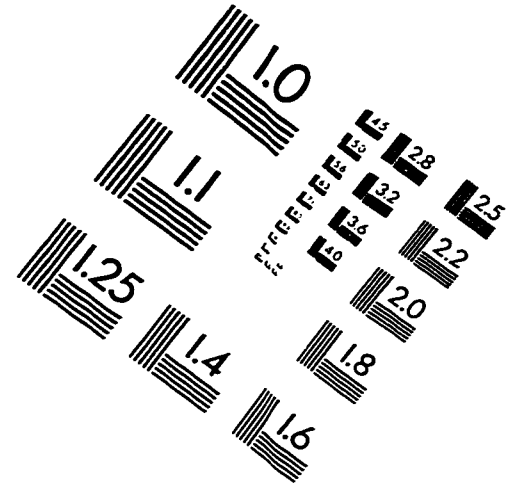
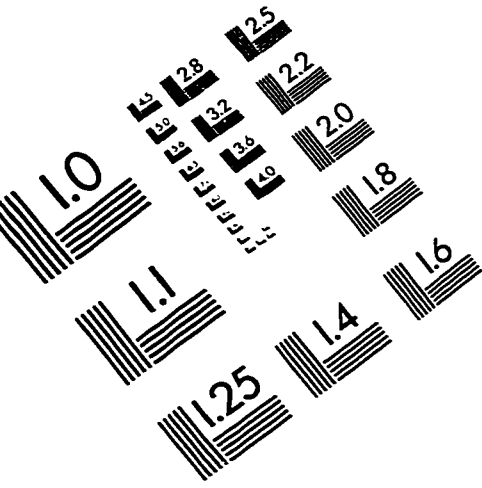
    Else
    End If
Next j

```

```

    sumazmflow = pflow
End Function
,
Function poleazm(azimuth)
    If azimuth < 180 Then
        azimuth = azimuth + 180
    Else
        azimuth = azimuth - 180
    End If
    poleazm = azimuth
End Function
,
Function poleinc(incl)
    incl = 90 - incl
    poleinc = incl
End Function
,
Function rads(angle)
    pii = 3.14159265
    angle = angle * pii / 180
    rads = angle
End Function
,
```

IMAGE EVALUATION TEST TARGET (QA-3)



APPLIED IMAGE, Inc
1653 East Main Street
Rochester, NY 14609 USA
Phone: 716/482-0300
Fax: 716/288-5989

© 1993, Applied Image, Inc., All Rights Reserved